Three dimensional cloud and dynamical structure of Southern Hemisphere extra- tropical cyclones in observations and in a model

Pallavi Govekar, M.Sc.

A Thesis Submitted in Fulfillment of the Requirements
for the degree of

Doctor of Philosophy

School of Mathematical Sciences
Monash University

March, 2013

Statement

Notice 1

Notice 2

I certify that I have made all reasonable efforts to secure copyright permissions for third-party content included in this thesis and have not knowingly added copyright content to my work without the owner's permission.

[redacted]

Pallavi D. Govekar

Acknowledgements

It has been a great privilege to spend several years in the Department of Mathematical Science at Monash University. I am indebted to many people for making the time working on my Ph.D. an unforgettable experience.

First of all, I would like to thank my supervisor, Prof. Christian Jakob for his constant support, encouragement and guidance throughout the years of my PhD study, and without whom none of this would have been possible. I honestly appreciate his patience and support during the last few months of my writing-up period. Christian's ability to select and to approach compelling research problems, high scientific standards, and his hard work set an example for me. I am very grateful to my associate supervisor Prof. Michael Reeder who first offered me an opportunity to start my research career in Atmospheric Science. Michael has been supportive since the days I began working on my masters degree in Monash. He always provided refreshing insight and asked critical questions which enormously helped me in developing my scientific knowledge. Furthermore, I am very grateful to my other associate supervisor Dr. Jennifer Catto for her insightful comments in my work and thesis writing and for her support.

I would also like to thank Dr. John Haynes for his help with data, code, ideas and computing issues throughout the study, and his early guidance is highly appreciated. Further, I am very grateful to Dr. Gareth Berry for providing data for fronts and his code for trajectory analysis. I would like to extend my gratitude to all my postgraduate colleagues for their support and help. I am very privileged to get to know and to collaborate with many other great people who became friends over the last several years.

This work was funded by Science faculty of Monash University and Centre of Excellence in Climate Science, and I would like to thank both organisations for their generous support. Thanks also go to my all teachers in India. Their guidance has served me well and their encouragement in those early years of my life has meant more to me than I could ever express.

My grateful thanks go to my family for their unbound love and sacrifice. I would like to thank my parents, Vijay and Sandhya Korgaonkar, who instilled within me a love of science and always encouraged me to pursue higher study. My brothers and sister were always supporting me and encouraging me with their best wishes.

I would like to thank my husband, Dev Govekar, whose love and encouragement allowed me to finish this journey. Dev was always there cheering me up and stood by me through the good times and bad. My deepest appreciations are for my sweet little twin boys, Omkar and Vedant, who were always ready to help mum to get her 'very big certificate'. My family's love provided me inspiration and was my driving force. I hope that this work makes my family proud and will encourage my siblings and children to have confidence to fulfill their dreams.

Abstract

This study, for the first time, investigates the three-dimensional cloud and dynamical structure of extratropical cyclones over the Southern Ocean using both observations and model simulations. The three-dimensional structure of clouds associated with Southern Hemisphere extratropical cyclones is constructed using active observations from the CLOUDSAT and CALIPSO satellites. First, a composite cyclone is constructed from cyclones in 40^0S - 50^0S in the years 2007 and 2008 using the cyclone center as the composite reference point. It is shown that the three-dimensional cloud distribution around a composite cyclone captures well-known features of conceptual models of extratropical cyclones with thick high top clouds in the frontal region and low clouds of varying depth behind the system. Composite mean fields of sea level pressure, vertical motion, potential temperature and relative humidity are superposed on the three dimensional cloud structure to identify key links of the cyclone dynamical structure with the cloud field. Further, the relationship between dynamical and cloud processes in full three dimensions around cyclones is quantified. The change in relationship between clouds and dynamical fields with cyclone strength and life cycle are investigated.

The ACCESS (Australian Community Climate and Earth System Simulator) model is compared to CloudSat/ CALIPSO observations. Model fields for MSLP, omega, relative humidity and cloud fraction are examined. The model cyclones were tracked using the MSLP field of the model. The overall cloud structure is qualitatively reproduced by the model. However, high-level cloud occurrence is overestimated while low-level cloud occurrence is severely underestimated. There are too few clouds behind the system and too many high clouds in the warm frontal region, compared to observations. It is found that the range of most dynamical variables in the composite cyclone is smaller than observed, indicating that the dynamical properties of the model cyclones are not well simulated. The possible implications this has for the simulation of clouds around cyclones are discussed.

Contents

List of Figures

List of Tables

Chapter 1

Introduction

1.1 Clouds in the climate system

Clouds play an important role in the climate system. At any given time, approximately 60 to 70 % part of the planet is covered by clouds. They exist in a great variety of forms and on a large range of both temporal and spatial scales. The processes related with the formation and dissipation of clouds span an even larger range of scales from micrometers for the condensation of individual droplets to thousands of kilometers for cloud systems within extratropical baroclinic systems. Clouds are directly linked to a large variety of weather phenomena. They are required for precipitation to occur and hence, are an important component of the Earth's hydrologic cycle. They interact directly with air motions through both latent and radiative heating. Moreover, clouds produce a net energy loss or gain to the earth system through their radiative effects. In the global average, clouds produce more cooling than warming. Thus variations of clouds can influence the climate by amplifying or reducing changes in it.

Clouds are strongly associated with the major circulation systems of the planet as is evident from the fact that satellite imagery of cloud patterns is extensively used to identify circulation systems, such as extratropical and tropical cyclones as well as convective systems of the Intertropical Convergence Zone.

Representing clouds in general circulation and weather prediction models has proven challenging due to the complex nature of cloud processes, which act on scales much smaller than contemporary model resolutions. The reports of the Intergovernmental Panel for Climate Change (IPCC) so far have all highlighted clouds and cloud feedbacks, as a major uncertainty in our understanding of the climate system as well as our ability to project changes to this system. For example, the Working Group report of the Fourth Assessment report of the Intergovernmental Panel on Climate Change (Solomon et al., 2007) says "despite some advances in the understanding of the physical processes that control the cloud response to climate change and in the evaluation of some components of cloud feedbacks in current models, it is not yet possible to assess which of the model estimates of cloud feedback is most reliable." The largest uncertainty in the estimates obtained from GCM simulations of climate sensitivity is in cloud feedback (Cess et al., 1990; Bony et al., 2006; Sanderson et al., 2008; Lauer et al., 2010; Zhou et al., 2013).

The basic idea of this study is to highlight key cloud and radiative features of Southern Hemisphere mid-latitude extra-tropical cyclones and their link to the underlying cyclone dynamics. To do so, a compositing technique that combines many individual cyclones into a composite - or average - cyclone is applied. The organization and, for the first time, the three dimensional structure of clouds associated with the Southern Hemisphere cyclones are studied using active observations for clouds. The methodology developed in this study illuminates the relationship between dynamical and cloud processes in full three dimensions around cyclones. We then use this methodology to evaluate climate model's ability in simulating the cloud and dynamical structures of the Southern Hemisphere extratropical cyclones.

1.2 Observing clouds

Clouds can be an indicator of the weather and possible weather change in the hours or even days to come. For example, a long band of clouds in a satellite image can be evidence of the approach of a cold front or nimbostratus clouds can signify the advent of rain or snow. The life span of clouds in the atmosphere ranges from minutes to days. This temporal diversity is matched by the broad spectrum of spatial scales associated with clouds.

Cloud observations can be acquired from the earth's surface by humans or by an automated system, from an instrumented aircraft or from a space platform. The surface based observations tend to have the largest records and provide information that is valuable for cloud studies on climatological time scales. The cloud observations taken from the earth's surface are taken from a fairly close distance of 10 to 15 km. Ground observers can resolve individual clouds within their field of view and thus can easily identify clouds by type. A climatology of total cloud cover and cloud - type amounts have been published using surface based observations (Hahn and Warren, 1995; Warren et al., 2007). These climatologies were mainly used for analysis of inter-annual variations and trends. However, a surface based observer takes a bottom-up view and hence excludes middle and high level clouds if they are situated above low level clouds. These observations are local (Henderson-Sellers, 1986; Jones and Henderson-Sellers, 1992) and covering whole globe at a time is impossible. Another problem with surface-based observations is that the vertical extent of the clouds also impacts on the observer's perception of the percentage coverage of his/her hemispheric view. This can lead to a positive bias in surface-based estimates. Aircraft frequently penetrate clouds and take observations of their microphysical structure (e. g. Mossop et al. (1970); Twomey and Cocks (1982)). But for large areas, it is impossible to acquire observations of clouds in all but a few instances and locations.

Satellite technology provides an unprecedented view of clouds (Henderson-Sellers, 1992; Stephens et al., 2002; Mace, 2010). Satellites can be polar orbiting or geostationary. Geostationary satellites are positioned over one location on the earth's surface and provide high temporal resolution cloud observations. They orbit in the earth's equatorial plane at a height of approximately 36,000 km. They are particularly useful for monitoring tropical cyclones and severe local storms. This would be impossible from surface observation alone. Geostationary satellites, however, do not cover polar areas. Moreover, for the geostationary satellites, the view of middle and low level cloud may be partially or fully obscured when there is higher level cloud above them. Polar orbiting satellites operate in a sun-synchronous orbit. They generally fly at a low altitude and pass over the poles on each revolution. Because of their lower orbit (800-900 km) polar orbiting satellites give much better spatial resolution. They offer a more global view of the earth than the geostationary satellites, but their disadvantage is that they see every point on Earth only a few times a day. Each satellite carries sensors that detect the amount of visible light, thermal radiation, and radiation from other parts of the electromagnetic spectrum coming from the Earth. Each sensor is sensitive to the specific spectral band, so geostationary and polar orbiting satellites generally use multiple sensors.

Many climatologies of cloud properties based on satellite observations are available now. The International Satellite Cloud Climatology Project (ISCCP, Rossow and Schiffer (1999)) provides geostationary and polar-orbiting satellite observations of clouds for 30 years. It uses visible and near-infrared (VIS/NIR, day only) and infrared (IR) spectral bands. ISCCP data will be discussed in detail further in Chapter 2. The Moderate Resolution Imaging Spectroradiometer (MODIS, Justice et al. (1998)) instruments aboard the National Aeronautics and Space Adminis-

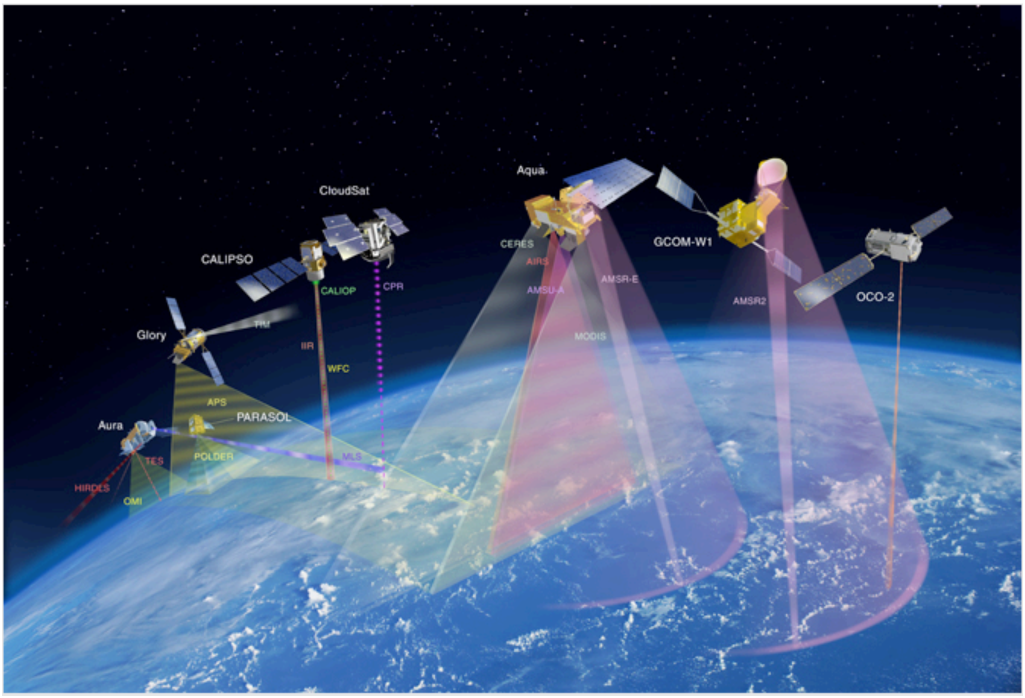

Figure 1.1: Artist's concept of the A-Train constellation of satellites. Figure is adapted from NASA's website, http://www.nasa.gov/mission_pages/a-train/a-train.html

tration (NASA) Earth Observation System (EOS) satellites Terra and Aqua provides cloud observations globally. The Clouds and the Earths System experiment (CERES, Wielicki et al. (1996) provides both solar-reflected and Earth-emitted radiative fluxes from the top of atmosphere (TOA) to the Earth's surface.

The Afternoon A-Train (Stephens et al., 2002), a constellation of four satellites, allows multiple sensors to make near-simulteneous measurements of the earth's atmosphere in both space and time (Figure 1.1). The Cloud Profiling Radar (CPR, Stephens et al. (2008)) onboard the CloudSat satellite, and the CALIOP lidar on the CALIPSO satellite (Winker et al., 2007), both part of the A-train, provide active observations of clouds. These observations are the most comprehensive global observations of the vertically varying distribution of the clouds available to date. The CloudSat/CALIPSO data will be discussed in detail in Chapter 2.

1.3 Southern Hemisphere mid-latitude cloudiness

The Southern Hemisphere is ocean dominated and hence has different properties than its counterpart, the Northern Hemisphere. The cloud systems over the southern Ocean cover over 10% of the earth's surface. The lack of inhabited land is a strongly limiting factor in the collection of *in situ* cloud observations over the ocean dominated Southern Hemisphere mid-latitudes. So for Southern Hemisphere midatitude cloud observations, we have to rely mostly on satellite data.

The global distribution of clouds has been studied extensively in particular since the advent of satellites (e.g. Rossow and Schiffer (1999) and references therein). For example, clouds in the tropics have received detailed attention due to their connection to deep convection and tropical cyclones. However, until recently, with few exceptions (e.g. Troup and Streten (1972); Zillman and Price (1972); Jones and Henderson-Sellers (1992); Morrison et al. (2009); Mace (2010); Gordon and Norris (2010); Haynes et al. (2011); Verlinden et al. (2011); Bodas-Salcedo et al. (2012); Naud et al. (2012)) clouds in the Southern Hemisphere extratropical region have received relatively less attention than their Northern Hemisphere counterparts.

The Southern Ocean's cloud climatology is different from the rest of the globe with the largest fraction of low level cloud cover and a fair portion of relatively thick mid-level clouds (Mace et al., 2007). Many parts of the Southern Ocean have a cloud cover of more than 80% with little seasonality. Except for some regions of South America, there is not much variation in cloud cover latitudinally or longitudinally.

Clouds have a profound influence in the Southern Ocean region, as the background albedo is low leading to a large sensitivity of the radiative fluxes to the presence of clouds (Cess et al., 1990; Tsushima et al., 2006). Recently, clouds over the Southern Ocean have been the subject of increased interest due to mounting evidence of their poor representation in climate models. Climate model errors in top of atmosphere (TOA) fluxes over the Southern Ocean are large compared to rest of the world (Trenberth and Fasullo, 2010). Errors in the cloud representation over the Southern Ocean will have large effects on the global TOA energy balance for solar radiation as the area coverage of the Southern Ocean is vast. Trenberth and Fasullo (2010) studied the climate sensitivity of models (defined as the change in surface temperature produced by doubling atmospheric carbon dioxide) and showed a strong linear relationship between it and the net radiation at the Southern Hemisphere TOA. The smallest climate sensitivity was found in models which have a greater than observed net downward TOA radiation while the highest climate sensitivity was found in the models which have produced a net TOA radiation similar to that in observed. This highlights the potential importance of the correct representation of Southern Ocean clouds in current day climate models.

To improve the representation of Southern Hemisphere clouds in climate models, we need to first correctly identify the type, horizontal and vertical distribution, radiative effects and organization of Southern Ocean clouds. Models should not only produce satisfactory mean radiative fluxes but also should be able to produce clouds affecting those fluxes with the right properties in the correct locations, consistent with the clouds observed in nature. In this study, we will develop a method which will provide another innovative opportunity for an in-depth evaluation of climate models. The comprehensive picture of an extratropical cyclone painted by our data analysis will provide the possibility to evaluate a climate model's ability to simulate the concurrent cloud, dynamical, radiative and precipitation structures of extratropical cyclones in the Southern Hemisphere. This study will provide a major ingredient to not only understand the mean behavior of models over the Southern Ocean, but to ensure that this behavior is produced from the right combination of physical processes as they act in the major building blocks of Southern Hemisphere weather, extratropical cyclones.

1.3.1 Southern Hemisphere mid-latitudes cloudiness in observational studies

Various *in situ* field observations have uncovered many unique features of the ubiquitous low-altitude Southern Ocean clouds. Cloud droplet, radiation and cloud condensation nuclei (CCN) observations around the Australian continent have been collected for more than 50 years (e. g. Squires (1956)). Over the years, the microphysical aspect of cloud development was studied more comprehensively as more and more experimental evidence was gathered (Twomey, 1959; Twomey and Warner, 1967; Warner, 1970, 1979). From the early 1970s, several aircraft studies focussed on the radiative structure of clouds and recognized its importance and its link to the microphysical cloud structure. These short flight campaigns were conducted for some local areas in the Southern Hemisphere mid-latitudes. Their intentions were relevant to ice multiplication processes (Mossop (1985); Mossop et al. (1970, 1968), west Tasmania), to the retrieval of cloud microphysical properties from remote sensing instrument (Twomey and Cocks (1982), north-west Tasmania), or to study planetary boundary layer clouds in the region of Tasmania and the east coast of Australia (Stephens et al., 1978).

Several major field experiments undertook further *in situ* observations of the Southern Ocean boundary layer and the ubiquitous low-level clouds. The Southern Ocean Cloud Experiment (SOCEX) (Boers et al., 1996) investigated the cloud microphysical properties and linked them to the lower atmospheric aerosol structure in the Southern Ocean. SOCEX I and II flew instrumented aircraft through clouds off the coast of Tasmania to study their microphysical structure (Boers and Krummel, 1998). The Aerosol Characterization Experiment (ACE, Bates et al. (1998)) campaign utilized shipborne and aircraft measurements to study physical and chemical properties of aerosols. The first part of this experiment (ACE I) was carried out in 40^0S-55^0S to provide survey of microphysical and optical properties of the boundary layer clouds to link aerosol chemistry to cloud radiative properties.

The Australian Bureau of Meteorology provides surface based data for clouds for more than 100 years. Jones and Henderson-Sellers (1992) made use of these climate records to determine long term trends in cloud amount over Australia. They found a 5% increase in cloud cover in the period 1910-1989. They also analyzed sunshine records and found an anti-correlation between cloud and sunshine fractions.

Fitzpatrick and Warren (2007) used surface radiation and cloud cover measurements acquired from voyages of the RSV Aurora Australis (AA) during year 1991-2002 and developed climatologies of cloud albedo, optical depth, shortwave irradiance and cloud radiative forcing at the surface for the Southern Ocean for the latitudes 50^0S-80^0S. They attempted to quantify the effects of sea ice and clouds on the climate and found that in summer, the clouds are more important than sea ice for the radiation balance at all latitudes in the Southern Ocean.

Limited microphysical properties of wintertime clouds over localized areas in the Southern Ocean were studied by cloud seeding experiments. Numerous cloud seeding research programs were conducted over the island of Tasmania. Two cloud seeding experiments, in 1964-71 (Smith et al., 1979) and in 1979-83 (Ryan and King, 1997) have documented *in situ* observations of mixed-phase clouds with particular interest in supercooled liquid water and reported increases in precipitation related with cloud seeding periods. Furthermore, Morrison et al. (2009) analyzed cloud seeding activity for the period 1960-2005 and found consistent increases in precipitation. Combining limited satellite, radar and *in situ* observations along with numerical simulations, Morrison et al. (2010) examined low level clouds through two case studies over Tasmania. They suggested that low level clouds may commonly exist in a supercooled state, rather than being glaciated or mixed phase. Moreover, their numerical simulations suggested that such clouds should readily exist widely across the Southern Ocean.

The local energy budget, particularly, absorbed shortwave radiation is dependent on the phase of water exposed at cloud top (Gregory and Morris, 1996). Better understanding of the phase of low level clouds in the Southern Ocean may therefore be imperative to properly constrain the global energy budget. To highlight the prevalence of supercooled liquid water in low-altitude cloud tops located within the higher latitudes over the Southern Ocean, Morrison et al. (2011) used a three year climatology of cloud-top phase from the MODIS. They concluded that the supercooled liquid water is present year-round in the low level clouds over Australia.

In a recent major observational study in the Southern Hemisphere, Haynes et al. (2011) used measurements from active and passive satellite based data sets to examine the organization and structure of Southern Hemisphere mid-latitude clouds. Using cluster analysis based on ISCCP observations (Jakob and Tselioudis, 2003; Rossow et al., 2005), they found that Southern Hemisphere mid-latitude cloud systems are organized into eight distinct regimes. Further using Cloudsat/CALIPSO active observations, they showed that all regimes contain a relatively high occurrence of low clouds, with a peak below 2 km. They also concluded that the spatial distribution of regimes vary with season and on average, these cloud systems are thicker during winter than summer.

Verlinden et al. (2011) documented the key features of clouds over the Southern Hemisphere high latitudes using data from Cloudsat/CALIPSO satellites. Consistent with Haynes et al. (2011), they noted a pronounced seasonal cycle in these cloudiness. They found two distinct maxima in vertical profiles of cloud incidence over the Southern Ocean, one centered near the surface and another centered in the upper troposphere.

1.3.2 Southern Hemisphere midlatitude cloudiness in models

Most General Circulation Models (GCMs) produce too low cloud amounts compared to observations in the midlatitude oceans. A general circulation model tested by Naud et al. (2010) did not form enough clouds across warm and cold fronts, partly because of its coarse spatial resolution. Field et al. (2011) found that the UK Met Office model produces less clouds poleward of the main low pressure belt than observed. Insufficient storm activity or deficient cloud cover may be responsible for large radiation errors in the model. The radiation biases are particularly large over the Southern Ocean.

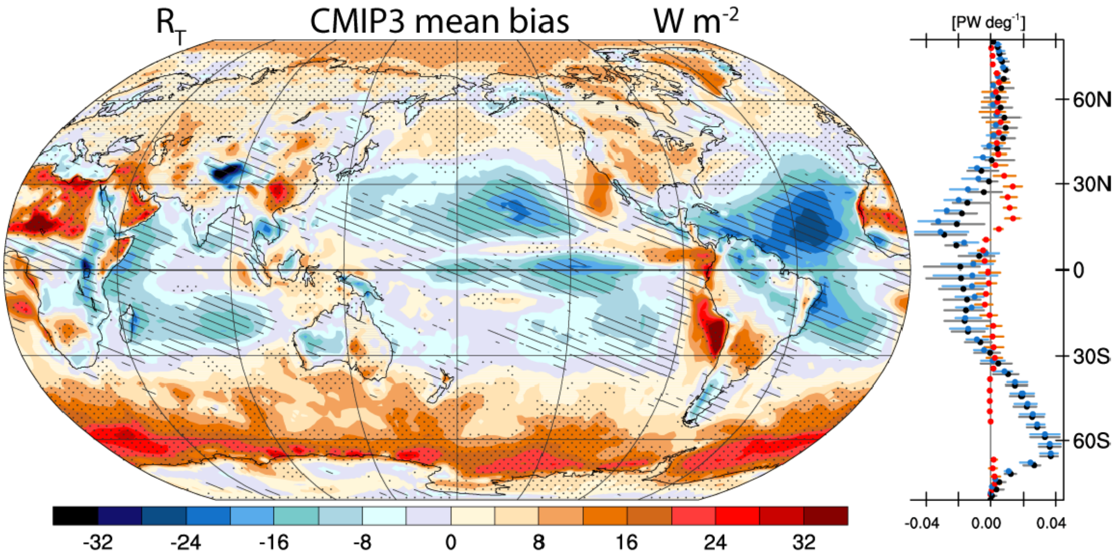

Figure 1.2: CMIP3 multi-model mean bias in net downward TOA radiation (R_T) relative to observations for 1990-1999 in W m^{-2}. (from Trenberth and Fasullo (2010))

After analyzing 24 climate models from the Third Coupled Model Intercomparison Project (CMIP3, Meehl et al. (2007)), Trenberth and Fasullo (2010) concluded that almost all the models absorbed too much shortwave radiation over the Southern Ocean (Figure 1.2), leading to poor representations of the radiation budget in the region. Further, they compared cloud cover in the CMIP3 models with cloud data from ISCCP and showed that the CMIP3 models show a lack of clouds which is at least partially responsible for the TOA shortwave bias. It has also been shown that climate models produce strong positive sea surface temperature (SST) biases (see Figure 1.3) where the shortwave radiation is too large (SenGupta et al., 2009), although a causal connection of the two errors has not been conclusively established.

The effect of clouds on both shortwave and longwave radiation can be quantified using cloud radiative effect (CRE), the difference between the net TOA solar radiation fluxes at clear sky and full sky conditions (Ramanathan et al., 1989). Webb et al. (2001) and Williams and Webb (2009) show that a lack of mid-level-top clouds in the mid-latitude oceans contributes to a weak CRE in many models, which leads to an excess in surface downwelling surface radiation. Tsushima et al. (2006) normalized shortwave CRE by the incoming solar radiation to find the 'albedo forcing'. They found that the observed albedo forcing in the Southern Hemisphere midlati-

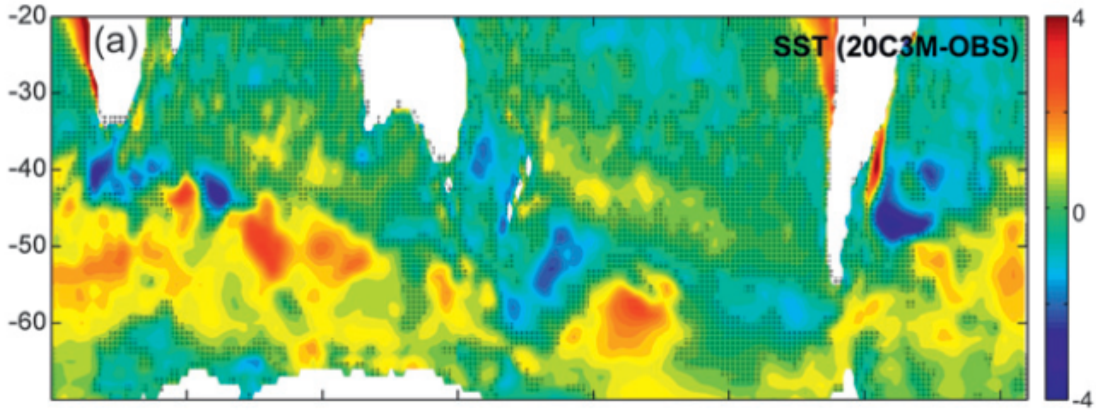

Figure 1.3: Multi-model mean SST bias in the CMIP3 climate models (from Sen-Gupta et al. (2009))

tudes the highest on the globe, indicating a large impact of clouds in this region on the TOA shortwave radiation balance. Also, they showed that climate models in the Cloud Feedback Model Intercomparison Project (McAvaney and LeTreut, 2003) had the largest inter-model differences of albedo forcing in the Southern Hemisphere mid-latitude region. This highlights the difficulties of correctly representing Southern Ocean clouds in climate models. The determination of the type of clouds which contribute to shortwave reflection over the Southern Ocean is very important to alleviate the errors in the cloud fields in models.

Extratropical cyclones, also known as mid-latitude cyclones or wave cyclones, strongly affect the extratropical distribution of cloud, precipitation and water vapor. The Southern Ocean storm tracks and their associated extra-tropical cyclones (Trenberth, 1991; Simmonds and Keay, 2000) and fronts (Berry et al., 2011) are prominent features of the Southern Hemisphere. Clouds associated with these extratropical systems form a substantial part of the total cloud field of the Southern Hemisphere cloud system (Gordon and Norris, 2010; Haynes et al., 2011). It is conceivable that the cloud fields associated with these extratropical cyclones are connected to the large radiation errors in contemporary climate models making them natural target for further study.

1.4 Extratropical cyclones

Extratropical cyclones are synoptic scale low pressure weather systems which occur in the middle latitudes of the Earth. These baroclinic systems cover vast areas of

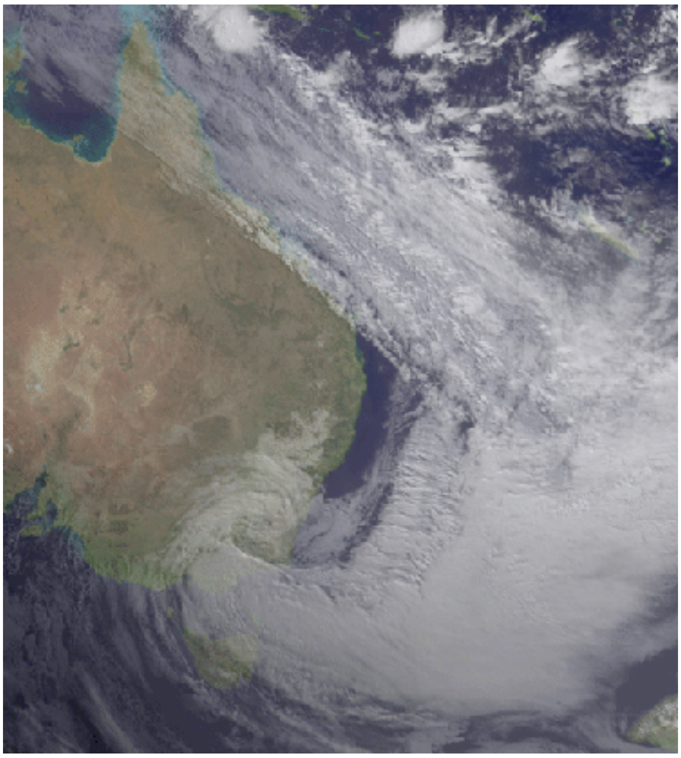

Figure 1.4: Satellite image: 8:30am 27 June 2007 - Image source - www.bom.gov.au

the planet. One example is shown in Figure 1.4 which shows a satellite image of a cyclone that occurred near the Eastern part of Australia on 27 June 2007. The cloud system related with this cyclone is very large and exerts a large influence on the radiation budget. Extratropical cyclones affect the day to day variability of weather in the mid-latitudes. Intense extratropical cyclones are associated with strong winds and heavy rain and therefore can have large socioeconomic impacts. These cyclones affect the energy budget of planet as they transport heat and water vapor poleward and they produce the bulk of the cold season precipitation in middle and high latitudes. These transient systems are mainly driven by the strong temperature and moisture gradients across the polar front.

1.4.1 The main features of extratropical cyclones

Extratropical cyclones form and grow via baroclinic instability. They get their main kinetic energy from the conversion of available potential energy. However, some contribution may also come from latent heat release. Available potential energy is proportional to the variance of temperature in the troposphere. Consequently, extratropical cyclones are more intense during winter as the temperature variance is highest at that time of year.

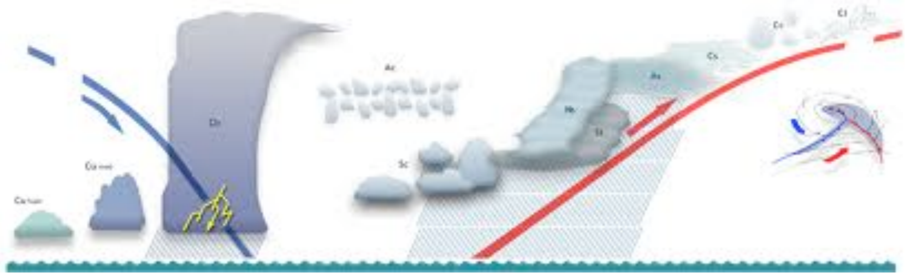

Figure 1.5: Schematic of a extratropical cyclone and its associated cloud structure. Image source - www.brockmann-consult.de

Figure 1.5 shows general features of extratropical cyclones. High level clouds of various depth can be found at eastern side of cyclone center while low level clouds can be found to the western side of cyclone center. The band of precipitation that is associated with the warm front is often extensive. In mature extratropical cyclones, an area known as the comma head on the northwest periphery of the surface low can be a region of heavy precipitation, frequent thunderstorms, and thundersnows. The distribution of clouds and water vapor depends mainly on motions associated with cyclones (Wang and Fu, 2000). It is therefore important to understand dynamical processes and airflows of extratropical cyclones.

Clouds around extratropical cyclones are strongly organized by the the internal circulations that accompany these baroclinic systems. Bjerknes and Solberg (1922) first explained the relative movement of different air masses along inclined frontal surfaces in extratropical cyclones and related the pattern of clouds and precipitation to vertical air motion. Their 'Norwegian Cyclone Model' was developed completely from surface-based weather observations, including descriptions of clouds found near frontal boundaries. This conceptual model was so successful that it was not substantially altered until Shapiro and Keyser (1990) incorporated a frontal fracture early in the life cycle, the frontal T-bone and bent-back warm front at the mid-point of the life cycle, and a warm-core seclusion near the end of the life cycle.

Traditional isobaric charts suffer from the fact that constant pressure surface intersect the flows as they ascend or descend through them. Eliassen and Kleinschmidt (1957) used relative isentropic analysis to study the motion of airstreams in cyclones. The analysis of the airflow on isentropic surfaces allows the identification of well defined belts of cloud-producing airflows and the resulting pattern of cloud and precipitation. Using relative isentropic analysis, Carlson (1980) developed a conceptual model illustrating discrete airflows through a mature mid-latitude cyclone. This conceptual model includes three airstreams, the 'warm conveyor belt', the 'cold conveyor belt' and 'dry intrusion', identified in the storm-relative flow field. A schematic of these can be seen in Figure 1.6. The warm conveyor belt (Harrold, 1973) is a strongly ascending cloud producing flow. It is a stream of relatively warm moist air which originates at low-levels within the warm sector and flows poleward parallel to the cold front and ascends over the warm-frontal zone along the moist isentrope, forming the frontal clouds. Carlson (1980) found that the warm conveyor belt started in the lower troposphere, ascended over the warm front, and turned anticyclonically to join the westerly jet flow at higher levels. The amount of precipitation produced by a cyclone may depend upon the amount of moisture flowing into the circulation along the warm conveyor belt. The warm frontal region of the storm produces most of the precipitation in the cyclone (Eckhardt et al., 2004).

The cold conveyor belt originates poleward and east of the cyclone center in the lower troposphere and travels westward, on the cold side of the warm front, below the warm conveyor belt, toward the center of the low pressure circulation. Browning and Roberts (1994) described cyclonic and anticyclonic components of the cold conveyor belt. The anticyclonic path of the cold conveyor belt is less apparent and narrower compare to cyclonic path of the cold conveyor belt and it spreads out in the cloud head as it ascends (Carlson, 1980). Schultz (2001) reexamined Carlson's (1980) analysis of the cold conveyor belt and found a cyclonic path of the cold conveyor belt. They suggested that the anticyclonic flow should be considered as a transitional flow between the warm conveyor belt and cold conveyor belt. As precipitation produced by the warm conveyor belt falls through the cold conveyor belt, the temperature and humidity of the cold conveyor belt can play an important role in controlling the type and amount of precipitation reaching the surface.

The dry intrusion is a coherent region of cold dry air that originates near the tropopause fold (Browning, 1997) and descends on the backside of the developing cyclone to mid- tropospheric levels. Often, it is associated with the dry slot that is identified as cloud free region in satellite images of cyclones. The penetration of this dry air over the low level moisture creates potential instability that may be released in convective clouds on the edge of the dry slot.

1.4.2 Cyclone climatologies

The extratropical cyclones in the Southern Hemisphere have been studied for more than 70 years (for example, Palmer (1942); VanLoon (1965); Taljaard (1967)). How-

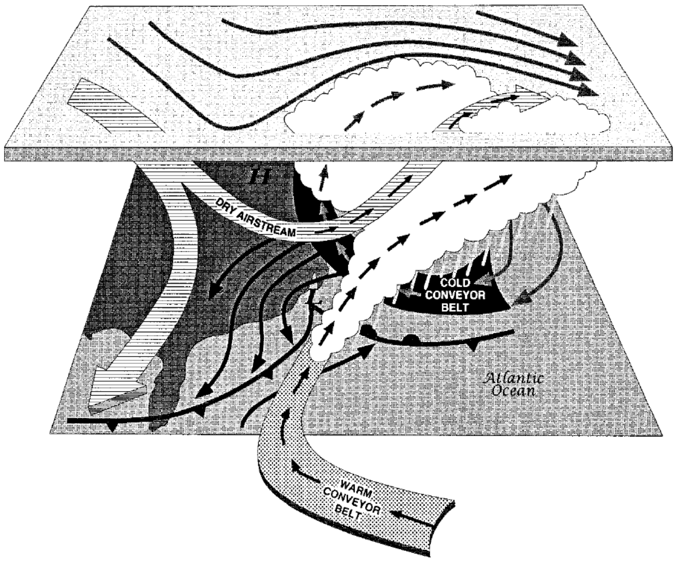

Figure 1.6: The conveyor-belt model of airflow through a northeast U.S. snowstorm (from Schultz (2001), based on the Carlson (1980, Figs. 9 and 10) conceptual model).

ever, with the advent of satellite information, studies of the development, movement and dissipation of the Southern hemisphere cyclones became more comprehensive (Streten and Troup, 1973; Carleton, 1979, 1981). One of the first climatologies of cyclogenesis, cyclolysis and track density throughout the Southern hemisphere was developed by Kep (1984) by using 10 years (1972-1981) of data. They noted a core of high track density throughout the high latitudes of the hemisphere. Moreover, they found a general tendency for cyclones to form preferentially during the month of July in the latitudinal band of 40^0 S - 50^0 S. Using the advances in computer resources, Jones and Simmonds (1993) generated a more comprehensive climatology of the distribution and behavior of extratropical cyclones in the Southern Hemisphere. This climatology was determined by an objective automatic scheme applied to 15 years (1975-89) of daily numerical analysis. It confirmed the results of previous studies. Simmonds and Keay (2000) presented a climatology of Southern Hemisphere extratropical cyclones for the period 1958-97 and showed that most Southern Hemisphere cyclogenesis occurs south of 45^0S.

Objective storm tracking provides information of spatial distribution and frequency of extratropical cyclones. Some studies used sea level pressure (SLP) for cyclone tracking (Blender et al., 1997; Bauer and DelGenio, 2006; Rudeva and Gulev, 2011) while some used relative vorticity (Sinclair, 1997; Hoskins and Hodges, 2002; Catto et al., 2010). The use of relative vorticity promotes the identification of smaller-scale storms and cyclones earlier in their life cycle than those identified by

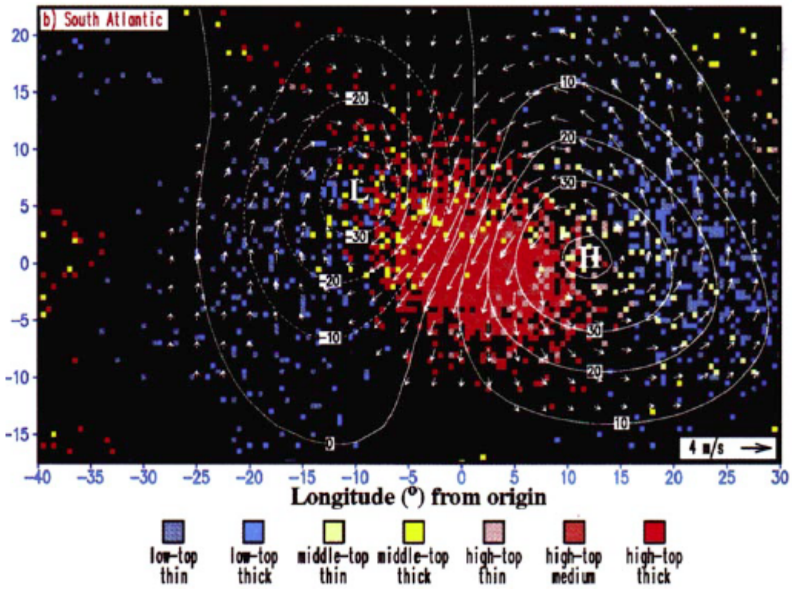

Figure 1.7: Cloud distribution from ISCCP observations (colour pixels), 1000-hPa horizontal wind (arrows) and geopotential height (contour) around the cyclone center as shown in Lau and Crane (1995).

MSLP. However, vorticity is a noisy field and use of it requires smoothing procedures and consequently, the results become dependent on the selection of the smoothing parameters (Sinclair, 1997).

1.4.3 Clouds in extratropical cyclones

The invention of satellites and radars revolutionised the capability to observe clouds and precipitation associated with cyclones. Satellite imagery has led to the discovery of many synoptic-scale and mesoscale features which were not explained by the classical models. Troup and Streten (1972) first used satellite data in the Southern Hemisphere mid-latitudes to examine vortices and related cloud patterns considering different stages of the life cycle of extratropical cyclones such as formation, evolution and decay. A satellite based classification scheme exploited satellite imaginary to identify characteristic of mid-latitude cyclones (Zillman and Price, 1972; Evans et al., 1994). Using passive satellite remote sensing, many of the dynamical, cloud and precipitation features of extratropical cyclones have been studied through case studies (Neiman et al., 1993; Browning and Roberts, 1994) and by applying cyclone compositing (Lau and Crane, 1995; Klein and Jakob, 1999; Tselioudis and Rossow, 2006; Field and Wood, 2007; Catto et al., 2010; Rudeva and Gulev, 2011).

Lau and Crane (1995) composited approximately 200 cyclones to provide a detailed view of the synoptic organization of clouds around midlatitude cyclones. Their composites for the midlatitude weather system display many of the features that were identified by other satellite data products for frontal clouds. Figure 1.7 is taken from their study and it shows spatial distribution of the observed cloud, 1000-hPa horizontal wind (arrows) and geopotential height. High top clouds are depicted in red, mid-level top clouds in yellow and low top clouds in blue. The darkness of each color indicates the cloud optical thickness. The optically thickest clouds can be seen at the center of the composite cyclone. High top thick clouds are at the north-east of the cyclone center. Middle top thick clouds are evident in the region to the southwest of the cyclone center. Ahead and behind the composite cyclone the cloud fields are dominated by low top medium thick clouds. Lau and Crane (1995) linked the mid-latitude cloud patterns with the vertical circulation in developing baroclinic waves and noted an eastward displacement of the center of the cloud shield from the position of maximum vertical ascent. They attributed this shift to the advection of clouds by the jet stream in the upper troposphere.

Tselioudis and Jakob (2002) examined cyclone-related clouds in a reanalysis and a GCM and found that in general the GCM and the reanalysis clouds are quite similar and even share some shortcomings. They further noted a deficiency of high clouds in the region of ascent in the GCM. Bauer and DelGenio (2006) suggested that this deficiency of high clouds is the direct result of the GCM's cyclones being too shallow, slow moving and due to rising motion that is too weak and too upright for a given surface intensity, when compared to the observations.

Bodas-Salcedo et al. (2012) studied role of clouds in the persistent bias of surface downwelling shortwave radiation in the Southern ocean in the atmosphere-only version of the Met Office model by compositing cloud regimes around cyclone centers. They concluded that low and mid-level clouds in the cold air sector of the cyclones are responsible for most of those biases. Further, they suggested that increase of optical depth of the low-level cloud with moderate optical depth and clouds with tops at mid-levels can address the substantial biases in the radiative properties of clouds in the model.

The above studies showed the usefulness of a composite approach when studying extratropical cyclones. The main advantage of this technique is that it reduces the case-to-case variability and allows for a realistic representation of specific cyclone features (Catto et al., 2010; Naud et al., 2010). One of the first quantitative studies using a composite technique for cyclones was carried out by Petterssen et al. (1962). Tselioudis and Rossow (2006) constructed composites of radiative and precipitation

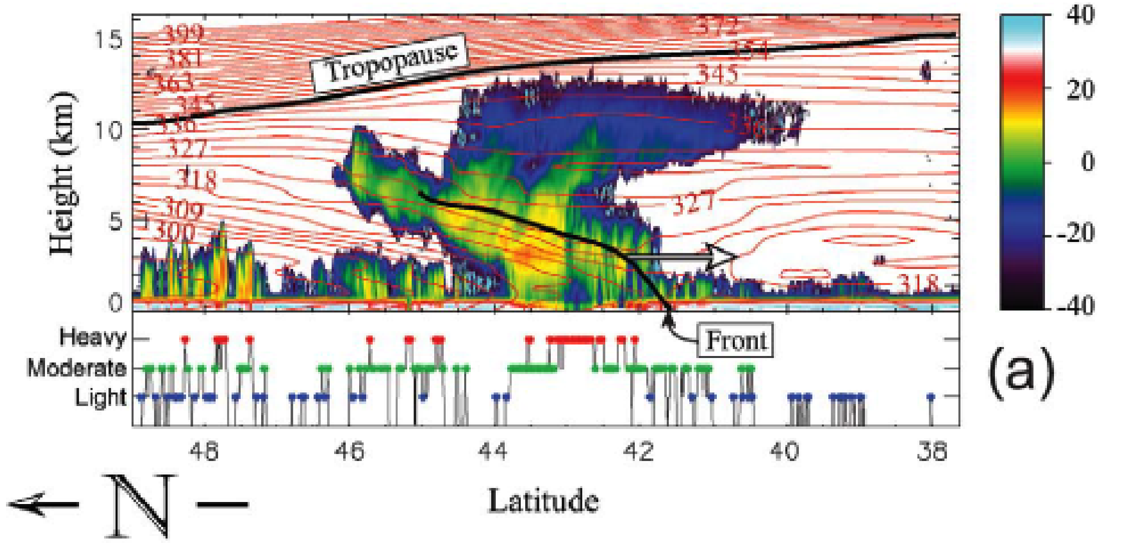

Figure 1.8: Cloud structure derived from Cloudsat for a cyclone case study as shown in Posselt et al. (2008). The positions of the front and tropopause are marked with a heavy black line, and the direction of movement of the front is indicated with a white arrow.

fluxes around extratropical cyclones and studied their effect on the Earth radiation budget. Bauer and DelGenio (2006) composited cyclones from NCEP-NCAR and the European center for Medium Range Weather Forecasts (ERA-40) as well as from the Goddard Institute for Space Studies model simulations and concluded that the model cyclones are shallower and drier compared to those in the reanalyses. Field and Wood (2007) used 1500 mid-latitude cyclones to quantify the relationships between the cyclone strength and the liquid water path and cloud characteristics. Field et al. (2008) composited midlatitude cyclones to compare satellite data to the National Center for Atmospheric Research Community Atmosphere Model (CAM3) and showed that a 1^0 horizontal grid resolution model was able to reproduce the warm conveyor belt relationship seen in the satellite data. Naud et al. (2010) composited cloud frequency of occurrence and precipitation at the warm fronts for northern and southern hemisphere oceanic cyclones. They showed that Southern Hemisphere cloud occurrence at the warm front is more sensitive to the amount of moisture in the warm sector than to wind speed.

An important limitation of studies based on passive remote sensing from satellites is that the retrieved cloud information usually represents the properties at or near cloud top or, in the case of thin cloud layers, represents a mix of properties from different levels in the atmosphere that is difficult to disentangle. The recent launch of active remote sensors on board the CloudSat (Stephens et al., 2008) and CALIPSO (Winker et al., 2007) satellites that form part of the A-Train satellite constellation (Stephens et al., 2002) provides, for the first time, an opportunity to combine observations of the cloud, radiation and precipitation with reanalyses of the circulation and thermodynamics structure to form a fairly complete composite picture of the Southern Ocean extratropical cyclones.

Using case studies, Posselt et al. (2008) showed the potential of using CloudSat/CALIPSO to add the third-dimension to the study of extra-tropical systems. Figure 1.8 is taken from their sudy. It shows observed reflectivity along the segment of a CloudSat track that intersects a cold front along with equivalent potential temperature computed from the ECMWF analysis. The tilted tropopause can be easily seen in this figure. The general cloud distribution is reasonably similar with that in classical picture of a cold front, with deep convective clouds at the front's leading edge, and cirrus aloft that extends to a distance of approximately 300 km from the surface front. Also, they noted presence of the widespread shallow convective clouds in the cold air behind the cold front. Moreover, Naud et al. (2010) demonstrated the utility of CloudSat/CALIPSO data in studying the aggregate three dimensional cloud distribution associated with frontal systems. They composited cold and warm fronts in extratropical cyclones and agreed that the cloud distributions across extratropical warm and cold fronts resemble well the classical model of cyclones with a few exceptions. They noted that clouds occur not only in the frontal region but also at low levels in advance and after the passage of the warm front and at high levels almost everywhere.

Here, we will apply these data and construct a picture of the three dimensional structure of clouds around Southern Hemisphere extratropical cyclones. As cloud structures are invariably linked to the internal circulations that accompany the cyclone, some selected dynamical fields will be composited and superposed on the three-dimensional cloud structure.

1.4.4 Extratropical cyclones in models and future projections

Given their fundamental importance to weather and climate, a good representation of extra-tropical cyclones in current climate models is of great importance. The complex interaction between a projected shift in the storm track, increased atmospheric water vapor content and potential changes in the large scale modes of variability (for example, the Southern Annular Mode, Jones and Widmann (2004)) are important to our understanding of the relation between these systems and changes in the climate of the planet. GCMs show a decrease in the number of extratropical cyclones in the simulations of future climate (Bengtsson et al., 2007). The results of observational studies show an increase in the intensity of storms (Simmonds and Keay, 2000). However, future changes in the intensity of cyclones are not consistent across models. Some studies report an increase in the number of intense cyclones (Lambert and Fyfe, 2006; Champion et al., 2011) while others find no changes in the number of intense events in future climate (Bengtsson et al., 2009). It is becoming increasingly clear that the apparent (recent and future) trends in cyclone behaviour, depend on the particular cyclone finding scheme used (Ulbrich et al., 2013).

Many studies have shown that most GCMs produce too few clouds compared to observations in the extratropics (Naud et al., 2010; Field et al., 2011). Over the Southern Ocean these errors are particularly large and are consistent with an overestimation of absorbed solar radiation in the region (Trenberth and Fasullo, 2010).

Here, we will test the ability of a modern climate model to simulate the concurrent cloud, dynamical, radiative and precipitation structures of extratropical cyclones in the Southern Hemisphere. This will lead to deeper insights into the mean behaviour of models over the Southern Ocean as well as to scrutinize physical processes in the model related to their behaviour.

1.5 Goal of the thesis

In this study, the following questions will be considered.

- What is the three-dimensional cloud structure around Southern Hemisphere extratropical cyclones?
- What is the relationship between the cloud structure and the dynamical processes of the cyclone?
- How does the cloud structure change with the intensity and life cycle of the cyclone?
- How well are the cloud structure and related dynamical processes represented in a state-of-the-art climate model?

To answer the above questions, a compositing technique that combines many individual cyclones into a composite cyclone is applied. First, consistent with previous work, passive satellite based data will be composited around the chosen cyclone centers along with objectively tracked fronts related to those cyclones. Some selected dynamical fields as well as rainfall and radiation will also be considered.

The CloudSat/CALIPSO dataset provides a unique opportunity to construct a comprehensive three dimensional cloud distribution surrounding the synoptic storms from active observations. By considering the combination of these modern satellite cloud observations, objectively tracked cyclones and fronts and supplementary reanalysis fields, we will for the first time present a consistent three dimensional picture of a (composite) Southern Hemisphere extratropical cyclone from observations.

The fully three dimensional nature of the cloud field derived in the composite allows us to illuminate the relationship between dynamical and cloud processes around cyclones and will also provide the foundation for an in-depth evaluation of a climate model's ability in simulating the cloud and dynamical structures of the Southern Hemisphere extratropical cyclones. We will evaluate the capability of a state-of-the-art climate model, the Australian Community Climate and Earth System Simulator (ACCESS) to simulate both the main features of the clouds themselves and their association with the circulation.

1.6 Outline of thesis

Chapter 2 presents the data used in this study. For the observational cloud field, passive satellite data from ISCCP and active observations from CloudSat/ CALIPSO are used. The observational dynamical fields are taken from the NCEP-NCAR reanalysis.

Chapter 3 discusses the method used in constructing the composite cyclone. First fronts related to chosen cyclones are composited to examine their organization around the cyclone center and to check whether rotation of the cyclones is necessary to better align frontal systems and their associated wind and cloud fields in the composites. Passive instrument data (ISCCP) for clouds is composited to construct a cloud field around the composite cyclone center. This chapter further gives details of the three-dimensional structure of clouds related to the cyclones as well as the relationship between dynamical and cloud processes, much in spirit of early conceptual cyclone pictures.

In Chapter 4, cyclones are classified with respect to their life cycle using an improved method of classification. Cyclones were classified into four classes considering their 'deepening' and 'filling' stage as well as considering their central pressure. The compositing method is used to examine changes in the cloud and dynamical fields with the class of cyclones.

The ACCESS model is evaluated against observations in Chapter 5. The three-dimensional cloud structure of extratropical cyclones captured by models is compared with CloudSat/CALIPSO observations. The relationship between clouds and dynamical fields related to extratropical cyclones in the model is examined and further compared with that in the observations. Model cyclones are then classified into the four observed classes and the changes in the relationship between clouds and dynamical fields with class of model cyclones are assessed. Chapter 6 summarizes the major results of this study.

Chapter 2

Data

2.1 Satellite cloud data

The main goal of this study is to study the cloud and dynamical structure associated with Southern Hemisphere extratropical cyclones. To do so, we use both active and passive remote sensing data from satellites. The main data sources of cloud data are the International Satellite Cloud Climatology Project (ISCCP) project (Rossow and Schiffer, 1999) and active observations of clouds from CloudSat/ CALIPSO (Stephens et al., 2002).

2.1.1 ISCCP data

ISCCP (Schiffer and Rossow, 1983; Rossow and Schiffer, 1991), the first project launched by the World Climate Research Programme, provides a multiyear and global coverage of different cloud parameters based on satellite measurements since 1983. One data source used in this study is the ISCCP D1 data set. It provides nearly global, three hourly, equal area gridded data, originally processed from visible and infrared radiances primarily measured by geostationary weather satellites. These satellites are equipped with sensors that measure radiances at different wavelengths. Retrievals from two of these wavelengths, 0.6 μm for the visible (VIS) spectrum and 11 μm for the infrared (IR) spectrum, are used to derive information on cloud top pressure and optical thickness every three hours. The ISCCP D1 data set provides continuous high spatial and temporal coverage of different cloud parameters like cloud amount, cloud top pressure and cloud optical thickness. This data set has data for 6596 equal-area grid boxes covering the globe, each grid cell having a size of 280 $\times$ 280 km^2.

The ISCCP-D1 data set contains retrievals of cloud fraction as a function of

Cloud-Top-Pressure (CTP) at seven pressure levels. These levels from top to bottom are CTP $<$ 180 hpa, 180 hpa $<$ CTP $<$ 310 hpa, 310 hpa $<$ CTP $<$ 440 hpa, 440 hpa $<$ CTP $<$ 560 hpa, 560 hpa $<$ CTP $<$ 680 hpa, 680 hpa $<$ CTP $<$ 800 hpa and CTP $>$ 800 hpa. The cloud top temperature and pressure retrievals in this data set are primarily based on infrared emissions, with adjustments made for thin clouds using the visible channel during daytime.

The ISCCP data was used by many earlier studies to examine clouds around cyclones (Lau and Crane, 1995; Jakob and Tselioudis, 2003; Klein and Jakob, 1999). But the vertical resolution of this data is poor. Having to rely on passive instruments like IR and VIS channels, ISCCP misses low level clouds when high-level optically thick cloud occurs over low clouds (Tselioudis and Jakob, 2002). To add a third dimension to the cloud field around extratropical cyclones, we use the active observations of clouds from CloudSat/CALIPSO.

2.1.2 CloudSat/CALIPSO data set

The CloudSat (Stephens et al., 2002) was launched in April 2006. Its active sensor, the CloudSat cloud profiling radar (CPR, Stephens et al. (2008)), started operating from June 2006. The radar has a footprint that measures vertical range bins of 240 m and 1.4 km across track (Tanelli et al., 2008). CloudSat and the lidar satellite Cloud-Aerosol Lidar and Infrared Pathfinder Satellite Observation (CALIPSO, Winker et al. (2007)) are part of the Afternoon A-Train (Stephens et al., 2002) satellite constellation which provides global observation of clouds made by using both active and passive sensors. The A-train orbit covers the latitudinal band between 82.5°N and 82.5°S with a repeat cycle of approximately 16 days.

The CloudSat radar system transmits a pulse of electromagnetic energy at 3 mm wavelength (frequency 94 GHz). This electrmagnetic radiation interacts with different types of particles in atmosphere such as cloud and precipitation particles, atmospheric gases like water vapor and oxygen. The interaction is dependent on the frequency of radiation and the type, size, distribution and orientation of the particles. These interactions result in backscattered energy which returns to the radar dish. The radar system measures this backscattered energy and converts it into radar reflectivity expressed in decibels (dBZ). Quantities like cloud water content or precipitation rate are inferred from these reflectivity measurements. Details regarding the CPR and CALIOP instruments and the resulting data products can be found online (at http://cloudsat.atmos.colostate.edu).

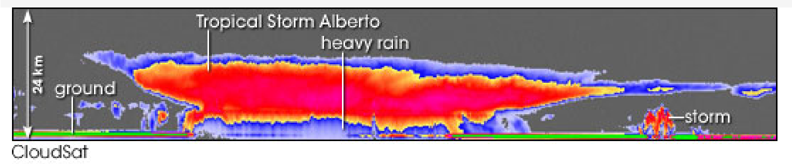

Figure 2.1: An example of CloudSat radar data. Image Source - earthobservatory.nasa.gov

CloudSat is the first space-borne radar with a wavelength that observes clouds vertically on a near-global scale. It takes measurements of vertical structure of both cloud and precipitation system from a sun-synchronous orbit approximately 705 km above the earth's surface. The CloudSat data set we use consists of radar reflectivity along with cloud parameters like cloud optical depth, cloud liquid and ice content, longwave and shortwave radiative fluxes and heating rates. The data is available at the Cloudsat data processing centre (http://cloudsat.cira.colostate.edu).

The 2B-GEOPROF (Mace et al., 2007) is one of the standard products of CloudSat. It contains two main types of information, the cloud mask information and the radar reflectivity. The characteristics of the 2B-GEOPROF product are mainly decided by the properties of the CPR. It is exceptionally sensitive to cloud-sized particles and attenuation by precipitation (Haynes et al., 2007).

Figure 2.1 shows a vertical cross-section of Tropical Storm Alberto captured by the CloudSat radar on June 12, 2006. The data shows that the storm reaches about 16 kilometers in height. The colors in the image represent the reflectivity which is the strength of the signal that returns to the radar. Higher reflectivity (pinks and reds) in tropical storm Alberto indicates more ice and/or water in the cloud. The green line at the bottom of the CloudSat image is the radar echo of the Earth's surface. Where this line disappears beneath the storm shows the area of heaviest rain. Cirrus clouds can also be seen out ahead of the storm. The CloudSat data show a smaller thunderstorm under cirrus cloud cover. That storm would be likely be hidden from the view of passive instruments.

CloudSat has ability to detect most clouds in the atmosphere. However, clouds with a small backscatter cross section which are mainly the optically thin cirrus with bases above 14 km are too tenuous to be observed by the CPR. Moreover, the CPR has a limitation in detecting boundary layer clouds whose presence is made ambiguous by noise associated with strong scattering of the earth's surface (Mace

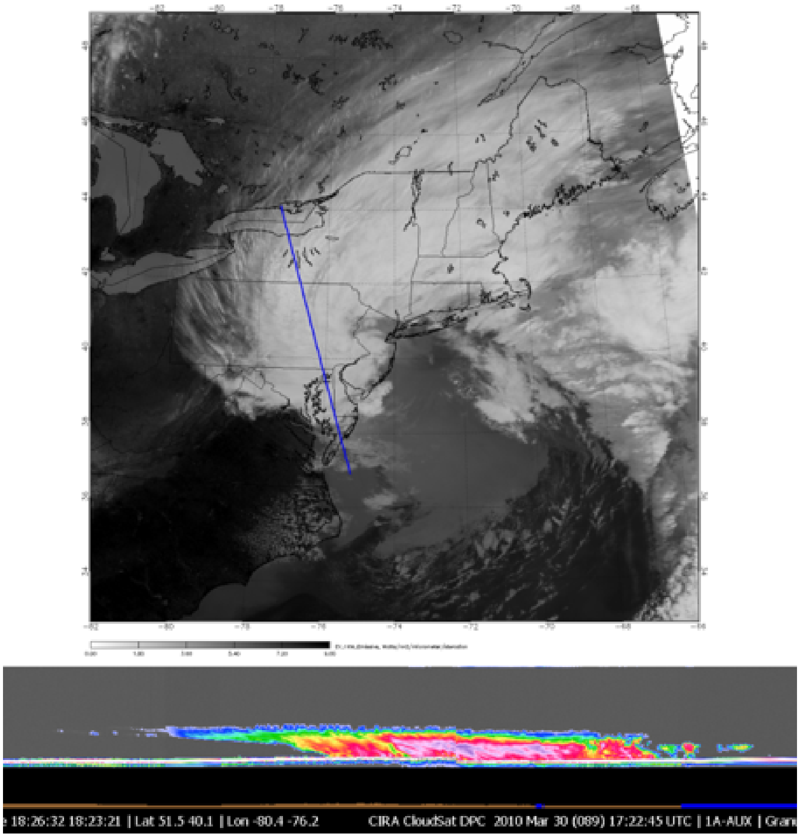

Figure 2.2: An example of CloudSat data, Image source - cloudsat.atmos.colostate.edu

et al., 2009; Haynes et al., 2011). The cloud-aerosol lidar with orthogonal polarization (CALIOP) on the CALIPSO satellite fills in many of these gaps. It operates at shorter wavelengths (532 nm and 1064 nm) and is able to detect much smaller cloud particles. It also does not suffer from the surface contamination effect (Mace, 2010; Haynes et al., 2011). To exploit the strength of both instruments in this study, we use the radar-lidar combined data from 2B GEOPROF-LIDAR product to define a cloud mask at 240m vertical and 1.4 km horizontal resolution. Mace et al. (2009) showed that the combination of CPR and CALIOP data is capable to detect cloud occurrence, correctly identifying more than 90 % of cloud layers as a cloud. If the Cloudsat radar indicates the existence of a cloud (i.e., a cloud mask value of 30 or higher) or the CALIOP lidar indicates that the radar bin in question contains 50% or greater cloud cover then cloud is considered to be present, in this study.

CloudSat provides a thin stripe of data every time as a result of its poor spatial sampling (1.4km slices). One example of such data is shown in Figure 2.2 when CloudSat intersected a storm system moving across New England on 30th March 2010. Figure 2.2 shows the CloudSat overpass slices through the western part of the storm. It shows the large area of high reflectivity indicating large amounts of rain. As our goal is to study the mean behaviour of extratropical cyclones, we can not just examine such small samples of data. The more comprehensive picture of extratropical cyclones can only be drawn by gathering many samples of data together. One such method using composites to provide a comprehensive picture of the cloud structure related to extratropical cyclones is discussed in Chapter 3.

2.2 Other data sources

2.2.1 Radiation data

In addition to mean cloud properties, we examine the radiative fluxes derived from the ISCCP data. The ISCCP-FD data set provides radiative fluxes at the top of atmosphere, at the surface and at the 680,440 and 180 hPa levels. They are computed using the ISCCP cloud properties and radiative transfer calculations (Zhang et al., 2004). These data are derived on the same temporal and spatial scales as the ISCCP-D1 data set. The flux data consists of upwelling and downwelling, shortwave and longwave radiative flux for both cloudy sky and clear sky conditions. At the top of atmosphere (TOA), cloud radiative effect (CRE) composites, i.e., the difference between clear sky and full sky conditions for both shortwave and longwave radiation (Ramanathan et al., 1989), are constructed using the ISCCP-FD data set.

2.2.2 Reanalysis data

To understand the structural and dynamical properties of cyclones, daily and 6-hourly data sets for vertical velocity, temperature, Mean Sea Level Pressure (MSLP), horizontal winds and relative humidity are used. These data are obtained from The National Centers for Environmental Prediction- Department of Energy (NCEP-DOE) Atmospheric Model Intercomparison Project (AMIP-II) (Kanamitsu et al., 2002). These reanalysis data (hereafter referred as NCEP-II) are available from the year 1979 on a $2.5^0 \times 2.5^0$ grid, at 17 pressure levels, every six hours.

2.2.3 Cyclone tracks

We use the Modeling, Analysis and Prediction (MAP) Climatology of Mid-latitude Storminess (MCMS) data to locate Southern Hemisphere midlatitude cyclones (Bauer and DelGenio, 2006). MCMS provides a detailed 6 hourly assessment of the area under influence of mid-latitude cyclone based on NCEP-II Reanalysis products. MCMS locates a cyclone as a depression in the MSLP field and tracks them over time (Bauer and DelGenio, 2006). the selection criteria for cyclones are 1) they must last at least 24 hours. 2)they must attain a minimum in MSLP of at least 1010 hPa, 3) they must travel at least 700 km during their lifetime. Variables provided by MCMS such as the cyclone track, grid MSLP, regional MSLP, intensity, area, depth of the cyclone are useful to classify cyclones. MCMS also assigns a simple intensity classification to each cyclone. By considering cyclone's minimum lifetime MSLP, deepening rate and pressure gradients cyclones were classified into three classes. The class 'intensity 1' has weak cyclones, 'intensity 2' has moderate cyclones and 'intensity 3' has strong cyclones.

2.2.4 Rain data

The Global Precipitation Climatology Project (GPCP) data is used to study the rainfall distribution around cyclones. The GPCP data set provides information of precipitation around the globe for many years. It provides monthly (Adler et al., 2003) and 1-degree daily (1DD, Huffman et al. (2001)) rainfall on a global grid from the year 1996. We apply the used 1DD rainfall data set in this study. The 1DD precipitation estimates are derived by different methods in the tropics and the extratropics. In the tropics and mid-latitudes (40^0N-40^0S), the Threshold-Matched Precipitation Index (TMPI) provides precipitation estimates based on a merged product including infrared information from geostationary satellites. In the high latitudes GPCP precipitation estimates are primarily based on statistically derived TOVS-AIRS (Television Infrared Observation Satellite (TIROS) Operational Vertical Sounder - Atmospheric Infrared Sounder) satellite data. Using a regression relationship between coincident rain gauge measurements and TOVS-AIRS based parameters like cloud-top pressure, cloud cover, the TOVS-AIRS precipitation data is inferred (Susskind et al., 1997).

Chapter 3

The composite cloud and dynamical structure of Southern Hemisphere extratropical cyclones

3.1 Motivation

Extratropical cyclones play a major role in the day-to-day variability of weather as well as climate variability in the midlatitudes due to their ability to redistribute large amounts of heat, moisture and momentum. Strong winds and heavy rain related to some of these intense systems can have major socioeconomic impacts. As a consequence the representation of extratropical cyclones is important in numerical weather prediction and climate models as these systems are the primary source of transport of energy and moisture from the midlatitudes to the poles. A good simulation of extratropical cyclones in current climate models is required for capturing the main characteristics of extreme events in the present day climate and to have confidence in predictions of future climate. Trenberth and Fasullo (2010) argued that a better simulation of the cloud radiative impact in present day simulations using the current generation of models is required to increase the credibility of the impact of cloud-radiative feedbacks on storm track activity in future climate simulations. As described in the Chapter 1, the Southern Ocean storm tracks and their associated extra-tropical cyclones (Trenberth, 1991; Simmonds and Keay, 2000) and fronts (Berry et al., 2011) are prominent features of the Southern Hemisphere, and the cloud fields associated with these extratropical cyclones are important in the radiation budget of the region.

Satellite imagery, weather radar, and surface observations are all invaluable tools for the analysis of the mesoscale structure of cloud, precipitation, and winds related to cyclones. Analyses of extratropical cyclones using these tools have been performed largely through case studies (Neiman et al., 1993; Browning and Roberts, 1994; Posselt et al., 2008). Such case studies have contributed significantly to the generation of three-dimensional conceptual models that provide a framework for understanding the internal dynamical evolution of cyclones. However, case studies have limitations as it is difficult to generalize their findings. Furthermore, case studies cannot easily be used to evaluate climate models as these models do not simulate an individual real-world cyclone. An alternative approach which enables information from a number of cyclones to be combined in a convenient form is to use a compositing technique. The use of compositing highlights basic common features while eliminating the "noise" related to individual cyclones. Cyclone relative compositing provides more generality than individual cyclone case studies without losing useful regime-specific system information that is lost in simple spatial averaging (Lau and Crane, 1995; Field and Wood, 2007; Field et al., 2008). It also provides a quantitative method for evaluating the ability of climate and weather prediction models to produce a physically realistic cyclone structure.

Clouds have a big radiative impact on the climate system but their representation in GCMs is not correct and consistent (Cess et al., 1990). The first step to improving the cloud representation in GCMs is identifying how their cloud properties differ from those in the real world. Several previous studies used composite techniques on cloud fields to carry out model-observation comparisons (Norris and Weaver, 2001; Webb et al., 2001; Klein and Jakob, 1999; Lau and Crane, 1997). The satellite data used in these previous studies relied on passive instruments thereby providing a quasi-two dimensional picture of the cloud field. With the advent of active remote sensing of clouds from space, such as CloudSat and CALIPSO arises a new opportunity to assess the three-dimensional cloud structure related to extratropical cyclones. By considering the combination of cloud observations, objectively tracked cyclones and fronts and supplementary reanalysis fields, a consistent three dimensional picture of a (composite) Southern Hemisphere extratropical cyclone can be drawn. In this chapter, this three dimensional picture of a (composite) Southern Hemisphere extratropical cyclones is developed and further the relationship between the cloud structure and the dynamical processes of the cyclone is described in detail. In Chapter 5, we will apply the same method to a state-of-the-art climate model and assess the model's ability to simulate cyclones and their associated cloud structures.

3.2 Cyclone compositing method

A technique similar to Lau and Crane (1995) that combines many individual cyclones into an average cyclone is applied here to composite the cloud field and some dynamical fields around the chosen cyclone centers. Figure 3.1 shows the four basic steps involved in generating the composite cyclones. The first step in the analysis is to identify and track cyclones over the Southern Ocean. There are many stae-of-the art cyclone identification schemes available (Neu et al., 2013) to identify and track cyclones. For the tracking procedure cyclones are identified by using MSLP field (Bauer and DelGenio, 2006; Blender et al., 1997), geopotential height field (Blender and Schubert, 2000) or vorticity field (Sinclair, 1997; Simmonds and Keay, 2000) in those schemes. As discussed in Chapter 2, we used the Modeling, Analysis and Prediction (MAP) Climatology of Mid-latitude Storminess (MCMS) data (Bauer and DelGenio, 2006) to identify and track the cyclones. The second step of the compositing is to find the points along each cyclone track (in terms of longitude and latitude) where the cyclone satisfy a given criterion (e.g. age, intensity of the cyclone). As the longitudinal extent of the cyclones varies with latitude, a grid based on distance is chosen for the compositing (Field and Wood, 2007). In the third step, a 4000 km $\times$ 4000 km grid box (x and y are the eastward and northward coordinates, respectively), is drawn around each identified cyclone center. This box is big enough to include mature cyclones along with their related transient ridges ahead or behind them, but not so big to include any following large cyclone. This assertion will be tested below by compositing fronts and rainfall to investigate if any of their signatures are visible behind the main composite cyclone.

Finally, in the last stage, a new coordinate system, with 100 km grid spacing, is defined with the cyclone center as its central point (x=0, y=0) and all the cyclones are overlaid in that new cyclone-relative coordinate system. No attempt is made to link the identified cyclones in time, which means that individual cyclones at different times in their life are identified as separate "cyclones".

Some studies have composited cyclones using a cylindrical polar coordinate system and suggested the need to rotate the cyclones according to their direction of propagation (Rudeva and Gulev, 2011; Catto et al., 2010; Bengtsson et al., 2007). The main reason for this rotation is to better align frontal systems and their associated wind and cloud fields in the composites. As the main aim here is to study the cloud structures associated with the cyclones, it is important to test whether rotation is required. To do this an objective algorithm to identify fronts using wet

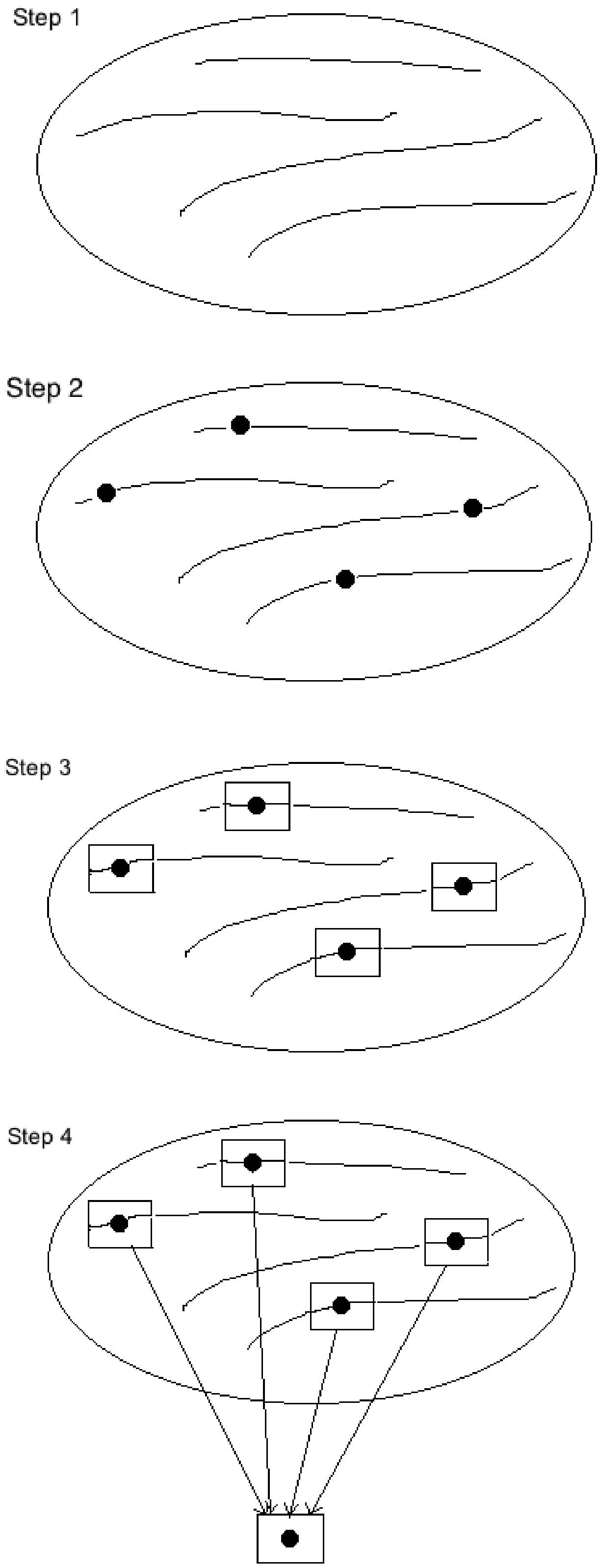

Figure 3.1: Schematic of the compositing method. Step 1) Identify cyclone tracks within the given region and time period, step 2) Find the region where the cyclone satisfies a given criterion like age or intensity, step 3) Draw a 4000 km × 4000 km grid box around each cyclone center and step 4) Overlay all boxes on each other in the newly defined co-ordinate system.

bulb potential temperature (θ_w) at 850 hPa (Berry et al., 2011) is applied to the NCEP-DOE AMIP-II Reanalysis (Kanamitsu et al., 2002). The number of occurrences of cold and warm fronts in each of the 100 km $\times$ 100 km grid boxes of the composite is determined. Figure 3.2 shows the number of cold (panel (a)) and warm (panel (b)) fronts identified in each of the 100 km $\times$ 100 km grid-boxes of a cyclone composite using 810 cyclones overlaid with the composite sea-level pressure. It is evident that the fronts are well organized within the cyclone composite and adhere to the idealized picture of frontal locations in extratropical cyclones (Bjerknes and Solberg, 1922; Shapiro and Keyser, 1990). Cold fronts are located to the north of the cyclone center while warm fronts are located on its eastern side. While there is some spread in the location of the fronts, the overall structures are clearly identifiable, leading us to conclude that rotation of the cyclones is not essential for the present study. While there are a few instances of warm fronts at the western edge of the composite box, this analysis confirms that our composite is largly free of cyclones following the main one. It is worth noting that cyclones are composited over all stages of development and the resulting composite cannot be expected to display the well-known development-stage dependent tilt of the systems (Lim and Simmonds, 2007). Also, the conclusion that no rotation is required has been shown here for the Southern Hemisphere, and is probably not true for the more complex cyclone structures in the North Atlantic and Pacific.

3.3 The composite cyclone as seen by passive satellite instruments

3.3.1 Cloud data from the ISCCP

Many studies examined clouds associated with extratropical cyclones using cloud data from different data sources like ISCCP, MODIS, etc. (Lau and Crane, 1995; Klein and Jakob, 1999; Norris and Weaver, 2001). These data were derived using passive satellite instruments. Here, the ISCCP (International Satellite Cloud Climatology Project) dataset is used to take a first look at the cloud distribution around extratropical cyclones. The ISCCP cloud data is derived using passive instruments using two satellite channels, one in the infrared and one in the visible part of the spectrum (see Chapter 2). The composite cloud cover is constructed here by averaging this passive-satelite derived cloud fields in the new cyclone-relative coordinate system explained in the compositing method section above. As a first step in compositing, cyclones at 12 UTC in the latitudinal band 40^0S-50^0S and longitudes 0^0-357.5^0E for the years 2000-2001 are identified. Considering the limited visible

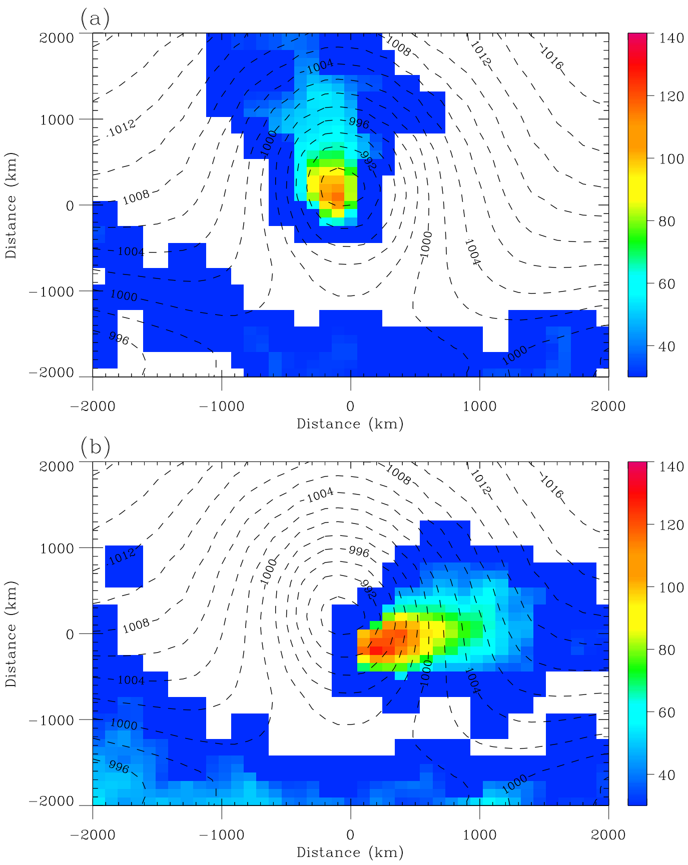

Figure 3.2: Cyclone composite MSLP (hPa) with absolute number of (a) cold fronts and (b) warm fronts. The colour denotes number of fronts and MSLP is shown by dashed contours.

channel measurements in the polar zone during the winter season, and difficulties in detecting clouds over ice-covered surfaces, we analyze the cloud data from ISCCP only until 60^0S. Consequently, the 4000x4000 km cyclone area box is reduced to a 4000 x 2200 km grid box around each chosen point, for all graphics showing ISCCP clouds.

Data related to 803 cyclones that fulfil the above criteria in the years 2000-2001 are examined in Figure 3.3 which shows the ISCCP-derived cloud structure and MSLP (dashed lines), averaged over the chosen cyclones. As discussed in Chapter 2, ISCCP provides cloud cover based on Cloud Top Pressure (CTP) in seven layers, each of which is shown in a separate panel. Isolines of one third of the maximum value of occurrence of warm and cold fronts (shown in Figure 3.2) are also overlaid in Figure 3.3 to identify the most common locations of the fronts in the cyclones that comprise the composite. The center of the composite cyclone with its minimum pressure of $\approx 994hPa$ is clearly identifiable. Panel (a) of Figure 3.3 shows very low level clouds with a CTP greater then 800 hPa. It shows clouds at the north-west side of the composite cyclone center, extending to the western side of the cold-front region. There are no clouds in the warm frontal region at this level. It is worth noting that this does not necessarily imply the absence of low clouds in this region, as the passive nature of the measurements may lead to shielding of low clouds by overlying high clouds (see below).

Panel (b) shows clouds with CTP between 680 hPa and 800 hPa. The maximum cloud cover occurs at the western side of the cyclone center and again the warm frontal region shows very few clouds at this level. Panel (c) shows clouds with CTP between 560 and 680 hPa. The maximum cloud cover at this level occurs to the south of the cyclone and is strongly associated with the cyclone-induced flow.

The next three panels, which show high clouds between 440 hPa and 560 hPa, 310 hPa and 440 hPa, and 180 hPa and 310 hPa respectively, show cloud cover maxima in the warm frontal region. At all three levels the cloud field is characterized by a 'comma' shaped structure. The high level clouds block the view of low clouds in the warm frontal region below. There is a shift in the cloud field between the three high cloud levels with higher clouds more closely wrapped around the cyclone center. Note that at least part of this behaviour might be due to the blocked view of the lower levels again. Interestingly, there are no clouds in the cold frontal region. The highest level where clouds have CTP $<$ 180 hPa don't show any clouds.

Consistent with previous studies, the ISCCP data overall allows a good first view of the structure of the clouds around the composite cyclone center (Lau and Crane, 1995). High-top clouds tend to occur along the eastern edge of the center in the warm frontal region. Most of the low top clouds are found amidst the cold airstream behind the main system. Middle-top clouds reside within the westward region of the center. However, a major drawback is that the view of lower level clouds is blocked by upper level clouds, which severely distorts our view of the cloud structure and makes it difficult to connect the cloud structure to dynamical features of the cyclone.

3.3.2 Radiation and precipitation around the composite cyclone

Extratropical cyclones strongly affect the atmospheric energy budget, not only through their dynamical characteristics, but also through the radiative and latent heating effects of their cloud and precipitation structures. As defined in Chapter 1, at the top of atmosphere (TOA), the cloud radiative effect (CRE) can be defined as the difference between clear sky and full sky conditions for both shortwave and longwave radiation (Ramanathan et al., 1989). The impact of clouds on the radiation budget can be quantified in terms of the CRE (Bodas-Salcedo et al., 2012; Tselioudis and Rossow, 2006). The composites of longwave CRE, shortwave CRE, and net CRE which is the sum of longwave CRE and shortwave CRE are constructed using the three hourly ISCCP-FD dataset (Zhang et al., 2004). GPCP daily data is used to composite precipitation data around the composite cyclone.

Figure 3.4 shows the distribution of the shortwave, longwave and net CRE, as well as the precipitation around the composite cyclone. There is a strong negative CRE in the shortwave of more than 60 W/m^2 in the entire domain (cf. Fig. 3.4(a)). The shortwave negative (cooling) CRE is largest just to the southeast of the cyclone center, where it reaches almost 200 W/m^2. While the largest CREs lie in the warm frontal region, there are wide-spread strong shortwave CRE away from that area due to the prevalence of low clouds around the cyclone center. Longwave CRE are generally weaker than the shortwave CRE, peaking at about 55 W/m^2 (cf. Fig. 3.4(b)). As the positive (warming) longwave CRE are generally driven by high-level clouds, it is not surprising that the maximum in the longwave CRE is located in and slightly ahead of the warm frontal region as this is where the highest cloud tops are found in the composite cyclone (see Figure 3.3). The net CRE is dominated by the shortwave CRE and is negative throughout the domain. Shortwave and longwave CRE largely cancel in the warm frontal region, shifting the maximum of the net

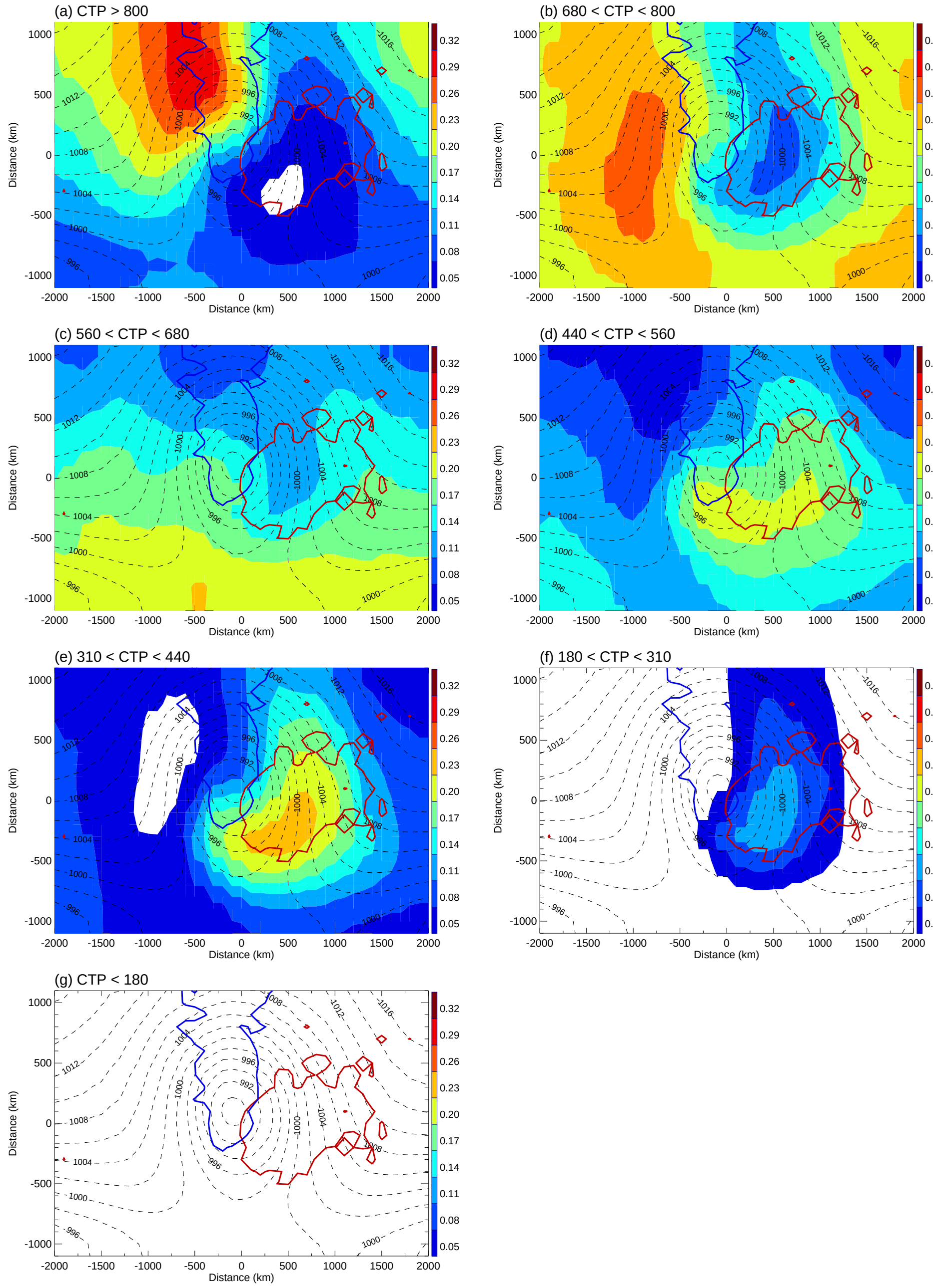

Figure 3.3: Composited ISCCP cloud cover in seven CTP classes (colored field), and MSLP (hPa, black dashed line) related to cyclones occurring in the period 2000-2001 between 40°S-50°S.

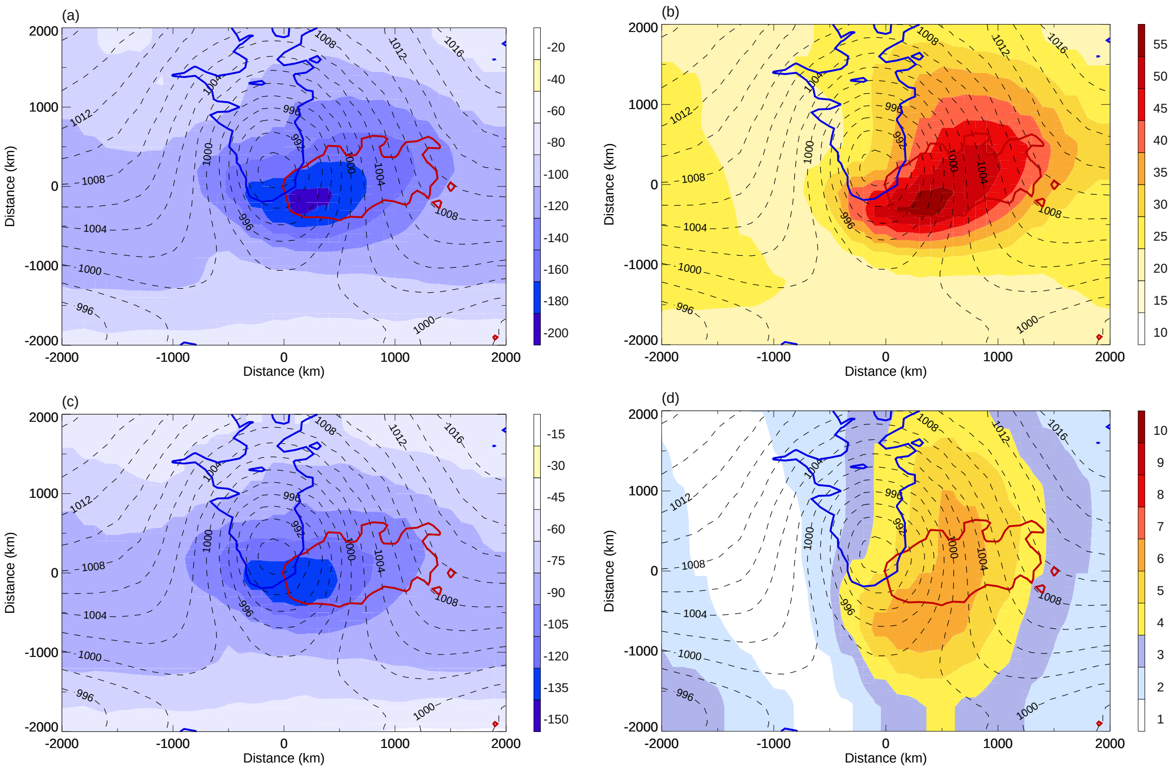

Figure 3.4: Cyclone composite CRE, MSLP and precipitation. MSLP is contoured, the radiation and precipitation fields are shaded and the isolines of the occurrence of cold and warm fronts are shown by blue and red lines respectively. (a): Shortwave CRE (W/m^2). (b): Longwave CRE (W/m^2). (c): Net CRE (W/m^2). (d): Precipitation (mm/day).

CRE to the south and south-east of the cyclone center (cf. Fig. 3.4(c)). This result highlights the importance of the low clouds, which are not necessarily related to the frontal regions, in determining the net CRE of extratropical cyclones on the climate system (e.g. Tselioudis and Rossow (2006)).

Figure 3.4(d) shows the distribution of precipitation around the composite cyclone. The area of maximum precipitation lies within and ahead of the warm frontal region, consistent with the location of deep clouds. The significant displacement of the rainfall and cloud maxima to the southeast of the warm frontal region is due to the tilted structure of the cloud systems. As the fronts are determined at 850 hPa and the cloud structure is tilted, the maximum rain is found ahead of the fronts. Maximum rain rates are in the range of 6-7 mm day^{-1}. Most of the rain is associated with the warm conveyor belt, consistent with the previous studies (Field and Wood, 2007; Harrold, 1973). The western edge of the domain shows relatively high values of rain rate very likely due to the fact that the compositing method detects cyclones that follow those induced in the main composite.

Passive remote sensing is limited to cloud top or cloud base properties depending on the location of observing system (in space or on the ground). For the space-based system used here, if there is a high top cloud, the passive instruments often have difficulty to detect clouds below it. The more recently available active sensors on the CloudSat/CALIPSO satellites alleviate this problem and provide cloud observations with high vertical resolution. In the following subsection we combine these active observations of clouds with reanalyses of the circulation and thermodynamic cyclone structure to form a more complete composite picture of the Southern Ocean extratropical cyclones.

3.4 A three-dimensional view of the composite cyclone

To construct a three-dimensional picture of the cloud structure around the composite cyclone, the 2B-GEOPROF-LIDAR product is used as it combines the Cloud Profile Radar (CPR) data from the CloudSat satellite with the CALIOP lidar data from the CALIPSO satellite (Mace et al., 2009). The 2B-GEOPROF-LIDAR product provides a cloud mask at 240m vertical and 1.14 km (cross-track) horizontal resolution. Cloud is considered to be present anytime if either the CloudSat radar

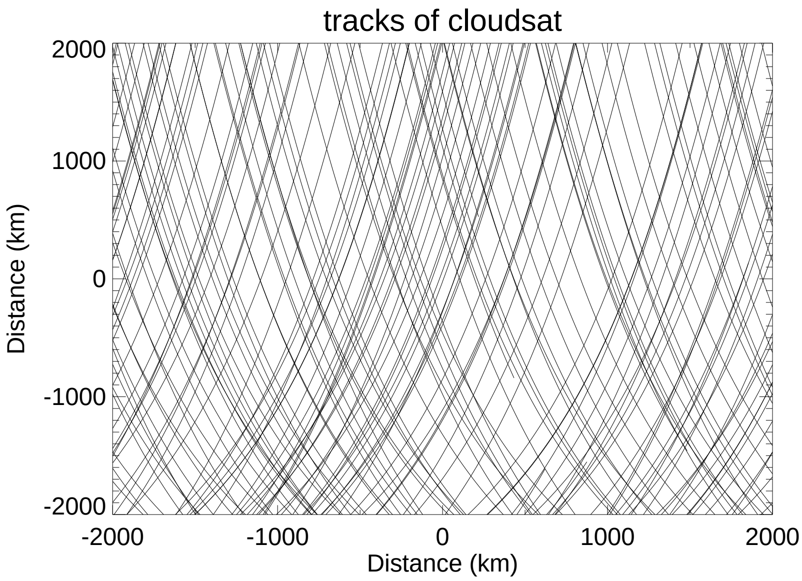

Figure 3.5: Available Cloudsat tracks for 96 cyclones in one month.

indicates the existence of a cloud (i.e., a cloud mask value of 30 or higher) or the CALIOP lidar indicates that the radar bin in question contains 50% or greater cloud cover.

The cyclone data is available every six hours and we assign Cloudsat/CALIPSO orbits to a cyclone if they cross the identified cyclone area $\pm$ 3 hours from the cyclone time. For each of the cyclones in the composite, all of the CloudSat/CALIPSO orbits intersecting the 4000 km $\times$ 4000 km cyclone area box are found. As with the analysis of fronts the cyclone area box is divided into 100 km $\times$ 100 km boxes and GEOPROF pixels are assigned to the appropriate box for each cyclone. The cloudy and total pixels falling into each box are counted to give the cloud fraction in each 240-m height bin around the composite cyclone. Because of the high reflectivity of the surface in the radar returns, CloudSat cannot detect hydrometeors in the first kilometer above the surface (Marchand et al., 2008). The cloud data for first 1 km is discarded here for this reason. It is also worth noting that the radar cannot easily distinguish between cloud and precipitation hydrometeors and thus precipitation is included in the cloud mask used here. We investigate possible effects of this choice further in Chapter 5.

Figure 3.5 shows all available CloudSat/CALIPSO tracks if only 96 cyclones occurring in May 2008 are included in the composite. With every track, only a very thin slice of cloud data is available. It is evident that the data is distributed very unevenly over the 4000 km $\times$ 4000 km cyclone area box. Some grid boxes have no data available at all while some have many data points. Figure 3.6 shows cloud fraction

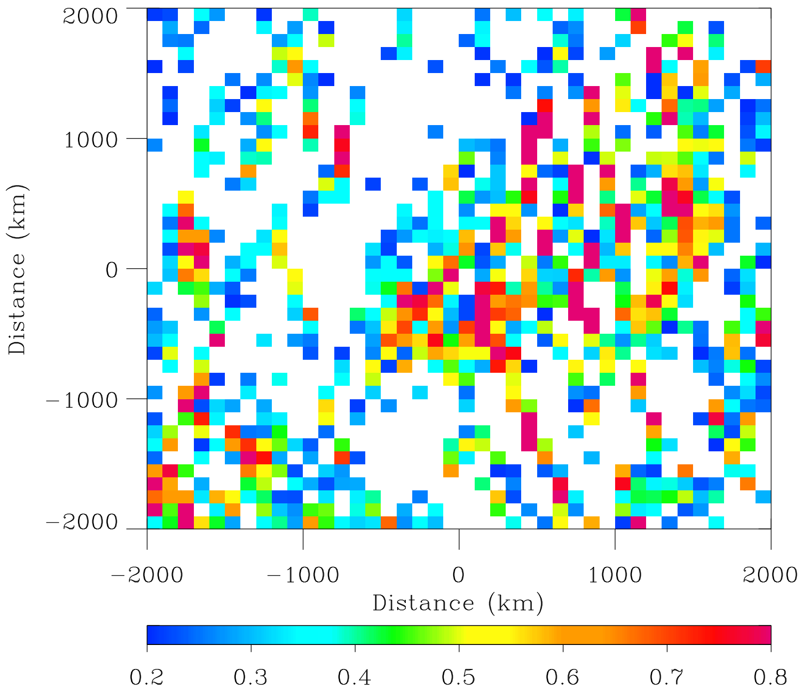

Figure 3.6: Cloud fraction derived from 96 cyclones in May 2008 at 4.25 km height from CloudSat/CALIPSO tracks.

derived using only the 96 cyclones above at height 4.25 km. It is evident that the cloud pattern is extremely noisy with little coherence. As a consequence, it is very difficult to draw any conclusion about the clouds related to cyclones. This figure demonstrates that a much larger number of cyclones is needed to get a meaningful picture of clouds from CloudSat/CALIPSO. Here we use two years data covering all cyclones in the 40^0S-50^0S latitudinal band. Of the 3163 cyclones found in the year 2007 and 2008, 2038 have Cloudsat/CALIPSO orbits intersecting them in the 6 hour period covering three hours before and after the time of cyclone. These were used to form the composite of the cloud structure shown below.

Figure 3.7 shows the vertical profile of cloud fraction averaged over a 4000 km x 4000 km grid box (black line) around the cyclone center as a function of height. At lower levels, the values of cloud fraction are much higher than those at higher levels consistent with high cloudiness at low levels in the Southern Ocean (Haynes et al., 2011). From 1 km height to 3 km height, the cloud fraction decreases from 0.54 to 0.22 and then remains fairly constant between 3 and 9 km height, above which cloud fraction decreases to zero at around 11-12 km. The difference between values of cloud fraction at different heights indicates the presence of a multilayer cloud structure in extratropical cyclones.

The 4000 km x 4000 km grid box around the cyclone center is divided into four

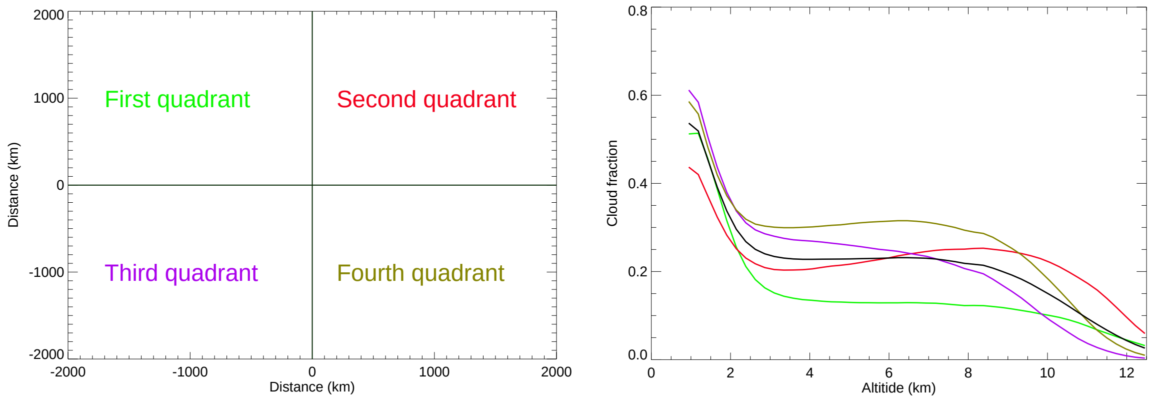

Figure 3.7: Cloud fraction as a function of height averaged over the 4000 km x 4000 km grid box around the cyclone center and its four quadrants. The black line shows the domain average, while the coloured lines represent the quadrants shown on the left.

quadrants as shown in the left panel of Figure 3.7 and the cloud fraction averaged over each of these four quadrants is shown in the right panel of Figure 3.7. All quadrants show the existence of low level clouds peaking just below 2 km. The second quadrant being the north- east part of cyclone has fewer low level clouds than other parts of the cyclone. However, the values of cloud fraction in this area gradually increase from 3 to 9 km height to a maximum above 9 km height indicating a shift of the clouds in the cyclone towards the north-east side of the cyclone center at very high levels. The first quadrant shows clouds behind the system and has fewer clouds above 3 km. The third and fourth quadrants have most of the clouds from the warm frontal regions and show high cloud fraction between 3-6 km height. Above 6 km, the cloud structure moves eastward of the cyclone center and thus values of the cloud fraction becomes highest in the fourth quadrant.

The three-dimensional structure of the cloud and dynamical fields of the composite cyclone is constructed using the methodology described above. Figure 3.8 shows the horizontal distribution of cloud cover taken at different heights. For orientation, we overlay the positions of the cold and warm fronts as thick blue and red lines respectively.

Figure 3.8(a) shows the mean cloud field at a height of 1.5 km together with the composite MSLP. The center of the composite cyclone with its minimum pressure of $\approx 992hPa$ is clearly identifiable. The low level cloud maximum is well aligned with the pressure structure with a NW-SE tilt extending to the western side of the cold-front region. Low clouds are also prevalent to the southern side of the cyclone

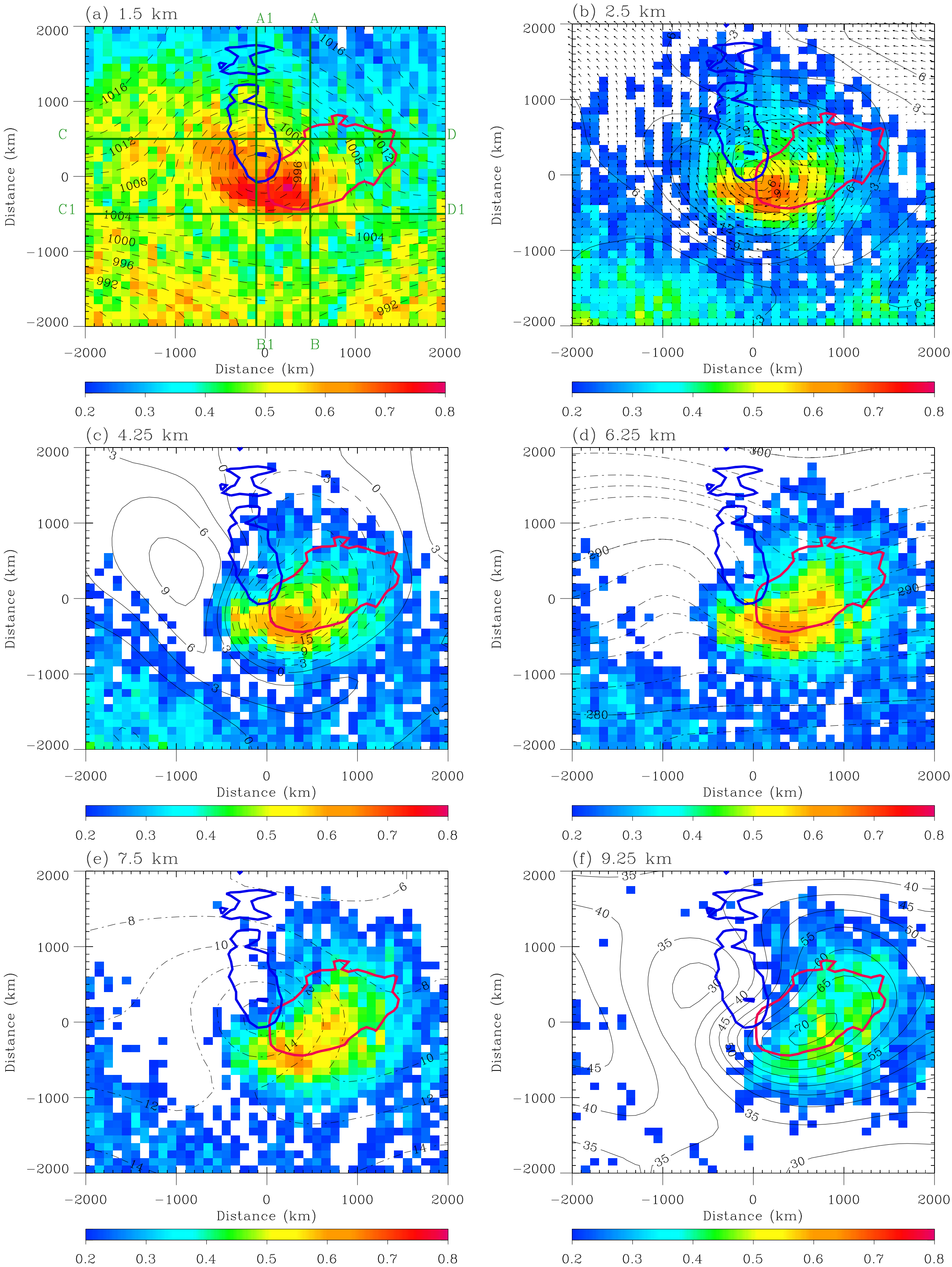

Figure 3.8: Cloud and dynamical structure of the the composite cyclone. Dynamical fields are contoured, cloud fields are shaded and isolines of the occurrence of cold and warm fronts are shown by blue and red lines respectively. Lines CD and AB indicate the position of the cross-sections shown in Figure 3.9 (a) and (b) respectively. (a): Cloud fraction at 1.5 km and mean sea level pressure (hPa). (b): Cloud fraction and system relative winds (m/s^{-1}) along with their corresponding wind vectors at 2.5 km. (c): Cloud fraction and vertical motion (10^{-2} Pa/s) at 4.25 km. (d): Cloud fraction and potential temperature (K) at 6.25 km. (e): Cloud fraction and absolute vorticity at 7.5 km. (f): Cloud fraction and relative humidity (%) at 9.25 km.

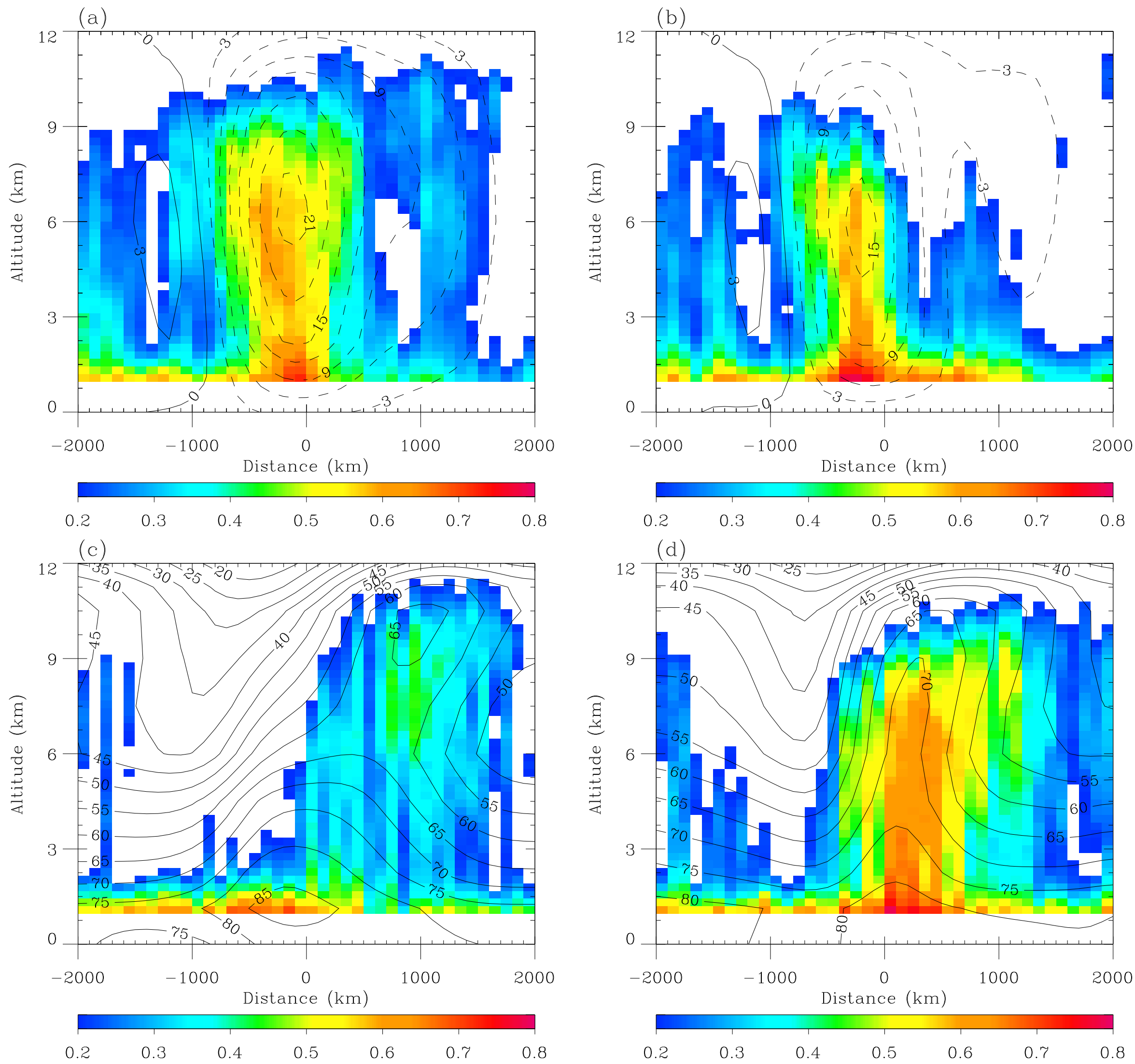

Figure 3.9: (a): Cross section of vertical motion (10^{-2} Pa/s) and cloud fraction along the line AB in Figure 3.8. (b): Cross section of vertical motion and cloud fraction along the line A1B1. (c): Cross section of relative humidity (%) and cloud fraction along the line CD. (d): Cross section of relative humidity (%) and cloud fraction along the line C1D1.

center consistent with the mean cloud distribution over the Southern Hemisphere (Haynes et al., 2011), which shows ubiquitous low cloudiness of high cloud fraction over much of the Southern Ocean south of 40°S.

Figure 3.8(b) shows the mean cloud field at height 2.5 km together with the system relative wind displayed as wind vectors. The maximum winds are found behind the system and to the right of the cyclone center. Some of the strongest winds are found in the warm frontal region. The wind turns cyclonically around the cyclone center and indicates a closed circulation. The warm air from the north-east part of the cyclone turns cyclonically into the warm frontal region. The cold air from south of the cyclone center travels rearward of the main system. The strongest winds are flowing rearward underneath the warm rising air, consistent with the existence of a cold conveyor belt, which flows at low levels rearward relative to the cyclone center producing a low-level jet that undercuts the warm conveyor belt. The cloud fraction values peak in the warm frontal region and in the south-west corner of the cyclone. The dry air turning cyclonically corresponds to the cloud-free region at the western side of the cyclone center.

Figure 3.8(c) shows the vertical velocity in pressure co-ordinates, omega(ω=dp/dt) and cloud fraction at height 4.25 km. Negative ω, denoted by dashed lines, indicates regions of ascent while positive ω (solid black line) denotes regions of subsidence. The vertical motion field has a dipole structure with ascent to the E-NE of the cyclone center peaking in the warm front and to a lesser extent cold front regions, with subsidence to the W-SW of the cyclone center with a strong peak to the west of the cold front region. Not surprisingly the cloud field at this height (tyically termed mid-level cloud) follows the vertical motion field with a distinct maximum in cloud fraction within or just ahead (to the south) of the warm front region. A secondary maximum in mid-level clouds is visible at the Southern edge of the the composite domain, again consistent with Haynes et al. (2011) who showed a maximum in mid-level clouds south of 55°S over the Southern Ocean.

Figure 3.8(d) shows the mean potential temperature and cloud fraction at 6.25 km. The thermal trough, associated with subsidence, is situated to the west of the cold front and surface low, while the thermal ridge, associated with ascent is situated along the eastern side of the warm front. The maximum cloud fraction is located well to the south-east side of the cyclone center and poleward of the warm front region. Recalling that the fronts were identified at 850 hPa, this is consistent with the tilted cloud structure of warm fronts (see also Fig. 3.9) in conceptual and theoretical models of extra-tropical cyclones.

Figure 3.8(e) shows the absolute vorticity and cloud fraction at 7.5 km. It indicates a closed cyclonic circulation at the center of the composite cyclone. The maximum of the absolute vorticity lies in the region of convergence. The cloud fraction decreases at this level and achieves its maximum in the south-east part of the cyclone. There are no clouds behind the system at this height.

Finally, Figure 3.8(f) shows the cloud fraction and relative humidity (with respect to liquid water) at 9.25 km. There are high level cirrus clouds on the east side of the cyclone center just east of the warm frontal region. The relative humidity maximum coincides with the cloud maximum, while regions with low relative humidity coincide with the cloud-free regions to the west of the cyclone center. The values of relative humidity are much higher in the eastern part of the cyclone center than the western part. The cloud structure relative to both the cyclone center and the regions of the 850-hPa warm fronts is consistent with the classic cyclone picture of warm air rising along the warm conveyor belt through the cyclone center to the South and then East.

As we have quasi-contineous observations of cloud cover in the vertical direction, we can construct vertical slices of the cloud structure. Through these vertical sections, changes in the cloud field with height are easily identifiable. Also the tilt in the cloud field is easily seen in these vertical sections. Four cross-sections have been chosen (they are indicated in Figure 3.8(a)), first, an east-west cross-section passing through both the cold and warm frontal region, second, an east-west cross-section taken in the region of maximum cloud fraction at mid-levels, third, a north - south section through the middle of the warm frontal region, and fourth, a north-south cross-section through the cold frontal region.

Figure 3.9 (a) shows a north-south slice of the three-dimensional cloud structure together with vertical velocity ω taken at (relative) 500 km to the east of the center (along line AB). It is evident from Fig. 3.8 that the cross-section taken along line AB crosses the warm-front region, which extends from roughly 1000 km south of the cyclone center to 1000 km north of the cyclone center. Low clouds and subsidence dominate the region south of the main warm-frontal zone. Cloud cover maxima at 1 km and 7 km dominate the main warm-frontal zone, with maximum cloud height increasing northward along the section reaching levels between 10 and 11 km.

Figure 3.9 (b) shows a north-south slice of the cloud fraction along with ω taken at (relative) 100 km to the west of the center (along line A1B1). This section crosses the cold-frontal region as shown in the Figure 3.8. At very low levels the cloud fraction shows higher values consistent with Figure 3.8(a). The cloud field peaks at about 6 km which is consistent with values of ascent in the region. It expands at the southern side of the cyclone center reaching a height of 10 km. The north side being the cold frontal side of the composite cyclone shows some clouds at 0-1000 km distance from the cyclone center up to 7 km height.

Figure 3.9 (c) shows an east-west slice of the cloud fraction taken at 500 km north of the center (line CD). The superposed field is relative humidity. Low clouds dominate the western half of the cross section consistent with Fig. 3.8(a). These clouds exist in a region of low mid - and upper tropospheric relative humidity and a strong vertical relative humidity gradient at around 3 km, consistent with the post frontal region of subsidence identified in Fig.3.8. Cloud fraction in this region is very high around just above 1 km accompanied by high relative humidity. Note that the low cloud maximum extends into the eastern half of the cross section, indicating the ubiquity of boundary layer clouds over the wet ocean surface found in many earlier studies (Rossow and Schiffer, 1999; Haynes et al., 2011). The eastern half of the cross section exhibits a tilted cloud and humidity structure closely following the conceptual model of air ascending along the warm conveyor belt in the E-NE part of the cyclone leading to cloud formation along the air parcel's trajectories. The maximum cloud height is about 11 km with a cloud cover maximum at around 9 km.

Figure 3.9 (d) shows an east-west slice of the cloud fraction taken at relative 500 km south of the center (line C1D1). This cross-section is taken where the maximum of cloud cover was found at mid- levels (Figure 3.8). The cloud fraction is maximum at 1.5 km accompanied by a maximum of relative humidity. Cloud fraction is higher to the eastern side of the cyclone center with the cloud field extending eastward reaching a maximum cloud height of approximately 11 km. At low levels, there are some clouds to the western side of the cyclone center associated with descending motion.

To bring the three-dimensional information together in a coherent picture, the cloud field is drawn in three-dimensions. Figure 3.10 shows two examples of this three-dimensional view of the cloud field related to the composite cyclone. In this figure, the X,Y and Z axes are shown with the red, green and blue arrows, respectively. The upper panel shows the view of cloud fraction through the XZ plane from

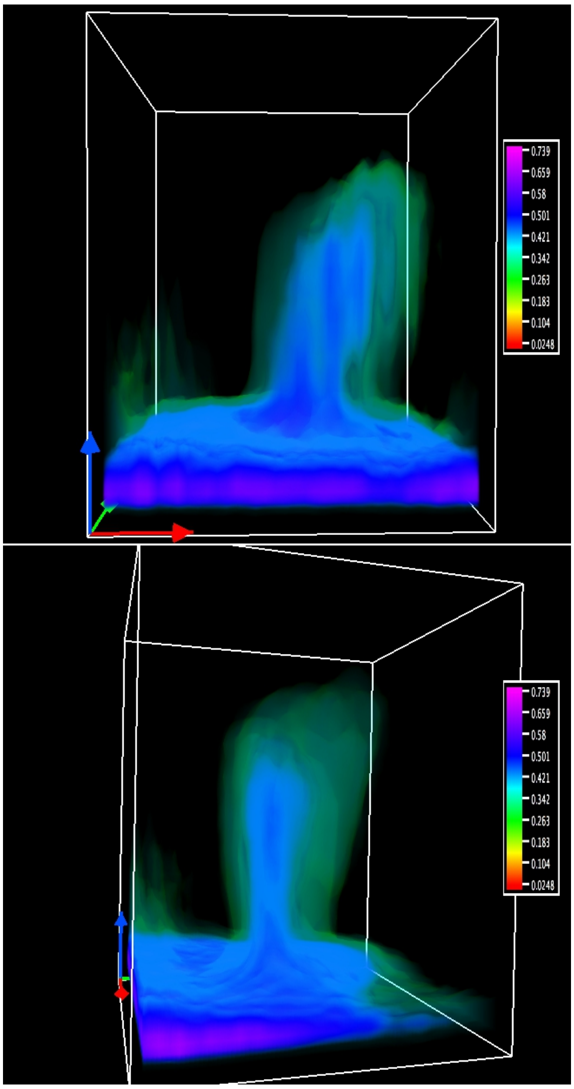

Figure 3.10: Clouds related to composite extratropical cyclones, shown in the three dimensions. The colour denotes values of cloud fraction.

the south while the lower panel shows cloud field view from the YZ plane from the east. The tilted structure of the cloud field can be easily seen. There are two peaks in the cloud field, one is at very low level and another at upper levels. The main 'stormy' clouds are at mid-levels, and are surrounded by thin cirrus clouds. The upper-level clouds have a smaller horizontal extent than those at the lower levels.

Taken together, the cloud fields depicted in the Figures 3.8, 3.9 and 3.10 are consistent with the classical conveyor belt picture of extratropical cyclones (e.g. Browning and Roberts (1994)). Air parcels ascend and form cloud, while traveling southward ahead of the cold front in the warm conveyor belt. These air parcels ascend over the warm front before turning anticyclonically at upper levels. On the cold side the cold front air parcels subside producing the characteristic postfrontal dry slot.

3.5 Trajectories of air parcels in the airflow of cyclone

It is important for climate models to represent the dynamical processes and airflows of extratropical cyclones in order to be able to correctly predict the clouds. As clouds are formed by the dynamical processes, if those are poorly represented in the model then there is no reason to believe that the model will produce the clouds with the right properties in the correct locations. To prepare for the evaluation of clouds in Chapter 5, the next two subsections will introduce two different ways to study the dynamical features of the composite cyclone and their relationship to the cloud field.

First, 48 hour back trajectories are drawn in the Figure 3.11 at three different pressure levels, 850 hPa, 500 hPa and 250 hPa. The path followed by an air parcel in the composite cyclone flow can be traced using these trajectories. The black dots in the figure denote the end point of each trajectory. Using a linear interpolation, applied to the composite of the u, v and w components of the wind, the path followed by the air particle is traced back for every hour. Each trajectory in the Figure 3.11 is constructed by accumulating this hourly information. The colour of the trajectories in the figures denotes the difference in pressure level the air parcel was found on every hour. A positive pressure difference denotes ascending motion (i.e. the air parcel has moved from higher to lower pressure) while a negative pressure difference denotes descending motion (i.e. the air parcel has moved from lower to higher pressure).

At 850 hPa, descending southerlies are dominant to the western side of the cyclone center. The cold air descends and some of this air flows rearwards, relative to the advancing system parallel to and on the cold side of the warm front, comprising the cold conveyor belt (Schultz, 2001). The warm air from the north side of the cyclone center ascends and turns cyclonically near the center. Consistent with Figure 3.8, there is ascending motion in the south-west corner of the cyclone area box.

At the 500 hPa level, both ascending and descending motion are evident. At the cyclone center, air rises up approximately 5-10 hPa per hour. The air rises southwards and splits into two parts. Some part of it rises on the warm frontal region and turns cyclonically near the center. The other part rises and turns anticyclonically. The western side of the cyclone center shows descending motion.

Strong westerly motion is dominant at 250 hPa. The air near the cyclone center ascends and turns anticyclonically to the eastern side of the cyclone center.

The values of cloud fraction along the trajectories is shown in the Figure 3.12. At 850 hPa, the minimum value of the cloud fraction is 0.25 and it reaches up to the value of 0.75 near the center of the composite cyclone. Consistent with Figure 3.8 values of cloud fraction along the trajectories are highest at this level, compared to the other levels in this figure. At 500 hPa, trajectories in the region of ascent show higher values of cloud fraction while trajectories in the region of descent show lower values of cloud fraction. The trajectories ending near the center of the composite cyclone show the highest values of the cloud fraction at this level. At the 250 hPa, the values of the cloud fraction are small. The trajectories ending at the far eastern side of the composite cyclone center show moderate values of cloud fraction. Trajectories ending in the western part of cyclone and near the center show very small values of cloud fraction at this level.

Figure 3.13 shows the values of relative humidity along the trajectories. Consistent with higher values of cloud fraction found, higher values of relative humidity are evident at 850 hPa level. The region of descent contains trajectories having 50-75% relative humidity while the region of ascent contains trajectories with the highest relative humidity values. At the 500 hPa level, the highest relative humidity is found along the trajectories ending near the center and at the eastern side of the cyclone center. The trajectories at western side of the cyclone center show moderate values of the relative humidity. At the 250 hPa level, the trajectories ending at the far eastern side of the cyclone center shows moderate values of relative humidity consistent with moderate values of cloud fraction found in the region in Figure 3.12. The trajectories ending elsewhere show small values of relative humidity at this level.

The results of the trajectory analysis are consistent with those in Figures 3.8, 3.9 and 3.10 and agree well with the conceptual model of cyclones. A stream of dry air (the dry intrusion) descends from the lower stratosphere behind the cyclone and fans out. Some of the air turns anticyclonically and some air turns cyclonically and ascends into the warm front. This cyclonic path is associated with the cloud-free region. The warm conveyor belt is a warm, moist synoptic scale flow of air, which advances southwards ahead of the cold frontal region and then splits into two air flows. One air flow ascends along the warm frontal region and then turns cyclonically to form the upper part of a cloud head. The second air flow peels off anticyclonically from the warm conveyor belt and ascends, broadening the cloud band at upper-levels.

3.6 Linking clouds and dynamical fields

Cloud structures are invariably linked to the internal circulations that accompany the cyclone. Above we derived the three dimensional structure of clouds related to a composite extratropical cyclone in the Southern Ocean along with three dimensional dynamical fields. Our goal here is to quantify the relationships between the dynamical fields and the cloud field. Two dynamical variables which are important for the formation and dissipation of clouds, namely, vertical motion and relative humidity, are considered. Each of the three variables, vertical motion, relative humidity and cloud fraction, will be drawn in terms of remaining two variables to identify the relationship between them. This analysis will be done at three different heights to see how this relationship changes with the height.

The left panels of Figure 3.14 show the relationship between cloud fraction, vertical motion and relative humidity at three different heights. In these panels, the vertical motion is drawn on the X-axis, relative humidity is drawn on the Y-axis and colour of the points denotes the value of cloud fraction. The coloured boxes drawn on the left panels denote areas of particular interest. The purple colour box includes the points where the highest relative humidity and the highest ascent value are achieved. The red box has the points where the values of relative humidity and ascent are medium. The light green box contains those points where the values of vertical motion are close to zero and relative humidity is low while the dark green box accommodates points having the strongest values of descent and small values of relative humidity. The black solid line shows the zero value of vertical motion. The right panels of Figure 3.14 shows the position of points in the particular coloured box related to the (composite) cyclone center. The colour showing the position of the point in the right panel and the colour of the box in the left panel of the figure in which that point is contained, are matched.

The relationship between the cloud and dynamical fields at 1.5 km, 4.25 km and 9.25 km height is shown in the panels (a), (c) and (e) of Figure 3.14, respectively. It is evident that this relationship does change with height. The range of all variables

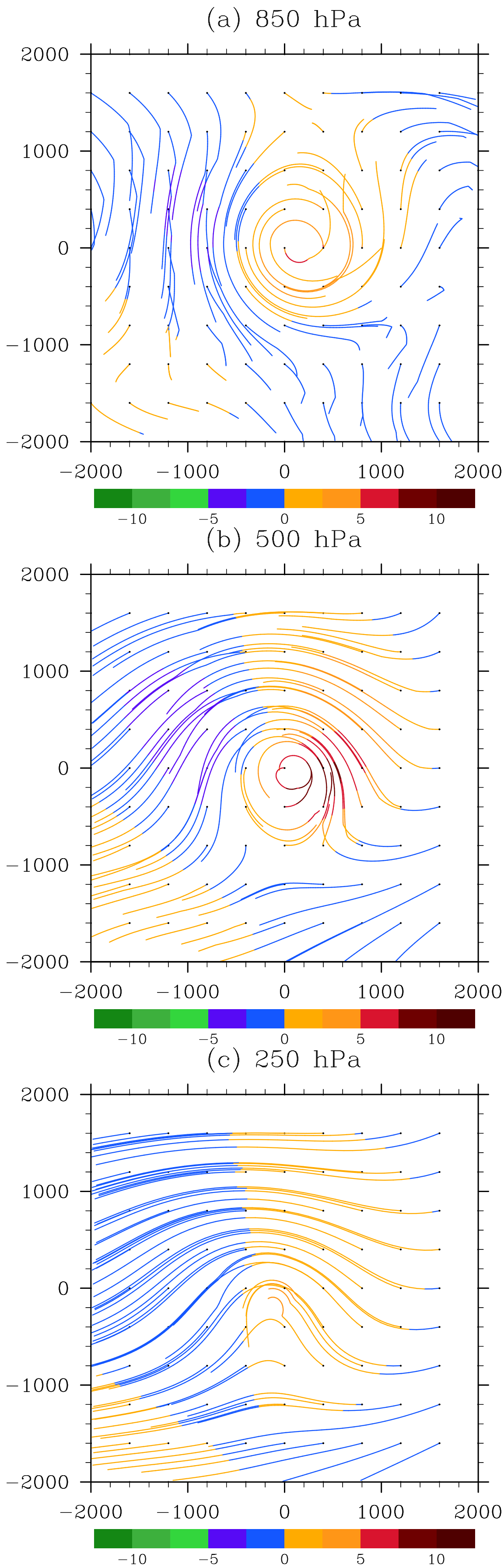

Figure 3.11: 48 hours back trajectories at (a) 850 hPa, (b)500 hPa and (c) 250 hPa for the composite cyclone. The colour of the trajectory denotes the difference in pressure level every hour. The end point of the trajectory is shown by black dot.

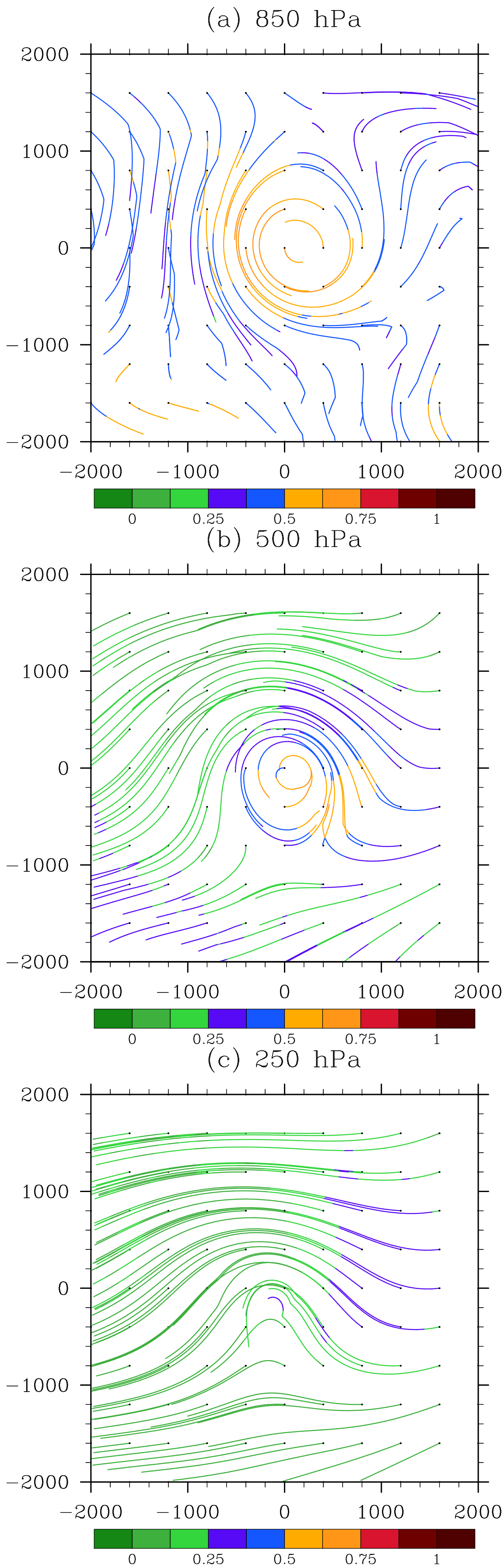

Figure 3.12: 48 hours back trajectories at (a) 850 hPa, (b)500 hPa and (c) 250 hPa for the composite cyclones. The colour of the trajectory denotes the value of cloud fraction. The end point of the trajectory is shown by black dot.

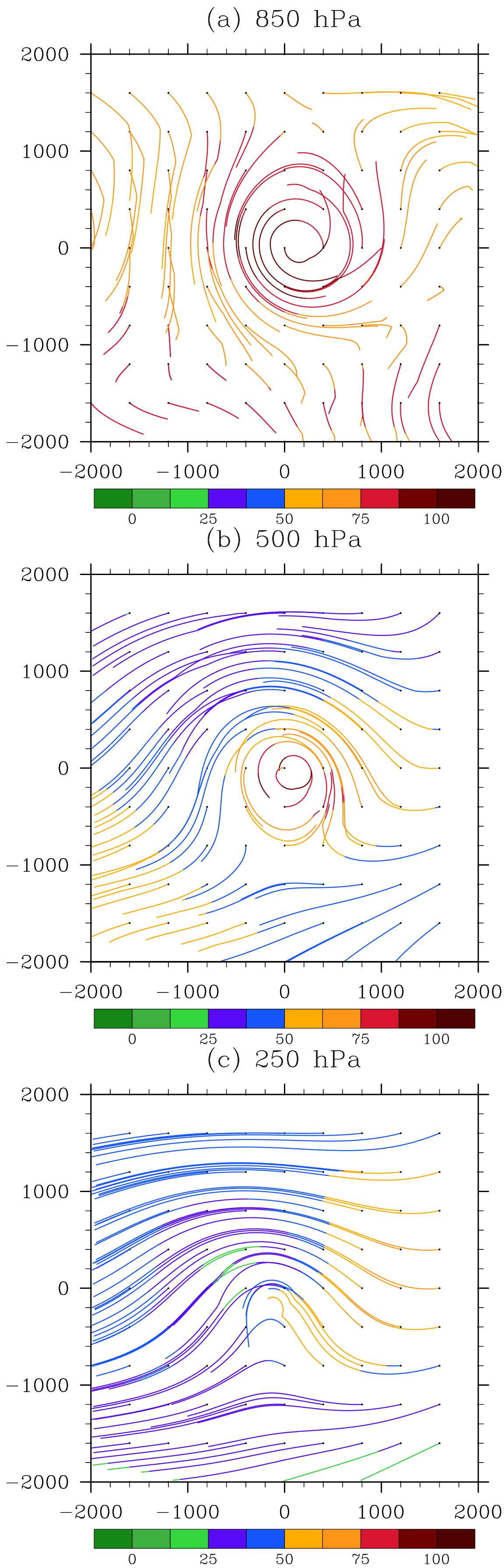

Figure 3.13: 48 hours back trajectories at (a) 850 hPa, (b)500 hPa and (c) 250 hPa for the composite cyclone. The colour of the trajectory denotes the value of relative humidity. The end point of trajectory is shown by black dot.

is large at lower levels while at higher levels it is small. At all levels, the values of ascent are larger than those for descent. At 1.5 km (cf. Figure 3.14(a)), the values of cloud fraction are very high consistent with prevalent low cloudiness of high cloud fraction in Figure 3.8(a). Relatively large cloud fractions exist in both ascending and descending regions with the region of ascent have higher values of cloud fraction than that in the region of descent. Lower cloud fractions are found in regions which have small vertical motion and are relatively dry. The right panel shows that the combination of these variables is not random. The particular regions have special characteristics depending on their position relative to the cyclone center. Very high values of ascent, high relative humidity and high values of cloud fraction is the characteristic of the region at the center and eastern side of the cyclone center. It is surrounded by points which have medium ascent values and are relatively dry. Also, the region at south-west of the cyclone center shows moderate ascent and medium values of humidity. The region of descent is very dry and is at the western side of the cyclone center, behind the system. The remaining regions mainly have small vertical motion and are dry compared to the other parts of the cyclone.

Figure 3.14(b) shows that the range of cloud and dynamical fields gets expanded at mid-levels. Different regions within the cyclone composite occupy distinct spaces in this panel similar to panel (a). The cloud fraction values are smaller at this level than they are at the 1.5 km level. The region of ascent which is very moist has higher cloud fractions and is situated at and to the east of the cyclone center. As at the 1.5 km level, this area is surrounded by a region of medium ascent and relative dryness. The region of descent has low cloud fraction and is dry. The driest part of the cyclone is at north side of the cyclone center, it has the lowest cloud fraction values.

At 9.25 km the range of ω is reduced while there is still a wide variation of relative humidity (cf. Figure 3.14(c)). The region of descent shows low values of cloud fraction while the region of ascent shows moderate values of cloud fraction. The region near the center of cyclone and to eastern side of cyclone center shows medium ascent values and higher relative humidity values. The remaining part of the cyclone is mostly dry and has small vertical motion.

Figure 3.15 shows relative humidity in terms of cloud fraction and omega at heights 1.5 km, 4.25 km and 9.25 km. The values of relative humidity are very high at the lower levels which is consistent with prevalent lower level cloudiness in the region. As the ascent values increase, the value of relative humidity increases.

Small values of ascent or descent corresponds to relative dryness at 1.5 km. Consistent with the Figure 3.14(b) all variables have large range at 4.25 km. Ascent is much stronger than descent at this level. Larger cloud fractions are found to be in the region of ascent. At 9.25 km height the ascending motion weakens. Relative humidity and cloud fraction are not always directly proportional to each other at this highest level. Some points having higher value of cloud fraction and higher ascent values have low values of relative humidity while points having low values of cloud fraction and weak vertical motion have higher values of relative humidity. The relationship between the three variables is not as strong as at other levels here (cf. Figure 3.14(c)).

In Figure 3.16, ω is drawn in terms of cloud fraction and relative humidity. The points showing the highest values of relative humidity and the highest values of cloud fraction also have largest values of ascent at 1.5 km and 4.25 km. At these levels, the relationship between omega, the cloud field and relative humidity is strong. The relationship between the three variables appears quasi-linear. However, at the higher levels, the relationship between the dynamical variables and cloud fraction are weakening. At 9.25 km, all three variables have smaller values compared to the other two levels. At this level, the cloud fraction reaches up to 0.55 and the relative humidity reaches up to 75 %. Ascent is also weak compared to the other two levels.

Overall, quasi-linear relationship between dynamical variables and the cloud field is strong at the lower levels. These relationships become weak at the higher levels. However, it is worth noting that these relationships are representative for a highly averaged composite cyclone and they do not necessarily reflect the behaviour of any individual cyclone.

3.7 Summary of Chapter 3

The goal of this chapter was to provide a three-dimensional composite picture of Southern Ocean extratropical cyclone cloud structures using CloudSat and CALIPSO measurements, together with their associated velocity and thermodynamics fields derived from NCEP-DOE AMIP-II reanalyses.

The composite three-dimensional structure of clouds closely resembles the classical conceptual models (Bjerknes and Solberg, 1922; Posselt et al., 2008; Naud et al., 2010). Progressively thicker high-top clouds are found in the warm frontal region,

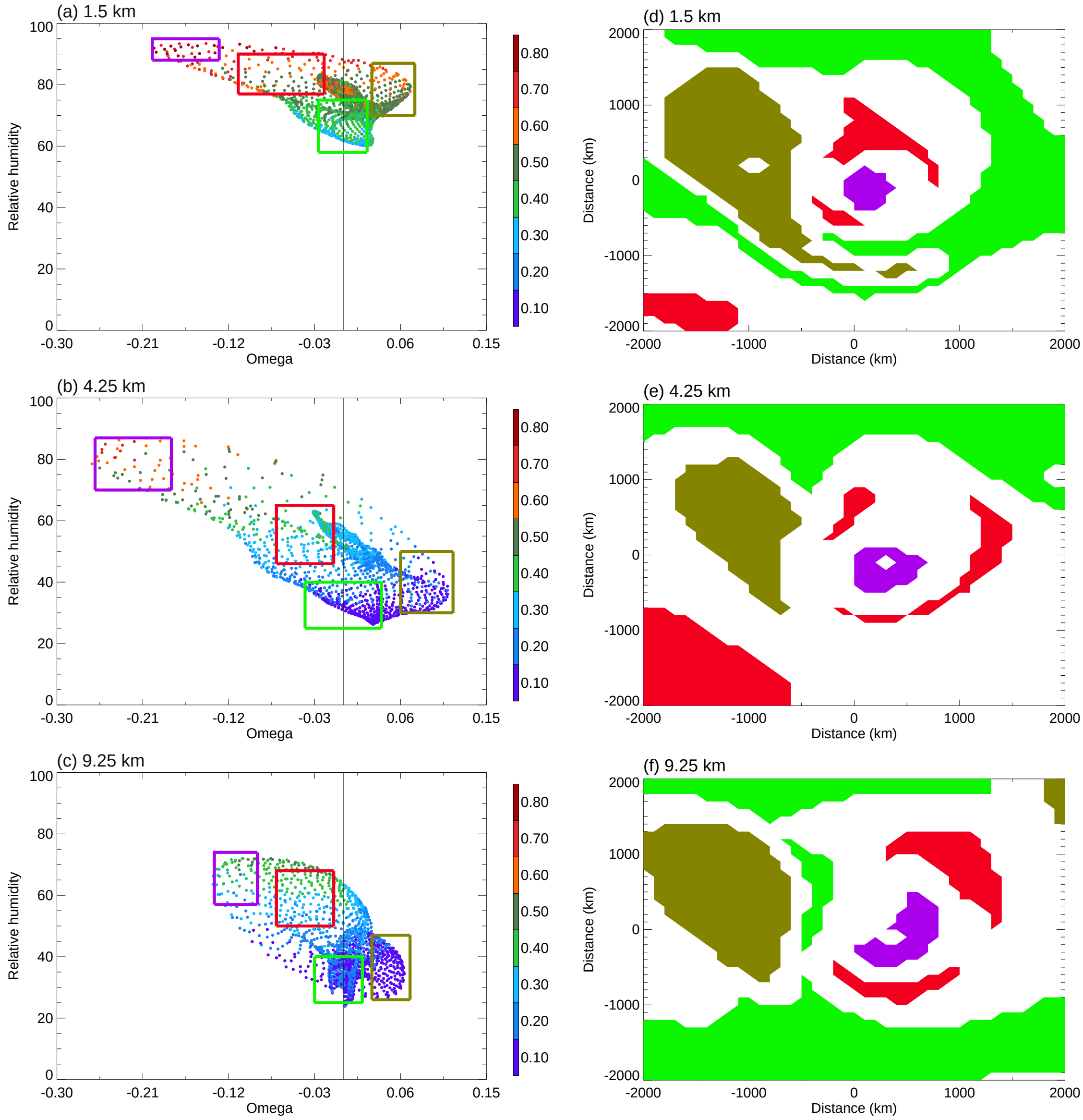

Figure 3.14: Cloud fraction in terms of relative humidity (%) and vertical motion (Pa/s) in the composite cyclone. The colour of the points denotes the value of cloud fraction. The black line denotes the zero value of vertical motion.

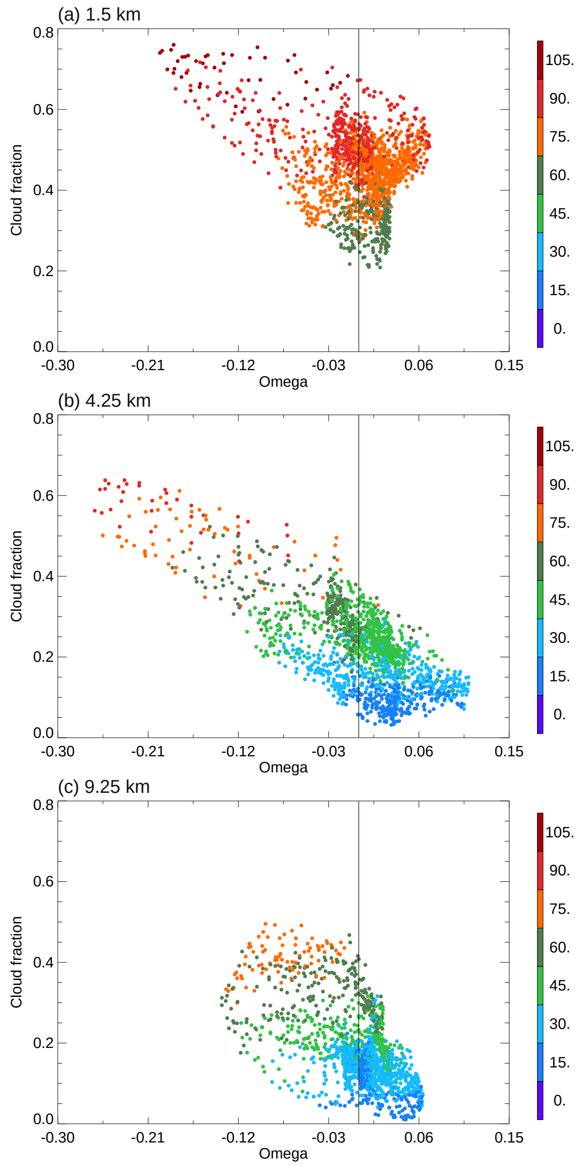

Figure 3.15: Relative humidity (%) in terms of cloud fraction and vertical motion (Pa/s) in the composite cyclone. The colour of the points denotes the value of relative humidity. The black line denotes the zero value of vertical motion.

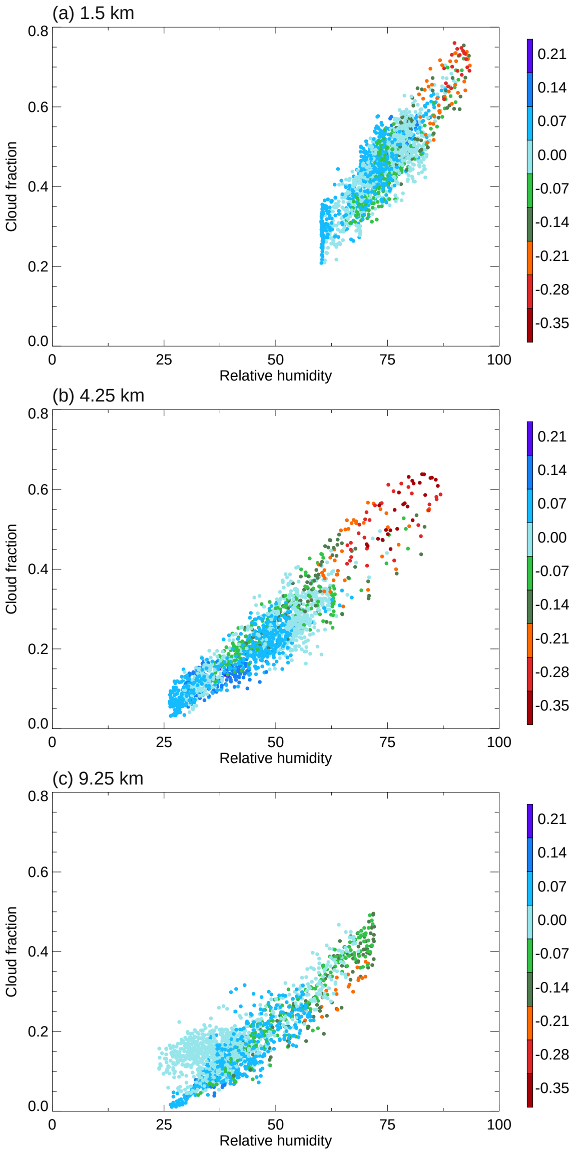

Figure 3.16: Vertical motion (Pa/s) in terms of cloud fraction and relative humidity (%) in the composite cyclone. The colour of the points denotes the value of vertical motion.

which is also the region of maximum rainfall, maximum mid- and upper-level ascent and high relative humidity. Thin cirrus clouds are located at the leading edge of the warm frontal region. A smaller but still significant region of thick cloud and precipitation is located along the cold frontal regions to the north of the cyclone. Mid-level cloud extends to the southeast of the cyclone center. Low-level clouds of various depth are found all around the system and form the dominant cloud type in the northwest sector of the cyclone. Thick and high clouds are essentially absent in that region owing to strong subsidence behind the frontal systems. The strongest net CRE are found near the cyclone center, which is dominated by a net cooling of 90-130 W/m^2.

The relationship between cloud fraction, vertical motion and relative humidity does change with height. The range of all variables is larger at lower levels than that at higher levels. Ascent is stronger than descent in the composite cyclone. A quasi-linear relationship is evident in these three observed variables at lower levels. This relationship becomes weak at higher levels.

Using case studies, Posselt et al. (2008) showed that Cloudsat can serve as a potent tool for model assessment. The methodology developed here provides another innovative opportunity for an in-depth evaluation of climate models. The comprehensive picture of an extratropical cyclone painted by our data analysis will provide the possibility to evaluate the ability of a climate model to simulate the concurrent cloud, dynamical, radiative and precipitation structures of extratropical cyclones in the Southern Hemisphere. This provides a major ingredient to not only understand the mean behavior of models over the Southern Ocean, but to ensure that this behavior is produced from the right combination of physical processes as they act in the major building blocks of Southern Hemisphere weather-extratropical cyclones.

The results of the analysis in this Chapter will be used to evaluate a climate model in Chapter 5. Before doing so, the next chapter will investigate how the relationships between clouds and dynamical fields found here changes with cyclone strength and life cycle.

Chapter 4

Cyclones classes and their related clouds and dynamical fields

Extratropical cyclones occur in a variety of forms and in different evolution stages. Their structure depends on the background flow in which they are embedded, the availability of moisture and the surface conditions (Wallace and Hobbs, 2006). The average properties of a certain group of cyclones can be examined by adding additional criteria to the compositing technique. Many methods to classify cyclones into groups so that each group contains cyclones with the same characteristics have been proposed. Here, one of such method based on cyclone intensity is used to classify cyclones and to study the influence of intensity on cloud cover. The disadvantages of that classification method are discussed and to address them a new classification method is introduced. This new method considers whether a cyclone is deepening or filling as well as assessing its central pressure for classifcation. The compositing method is used to examine changes in the clouds and dynamical fields with the class of cyclone. By compositing cyclones of similar dynamical properties, this chapter aims to provide some insights into the processes that couple the clouds and precipitation to the state of dynamical development of the cyclone.

4.1 Classification of cyclones considering their intensity

In earlier studies cyclones were classified using different parameters. Tselioudis and Rossow (2006) classified cyclones into three groups by using a cyclone's local minima in the MSLP anomaly field and showed that increases in midlatitude storm intensity produce stronger shortwave cooling and longwave warming. Field and Wood (2007) categorized cyclones by their strength which was defined using surface wind and by their water vapor path. They showed that the rain rate and high cloud fraction are positively correlated with cyclone strength defined in that way. Here the composite method will first make use of the classification of cyclones in the MCMS cyclone dataset (Bauer and DelGenio (2006), see Chapter 2). The MCMS cyclone data set provides an index for the intensity of a cyclone by combining the cyclone's absolute minimum MSLP, deepening rate and pressure gradient. This classification sorts cyclones into weak, intermediate and strong categories. This intensity index is used here to classify cyclones. There were 1961 cyclones with intensity 1 which are weak cyclones, 816 with intensity 2 which are moderate cyclones and 162 with intensity 3 which are strong cyclones. All cyclones falling into a particular category are composited using the method described in Chapter 3.

Figure 4.1 shows cloud fractions for all three intensities at height 1.5 km, 4.25 km and 9.25 km. Panels (a), (d) and (g) show cloud fraction and MSLP for intensity 1, 2 and 3, respectively. There is some noise in the results for intensity 3 because of the small number of cyclones. As expected from the intensity definition in MCMS, 'strong' cyclones with intensity 3 show the deepest low with a minimum pressure 970 hPa, 'moderate' cyclones with intensity 2 have a minimum pressure of 982 hPa and 'weak' cyclones with intensity 1 have a minimum pressure of 998 hPa. The cloud fraction has its highest values for the cyclones with intensity 3.

Panels (b), (e) and (h) show cloud fraction and vertical motion at 4.25 km for intensity 1, 2 and 3, respectively. The cloud field exhibits a comma shape to the east of the cyclone center for all cases. The vertical motion field becomes stronger and expands in the east-west direction with increasing intensity. The cloud fraction at this height associated with the rising motion at the eastern side of the cyclone center is highest for cyclones with intensity 3. The region behind the system has very few clouds due to the strong descending motion. There is slight increase in these clouds behind the system with increased intensity.

Panels (c), (f) and (i) show cloud fraction and relative humidity at 9.25 km for intensity 1, 2 and 3, respectively. The maximum of relative humidity matches well with the maximum of cloud fraction for all intensities. These very high-level clouds increase their fractional coverage with cyclone intensity. The maximum of cloud fraction moves eastward of the cyclone center with increasing intensity.

The cloud fraction and dynamical fields associated with the composite cyclones strengthen with increases in the cyclone's intensity. However, there are some limi-

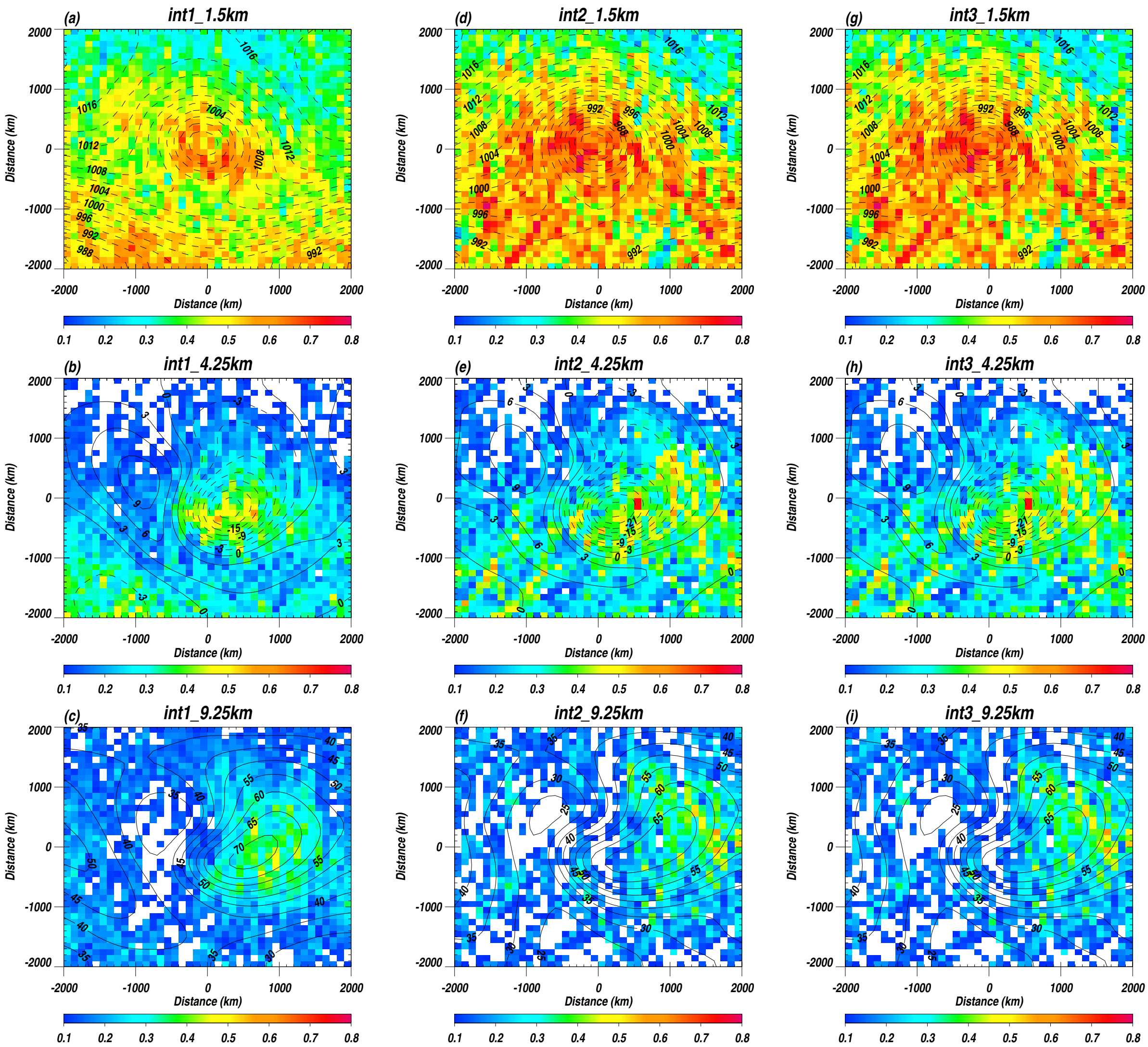

Figure 4.1: Cloud fraction at 1.5 km and MSLP (hPa) for cyclones having intensity 1, 2 and 3 in panel (a), (d) and (g) respectively. Panels (b),(e) and (h) shows cloud fraction and vertical motion (x 10 $^{-2}$ Pa/s) at 4.25 km while panels (c), (f) and (i) shows cloud fraction and relative humidity (%) at 9.25 km for intensity 1, 2 and 3, respectively. MSLP, ω and relative humidity are contoured and cloud fields are shaded.

tations of this classification method. There is major difference in the sample size for the three intensities. The number of cyclones having intensity 3 is very small compared to the number of cyclones having intensity 1. Given the CloudSat/CALIPSO data issue discussed in Chapter 3 the direct comparison of cyclones with these two intensities is difficult. Furthermore, the dynamical conditions for cyclones depend on whether the cyclone is deepening or filling (Carlson, 1994), a characteristic not accounted for in this classification. Considering these issues, a new classification method is introduced below.

4.2 Cyclone classification based on pressure tendency

4.2.1 An improved cyclone classification method

As the dynamical processes are different for cyclones in the deepening stage than that for cyclones in the filling stage, we classified cyclones considering their deepening or filling stage. To find cyclones of similar strength we used only cyclones observed in the JJA season and the 40^0-50^0S latitudinal band for the years 2007-08. The classification is done as follows.

- First all central MSLPs are noted related to all cyclones in the given period and season.

- For each cyclone center, the central MSLP is compared with the reading taken 6 hrs before. If the central MSLP is greater than six hours before then the cyclone is classified as 'filling' while if it is less than or equal to what it was six hours before, the cyclone is classified as 'deepening'.

- Further, as the dynamics will be different for cyclones having higher values of pressure than that for the cyclones having lower values for pressure, each category is subdivided into two classes. The 'deepening' category is divided into two classes: 'High Pressure Deepening (HPD) class' and 'Low Pressure Deepening (LPD) class'. To do so, the median of central MSLP's is calculated for all cyclones in the 'deepening' category. If a cyclone center has a central MSLP greater than that median then that cyclone center falls into the 'HPD class' otherwise it is assigned to the 'LPD class'. The HPD class contains 357 cyclones and the LPD class 362 cyclones.

- Similarly, the cyclones in the 'filling' catagory are divided into 'Low Pressure Filling (LPF) class' and 'High Pressure Filling (HPF) class'. As for the 'deep-

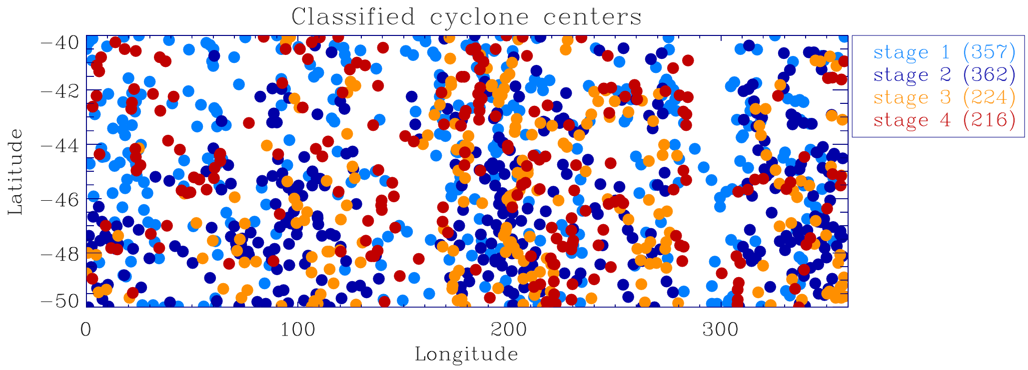

Figure 4.2: Position of all cyclone centers at different stages of their life cycle for JJA 2007 and 2008.

ening' case, the LPF class contains cyclones which have a MSLP less that or equal to the median of the 'filling category', while the cyclones with a central MSLP greater than the median fall into HPF class. The LPF class contains 224 cyclone centers and HPF class 216 cyclone centers.

To investigate if there is any geographic bias in the location of cyclones at different development stage, Figure 4.2 shows the position of all cyclone centers (for two JJA seasons considered for classification) at different stages of their life cycle. Cyclones from all classes are spread all over the region. However, there is a higher overall density of cyclone centers in the western Pacific. It is worth noting that this classification method does not consider the situation where the cyclone is moving into a region of higher or lower climatological MSLP, a situation very common in the Southern Hemisphere (Sinclair, 1994; Lim and Simmonds, 2002). In such cases this classification method has the potential pitfall of being misleading.

To check how our above defined stages relate to the actual lifetime stages of the cyclones, the following method was applied. It is assumed that the ideal cyclone will have four stages in its lifetime. It will be in the developing phase at the first stage, get mature in the second stage, start vanishing in the third stage and in the fourth stage it will be in its decaying phase. To find four stages of the cyclone lifetime, each lifetime cycle was divided into 4 parts. The minimum central MSLP was found for each cyclone. Then the lifetime between the starting position of the cyclone and the position when it achieved minimum MSLP was divided into two parts and these two parts, namely 1 and 2 were considered as the first two stages of the cyclone. The remaining lifetime was divided into two parts and those two, namely 3 and 4, were considered as last two stages of the cyclone. Each cyclone center was assigned a value between 1 and 4 depending on which part of the lifetime of the cyclone it represents. Table 4.1 shows a comparison of the four classes based on pressure tendency and their distribution into the stages of the actual lifetime of the cyclone. The HPD class has the majority of the cyclones in their lifetime stage 1, the LPD class has its majority of cyclones in the second stage, the LPF class has its majority in the 3rd lifetime stage and the HPF class has most of the cyclones in lifetime stage 4. This indicates that our classification which considers the deepening or filling stage of the cyclones matches well with their actual lifetime stage. In general, cyclones start developing in the HPD class, become mature in the LPD class, start declining in the LPF class and are in their last phase in the HPF class. However, there is a significant number of cases that do not follow this simple pattern. This is particularly pronounced in the deepening stages and is the result of the sometimes complex pressure evolution in the cyclone.

One example of this type of cyclone is shown in Figure 4.3. Figure 4.3 shows changes in central MSLP with the lifetime of a cyclone that occurred on 10th October 2007. For this cyclone, the central pressure decreases in the first 20 hours reaching 996 hPa, it then increases to 998 hPa in next few hours. After 34 hours it starts decreasing again and reaches 994 hPa and after 48 hours it starts increasing and reaches approximately 1000 hPa. It fluctuates between 1000 hPa and 998 hPa for some time and again decreases and reaches to 994 hPa at 96th hour. After 96th hour it starts rising again. This cyclone has a lifetime of 108 hours in total and achieves a minimum pressure during its lifetime of 993.6 hPa at 48 hours. So the first 24 hours, the cyclone will be in lifetime stage 1, between 30-48 hours it will be in lifetime stage 2. During 54-78 hours it will be in lifetime stage 3 and after that it will be in lifetime stage 4. However, as the central pressure goes up and down several times, it will enter in deepening and filling classes many times. For example, for this cyclone, at the 18th hour the central MSLP is 995 hPa and at the 24th hour it is 997 hPa. So according to our method, the cyclone will enter the filling category at 24 hours and therefore, it would enter in the LPF class or HPF class while when distributed according to lifetime cycle, it would remain in lifetime stage 1. Because of this type of fluctuations in central MSLP regardless of life time of cyclones, every class in Table 4.1 has cyclones in all life stages.

4.2.2 Rainfall in the pressure tendency classes

To check the viability of our classification method, first the precipitation field related to these classes is composited. The left panels of the Figure 4.4 show precipitation

Pressure tendency classes	**Life time stages**			
	1	2	3	4
HPD class (357)	166	117	39	35
LPD class (362)	127	155	53	27
LPF class (224)	21	41	96	66
HPF class (216)	24	22	54	116

Table 4.1: Comparison of the pressure tendency classes with the stages of the actual lifetime of the cyclone.

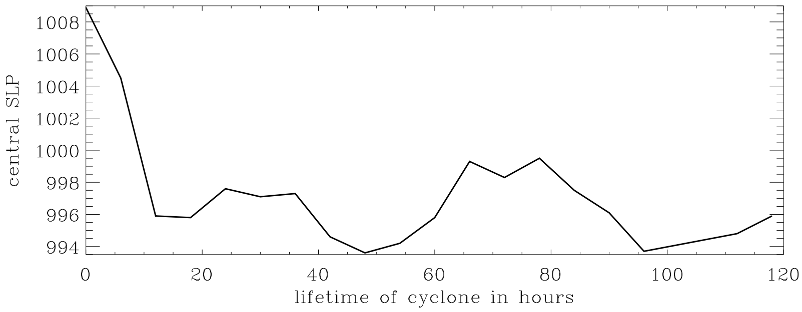

Figure 4.3: Cyclone's SLP (hPa) and lifetime (hours) for an example observed on 10th October 2007.

for the four classes and the right panels show the anomaly of precipitation which is calculated by subtracting the mean of all cyclones in the JJA season in our sample from the individual class fields. As the cyclone progresses, the heaviest rain moves progressively further to the east of the cyclone center and weakens. In the HPD class, rain is concentrated at and near the center of the cyclone. The region at the center is wetter than in the composite of all cyclones. The north-east part of the cyclone center is dry compared to the composite over all cyclones. The rain spreads more over the eastern part of the cyclone in the LPD class. Compared to the HPD class, the rain field extends to the north-west and south-east side of the center and the location of the maximum moves eastward. In the LPF class, the rain field starts shrinking and its maximum moves further east. The far eastern side of the cyclone shows an anomalous increase in the precipitation while there is an anomalous decrease in the precipitation around the cyclone center.

In the HPF class, the rain field becomes stronger at the western corner most likely representing a neighbouring system in the composite. The precipitation is minimum at the center and to the eastern side of the cyclone center. As mentioned above, rainfall gradually decreases with the progressing classes. This is consistent with the study of Rudeva and Gulev (2011) who showed that the precipitation rate decreases 50-70% during the lifetime of a composite cyclone. The evolution of the rainfall field with class indicates that our classification scheme captures key stages of cyclone evolution, encouraging us to proceed in studying the cloud to dynamics relationship in the four cyclone classes.

4.2.3 Clouds in the pressure tendency classes

Figure 4.5 shows cloud fraction at 1.5 km level and MSLP for all stages in the left panels and anomalies of cloud fraction and MSLP in the right panels. Anomalies are again calculated by subtracting the mean of all cyclones in the JJA season in our sample from the cloud fraction and MSLP for all for individual classes (shown in the left panels). Cloud fraction at the 1.5 km level changes according to cyclone classes. In the HPD class, the cloud structure starts developing. In the LPD class the cloud fraction values are highest compared to the rest of the classes. The cloud field starts diminishing in the LPF class and is lowest at the HPF class. As expected, MSLP is minimum for cyclones in the LPD and LPF classes. For the HPD class, the minimum MSLP is 1000 hPa, which is 9 hPa higher than the mean MSLP for all cyclones. The MSLP is minimum in the LPD class with the value of 986 hPa which is 7 hPa less than the mean state. The LPF class has MSLP of 986 hPa and 8 hPa less than the mean state in the eastern side of the cyclone center. In the HPF class the MSLP is 1002 hPa, which is 9 hPa higher than the mean state.

In Figure 4.5 isolines of the occurrence of cold and warm fronts are again shown by blue and red lines, respectively. The region showing a frequent occurrence of cold fronts is situated to the north side of the cyclone center and is most wide in the LPD class. It then shrinks with progressing stages of life cycle. The region showing a frequent occurrence of warm fronts is situated to the eastern side of the cyclone center. The regions showing the occurrence of cold and warm fronts are neatly organized in the deepening classes. In the LPF class, the region of warm fronts gets extended at the eastern side of the cyclone center consistent with the extended cloud structure in the region. The cold fronts have the highest spread in the LPD class while the warm fronts have highest spread in the LPF class when compared with rest of the classes.

Figure 4.6 shows the cloud fraction and the vertical motion at 4.25 km for all stages along with their anomalies from the mean cyclone. For all classes, the vertical motion field follows the cloud field with a comma shaped structure. The ascent is

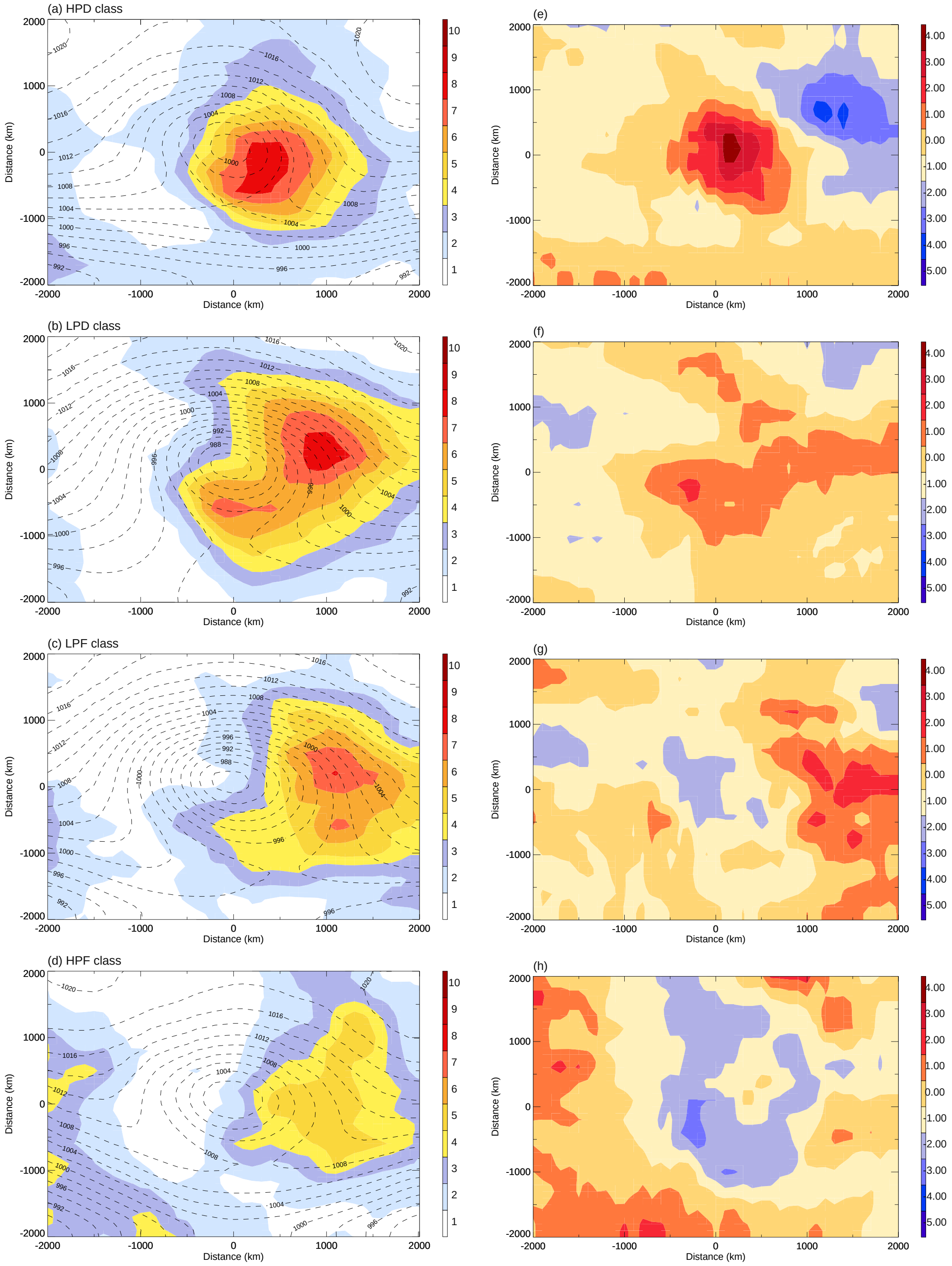

Figure 4.4: Left panels show rain (mm/day) and MSLP (hPa) and right panels show the anomaly of rain for cyclones in the pressure tendency classes. MSLP is contoured and the rain field is shaded.

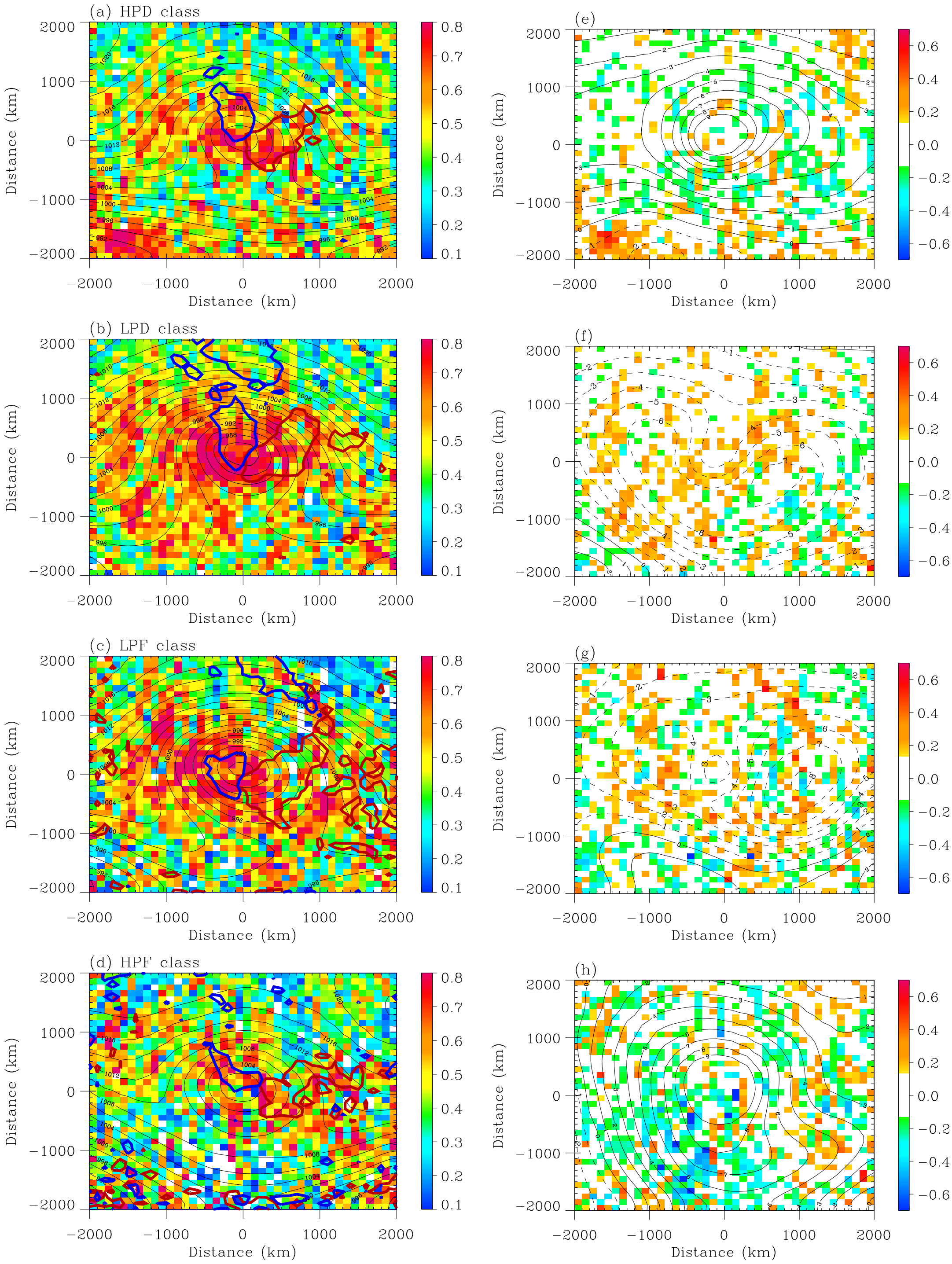

Figure 4.5: Left panels show cloud fraction and MSLP (hPa) and right panels show the anomaly of cloud fraction and MSLP at 1.5 km for cyclones in all pressure tendency classes. MSLP is contoured and the cloud fields are shaded.

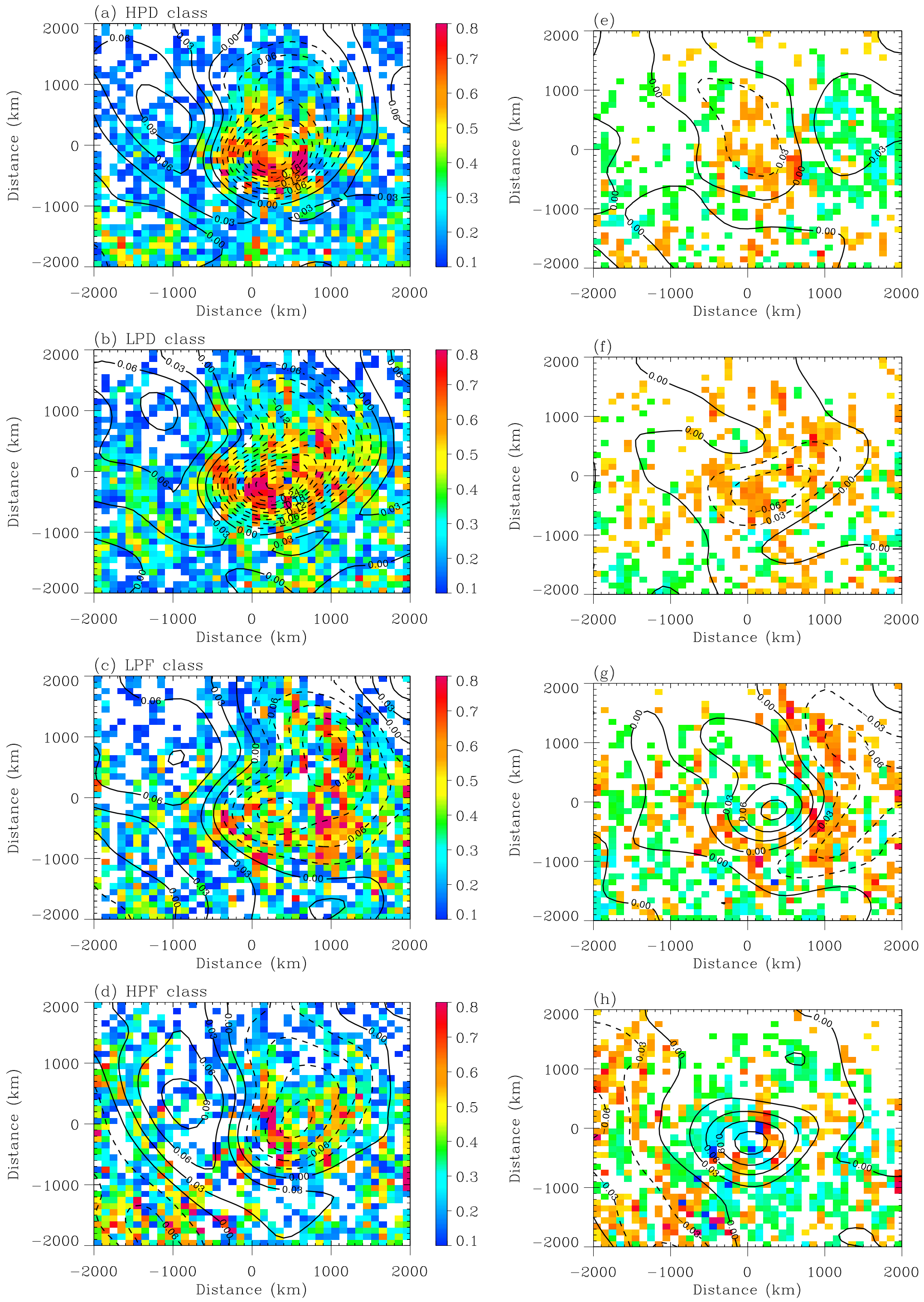

Figure 4.6: Left panels show cloud fraction and vertical motion (Pa/s) and right panels show the anomaly of cloud fraction and vertical motion at 4.25 km for all pressure tendency classes. The vertical motion is contoured and the cloud fields are shaded.

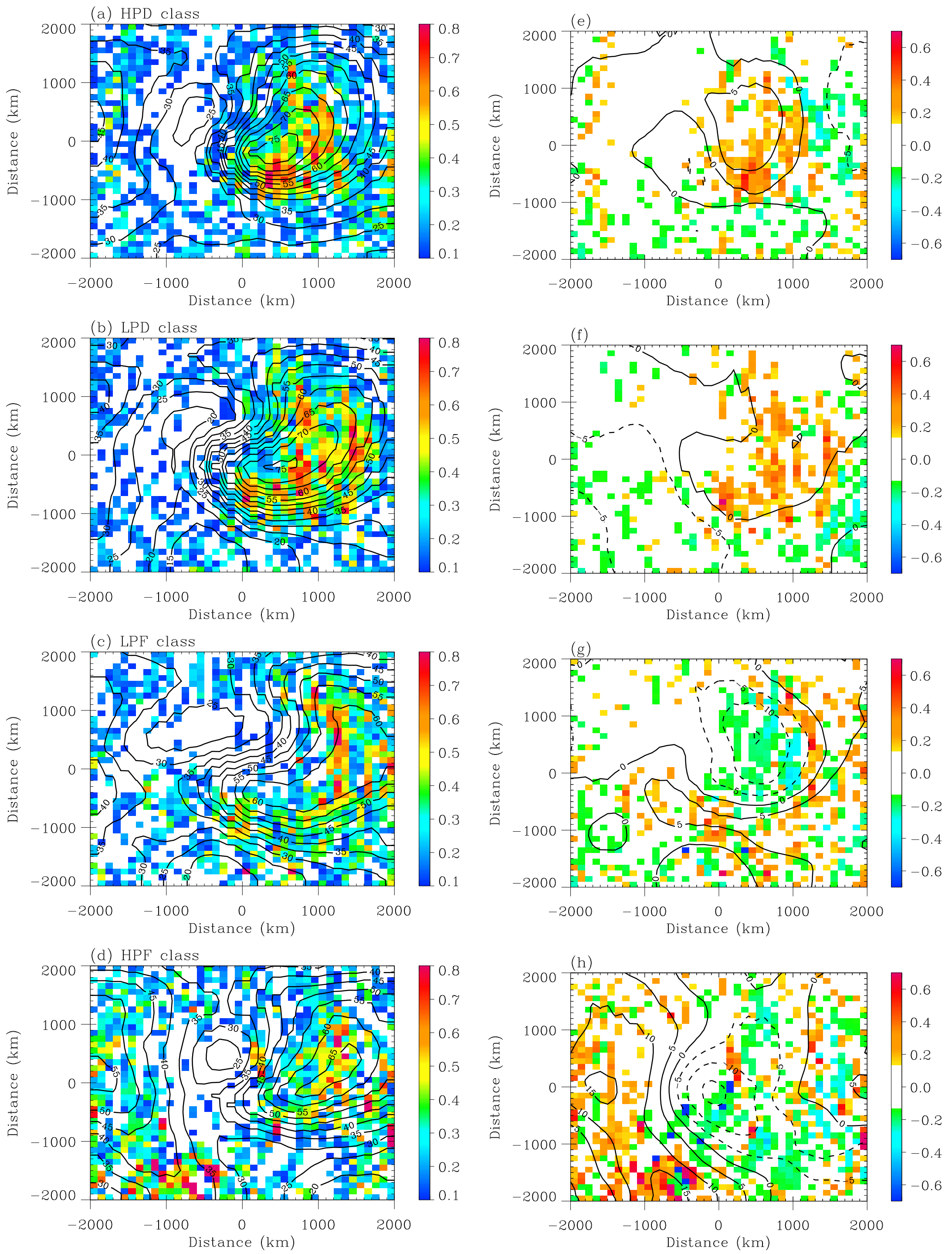

Figure 4.7: Left panels shows cloud fraction and relative humidity (%) and right panels show the anomaly at 9.25 km for cyclones in the four pressure tendency classes. The relative humidity is contoured and the cloud field is shaded.

strongest in the LPD class at the eastern side of the cyclone center. In the LPF class, the ascent weakens while the descent strengthens slightly. The ascent spreads more towards the eastern side of the cyclone center resulting in an anomalous increase of ascent to the far east of the cyclone center. In the HPF class, the region of ascent and its associated cloud structure shift towards the eastern side of the cyclone center. The descent strengthens on the western side of the cyclone center.

Figure 4.7 shows the cloud fraction and relative humidity at 9.25 km as well as their anomalies for the four classes. The maximum of cloud fraction is reached to the east of the cyclone center, similar to lower levels and consistent with ascent. The relative humidity maximum coincides with the cloud maximum, while regions with low relative humidity coincide with the cloud free regions to the west of the cyclone center, in all four stages. Values of relative humidity are higher in the deepening stages than that in the filling stages. For the HPD class, the relative humidity and cloud fraction are higher than their mean state at and near the center of cyclone. The LPD class shows an anomalous increase in the relative humidity on the eastern side of the cyclone center while the western side shows an anomalous decrease in the humidity, both consistent with the anomalous cloud fraction. The north-eastern corner of the cyclone center shows an anomalous decrease in humidity and cloud fraction in the LPF class.

As in Chapter 3, four vertical sections are selected and shown for all four classes here. Figure 4.8 shows the cloud fraction and the vertical motion at the North - South section taken 500 km east of the cyclone center, through the middle of the warm frontal region, along with their anomalies, for all classes. In the HPD class, the maximum of the cloud fraction is found at mid-levels, just to the south of the cyclone center. These clouds are more than those in the mean state. The maximum ascent coincides with the maximum of cloud fraction. Behind the warm frontal region there are no clouds consistent with descending motion in the region. In the LPD class, the maximum of cloud fraction is at the center of the cyclone. The ascending motion is larger than the mean state agreeing with anomalous increase in the clouds. In the filling stages, there is anomalous decrease in the cloud fraction consistent with anomalous weakening of the rising motion. In the warm frontal region, the deepening classes show maximum cloud fraction at mid-levels. In the filling stages, the cloud fraction decreases as the ascending motion weakens.

Clouds in the cold frontal region are shown in Figure 4.9 by taking a North -South cross-section at 100 km west of the cyclone center. In the HPD class, cloud

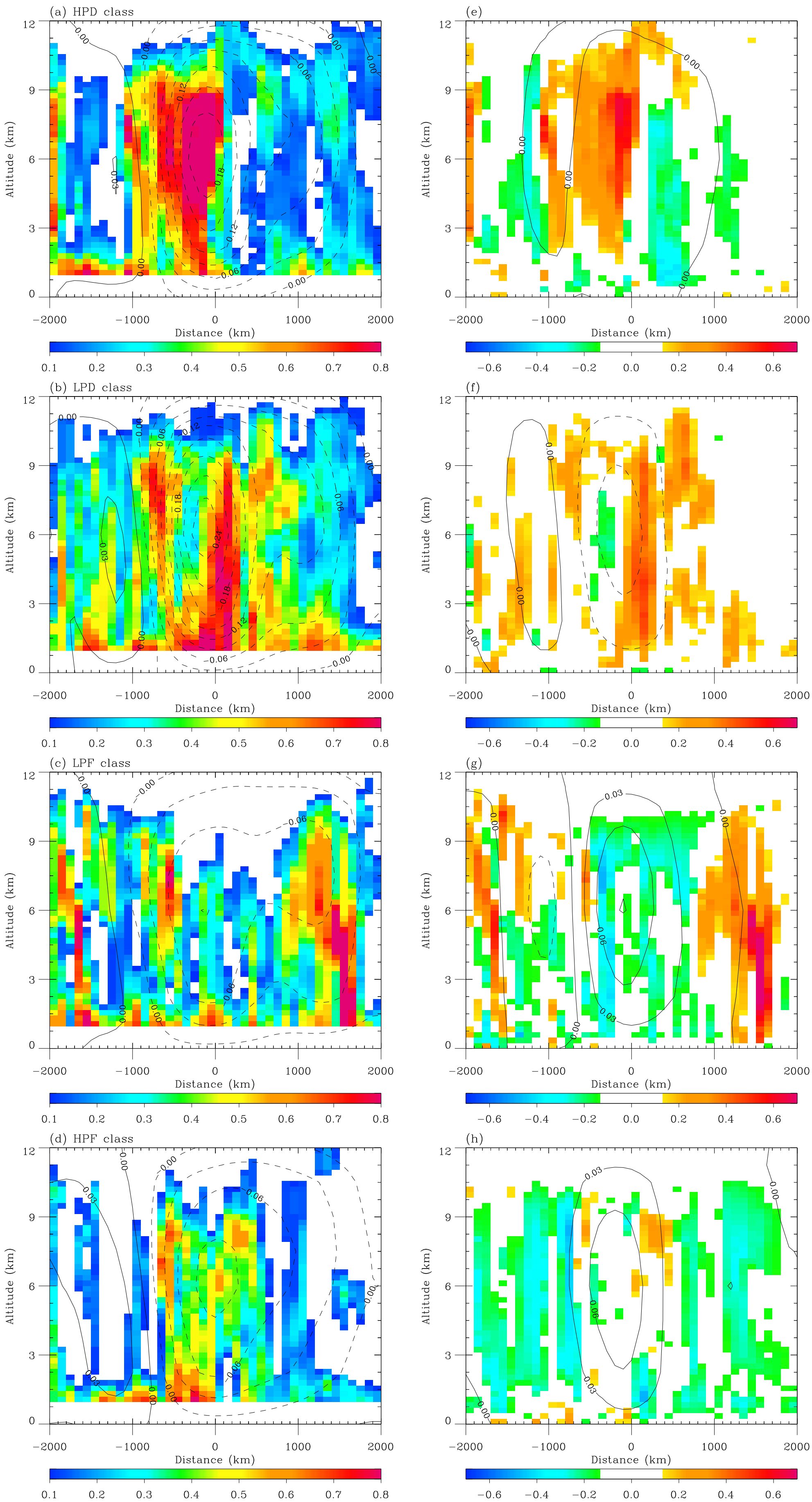

Figure 4.8: Left panels show cloud fraction and vertical motion (Pa/s) while the right panels show the anomaly of cloud fraction and vertical motion for the +500 km North-South slice for cyclones in all pressure tendency classes. The vertical motion is contoured and the cloud field is shaded.

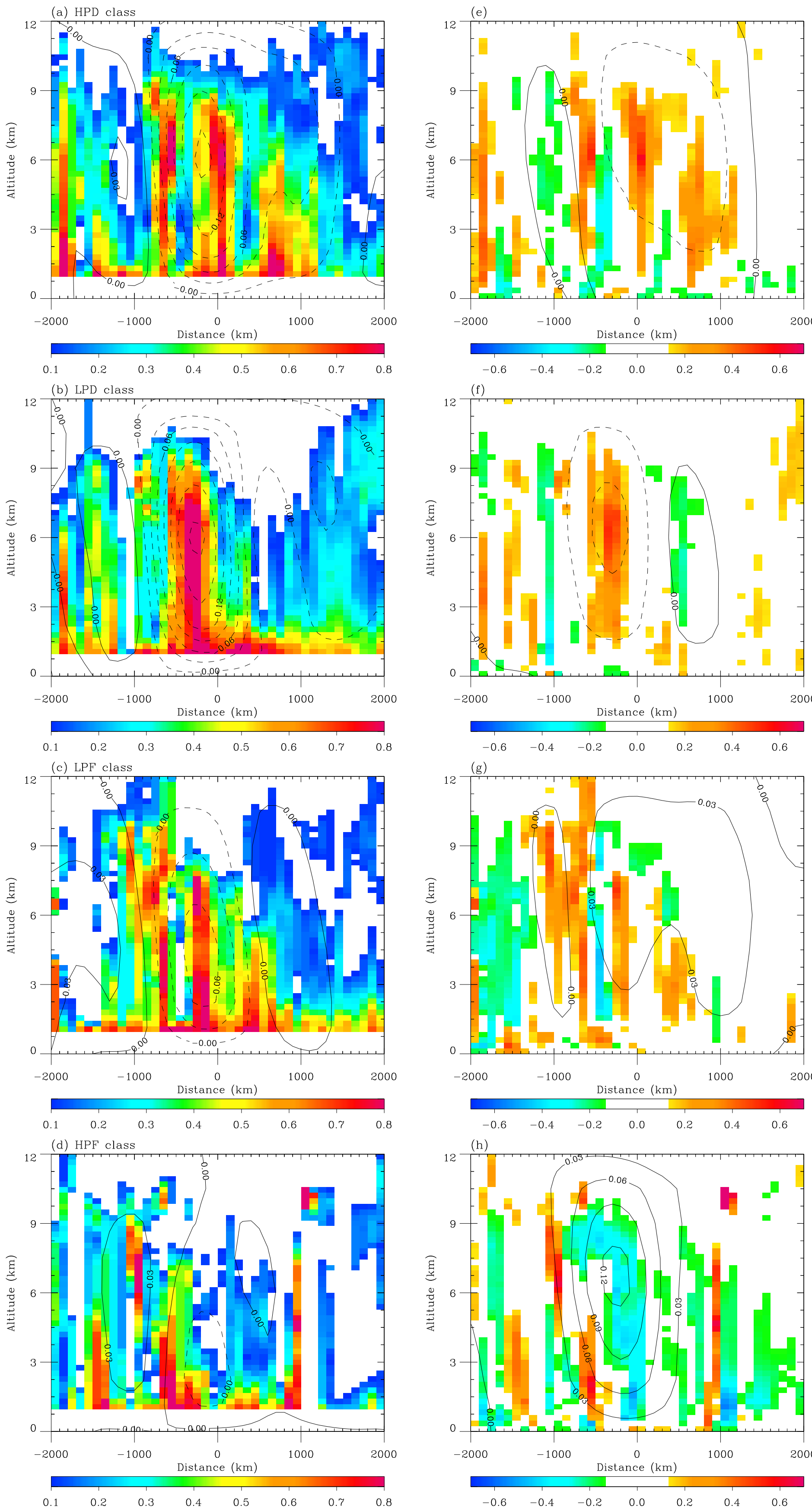

Figure 4.9: Left panels show cloud fraction and vertical motion (Pa/s) while the right panels show the anomaly of cloud fraction and ω for the -100 km North-South slice for cyclones in all pressure tendency classes. The vertical motion is contoured and the cloud field is shaded.

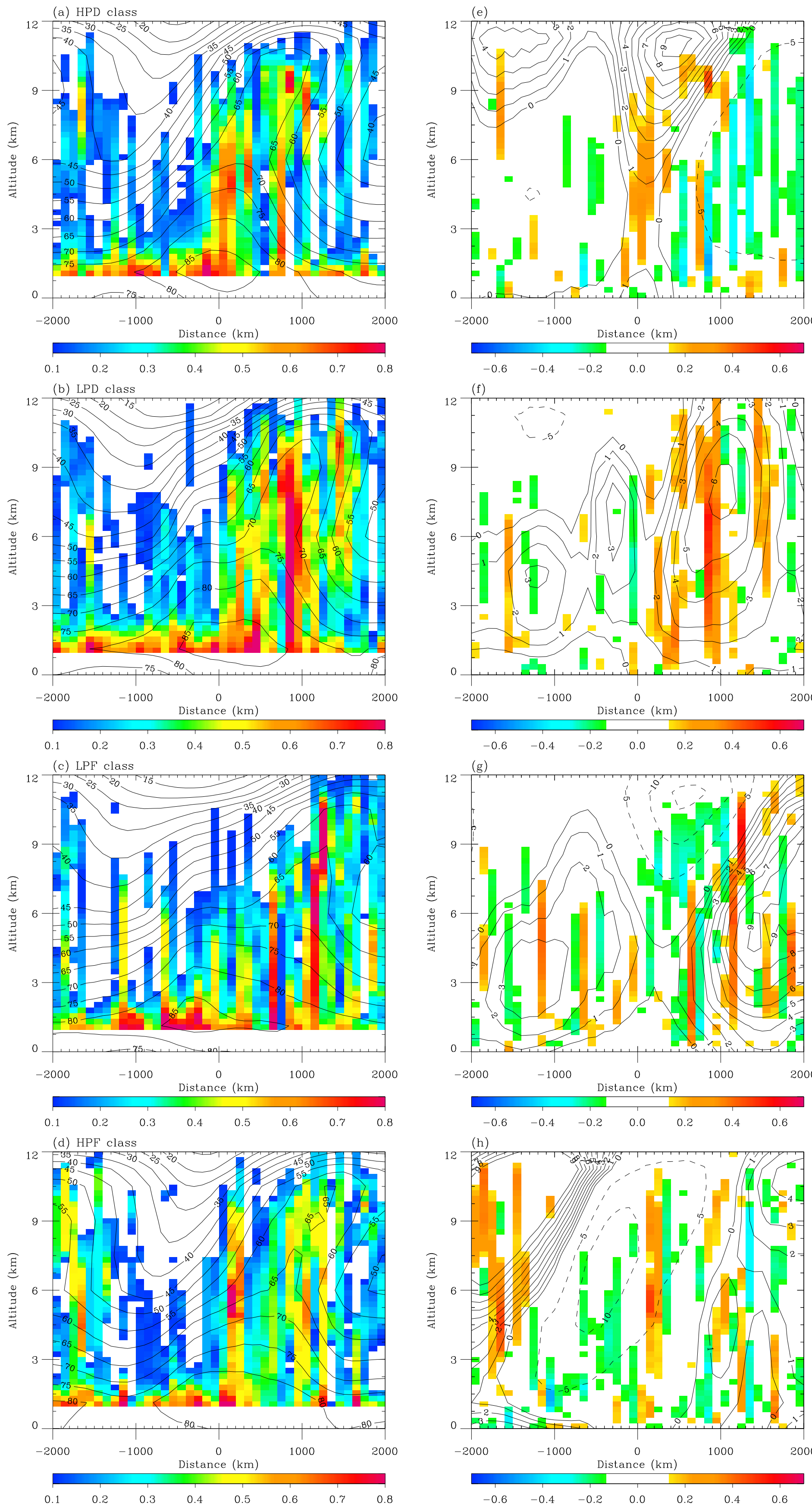

Figure 4.10: Left panels show cloud fraction and relative humidity (%) and right panels show the anomaly for the +500 km East-West slice for cyclones in all pressure tendency classes. The relative humidity is contoured and the cloud field is shaded.

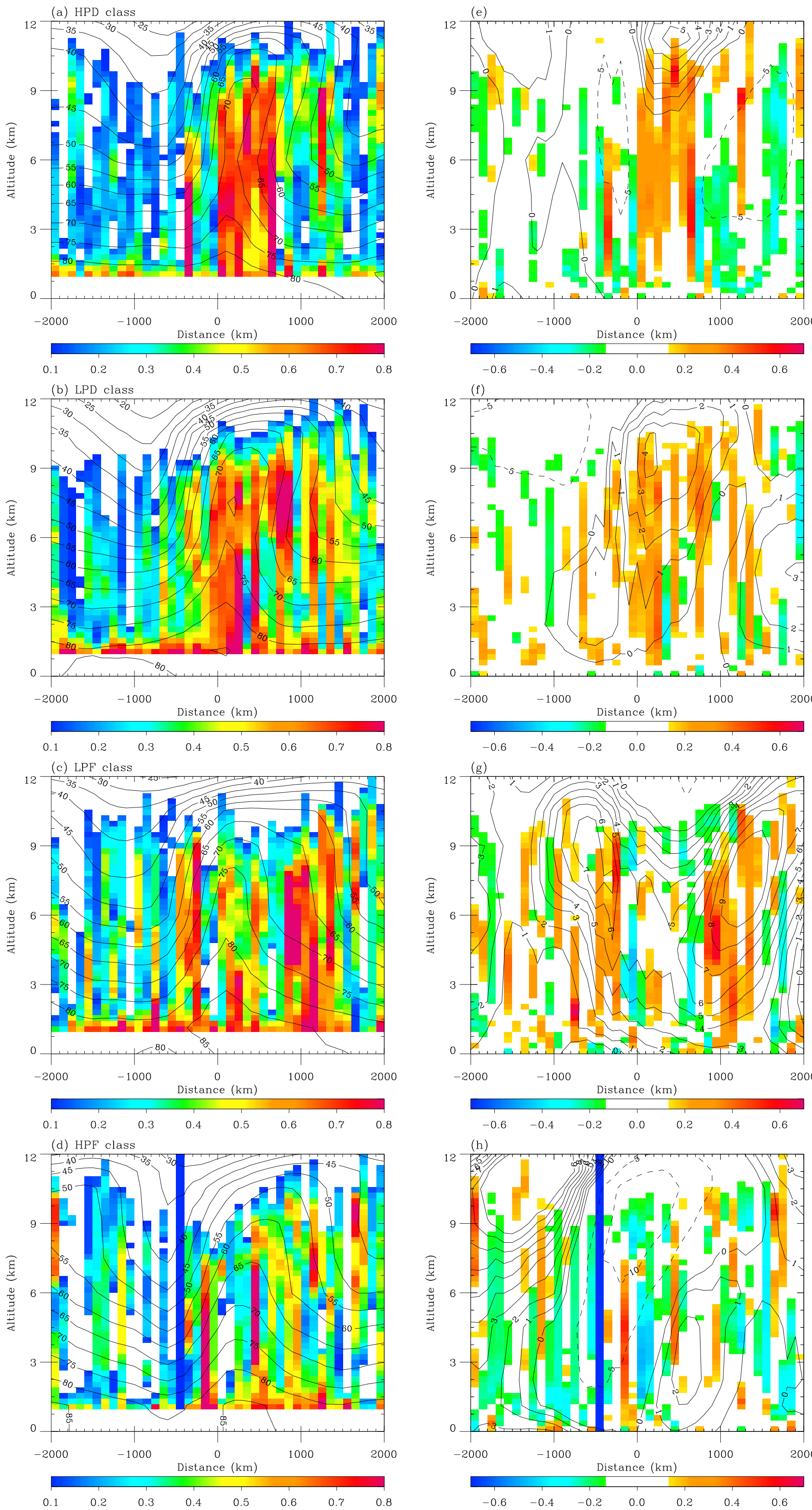

Figure 4.11: Left panels show cloud fraction and relative humidity (%) and right panels show the anomaly for the -500 km East-West slice for cyclones in all pressure tendency classes. The relative humidity is contoured and the cloud field is shaded.

fraction has two peaks, one at very low levels, around 2 km and another at a height of about 6-7 km. Values of cloud fraction and rising motion are higher than the mean state to the north of the cyclone center. The descending motion slightly strengthens and cloud fraction slightly reduces to the south of the cyclone center. The LPD class shows the highest values of cloud fraction and ascent compared to all other stages. The cloud fraction has its highest values just south of the cyclone center and it is stronger than the mean state agreeing with an anomalous increase in the ascent values in the region. However, to the north side of the cyclone center, there is an anomalous decrease in the rising motion consistent with anomalous decrease in the values of the cloud fraction. This region at 1000 km north of the cyclone center becomes the region of descent in the LPF class.

The LPF class shows an anomalous decrease of ascent and a slight increase in descent. In the HPF class, there is a strong anomalous decrease in the ascent values at and near the cyclone center and they are matched with anomalous decrease in values of cloud fraction in the region. The descending motion at 1000 km to the south of the cyclone center slightly strengthens accompanied with slight increase in the cloud fraction.

Figure 4.10 shows clouds in both the cold frontal and warm frontal region via an East -West cross-section taken 500 km north of the cyclone center. The superposed field here is relative humidity. The anomalies compared to the mean cyclone are shown in the right panels. Relative humidity and cloud fraction both show a tilted structure for all the classes consistent with the horizontal sections shown in Figures 4.5, 4.6 and 4.7. All the classes show the highest values for humidity and cloud fraction at very low levels consistent with prevalent low level cloudiness in the Southern Ocean (Haynes et al., 2011; Govekar et al., 2011). The HPD class has two maxima in the cloud fraction and relative humidity, one at very low levels, around 2 km and another at about 9 km. There is anomalous increase in the cloud and relative humidity near the cyclone center. Elsewhere there is a slight decrease in humidity and cloud fraction in this class. In the LPD class the relative humidity increases up to 70% at 6-9 km height consistent with higher cloud fraction at that height. The eastern side of the cyclone center has an anomalous increase in both relative humidity and clouds. The cloud and humidity fields at the center of the cyclone weaken in the LPF stage. However, to the far eastern side there is an anomalous increase in both fields. In the HPF class, there is an anomalous decrease in humidity at and near the cyclone center. The anomalous increase in both humidity and cloud fraction in the western part of the cyclone center confirms the likely existence of neighbouring cyclones following the original system.

An East-West slice of the cloud and humidity field taken in the region of maximum cloud fraction at mid-levels is shown in Figure 4.11 along with their anomalies. This vertical section is taken 500 km south of the cyclone center. The values of cloud fraction are maximum to the east of the cyclone center in the HPD class. The maxima of humidity and cloud fraction match well in the mid-levels. The western part of the cyclone is relatively dry and cloud free. In the LPD class, the cloud fraction on the eastern side of the cyclone center is highest compared to other classes. Both humidity and cloud fraction are higher than in the mean composite cyclone in that region. The cloud free region again lies to the western side of the cyclone center consistent with Figures 4.6 and 4.7. In the LPF class the maximum cloud fraction moves eastward and there is a slight increase in humidity and cloud fraction to the western side of the cyclone center denoting a slight weakening of the descending motion in the region. The HPF class shows larger values for cloud fraction and humidity in the western part of the cyclone compared to other classes. As seen in Figure 4.10, this is likely caused by the next system being included in the composite of this class.

The deepening classes have a cloud fraction maximum just to the east of the cyclone center while for the filling classes it moves further eastward. The rising motion is strong in the deepening stage and is accompanied with thick high top clouds. It weakens in the filling classes. This result is in agreement with Norris and Iacobellis (2005) who find that increasing the magnitude of vertical motion leads to higher cloud tops and increased optical depth.

Overall, the ascent is stronger in the deepening classes than that in the filling classes. The ascent values in the HPF class are approximately 50% less than that in the LPD class. The descending motion slightly strengthens in the filing stages. The upper level clouds having the highest humidity are in the region of ascent. For all heights, clouds in the region of descent occur in relatively drier air than those in the region of ascent. Strong ascent, higher values of relative humidity and cloud fractions are consistent with the strong rain field in the deepening classes as shown in Figure 4.4.

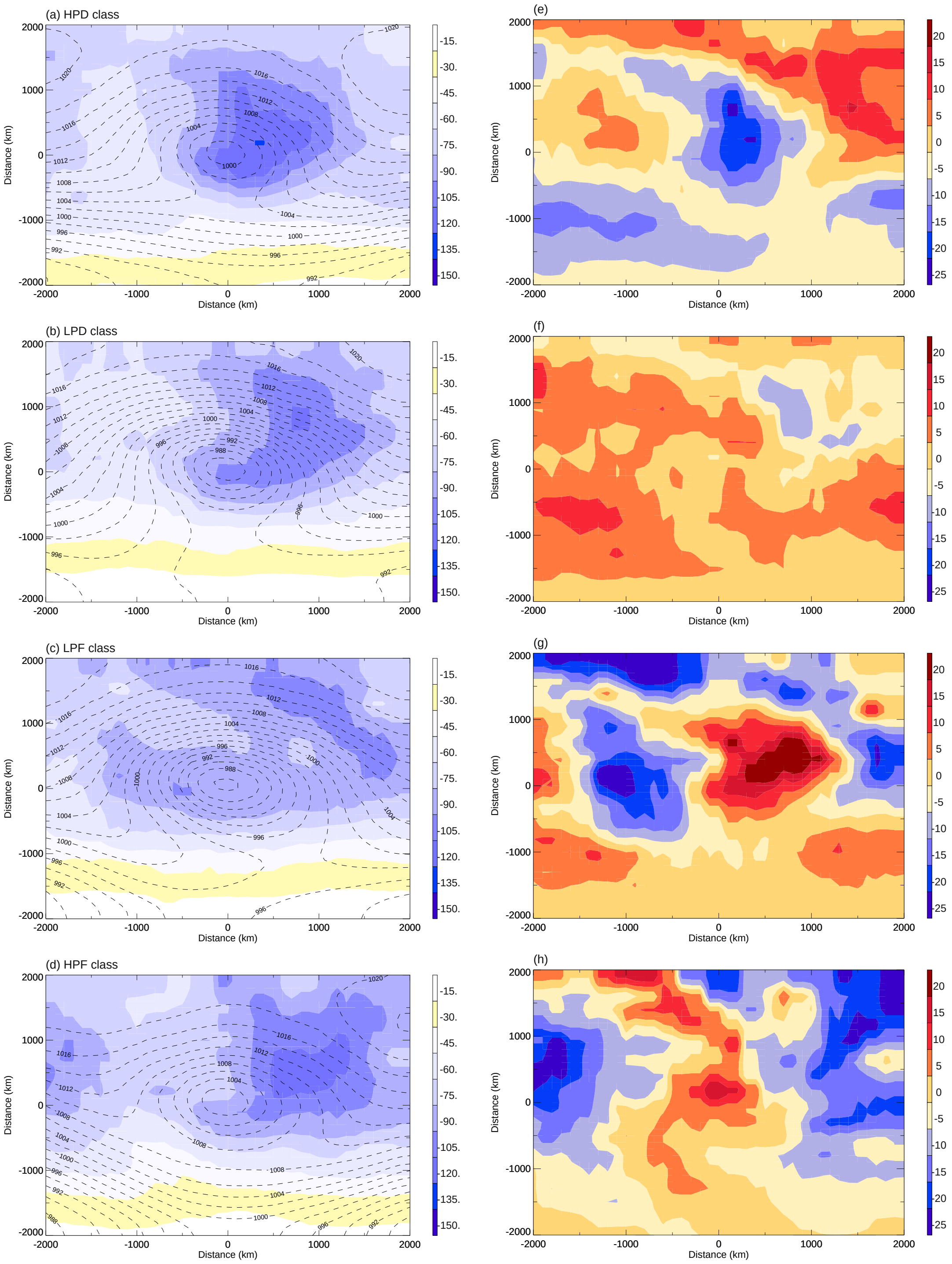

Figure 4.12: The left panels show the shortwave CRE (W/m^2) and MSLP (hPa) and the right panels show the anomaly of shortwave CRE for cyclones in the (a) HPD class, (b) LPD class (c) LPF class and (d) HPF class. MSLP is contoured and shortwave CRE is shaded.

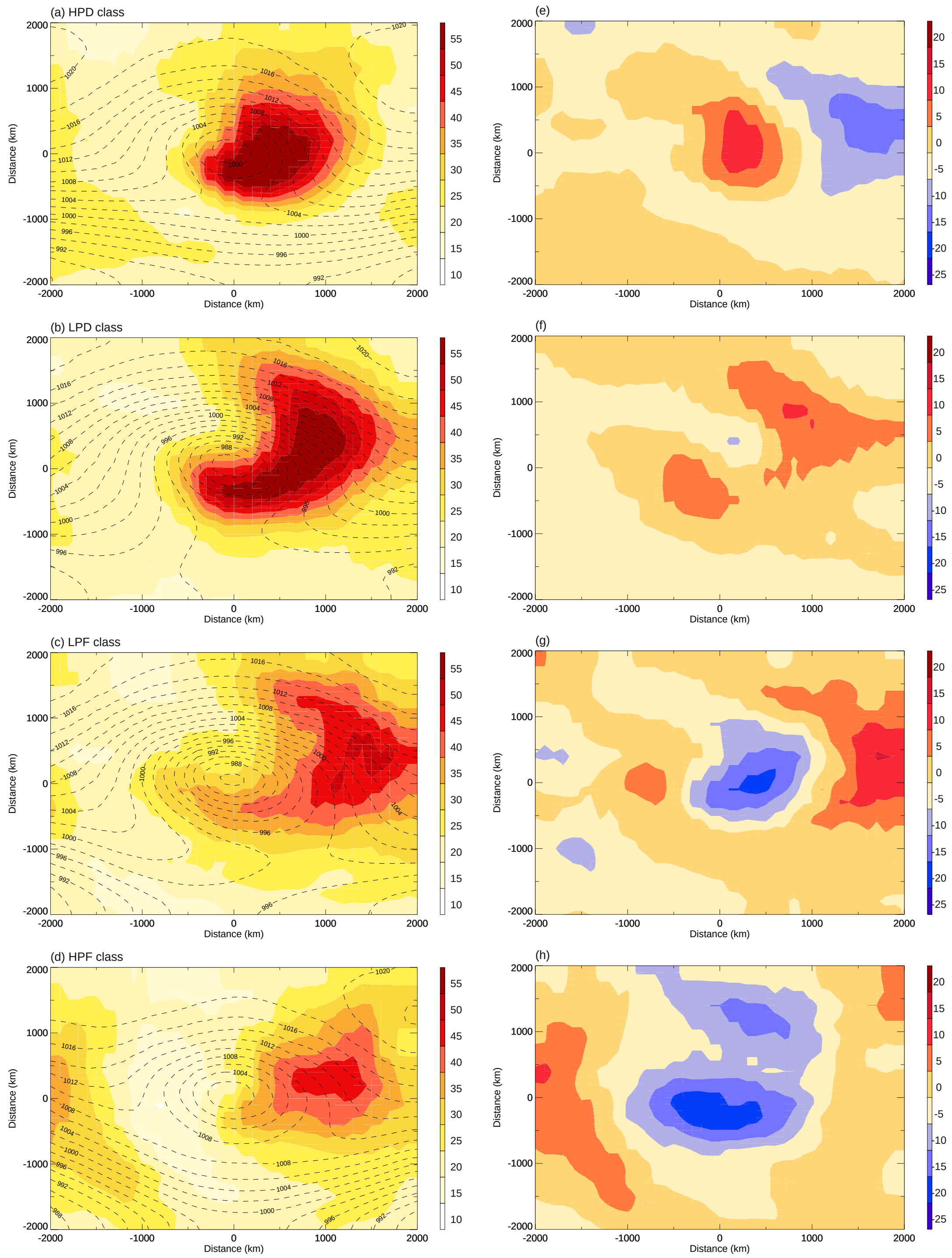

Figure 4.13: The left panels show the longwave CRE (W/m^2) and MSLP (hPa) and the right panels show the anomaly of longwave CRE for cyclones in all pressure tendency classes. MSLP is contoured and longwave CRE is shaded.

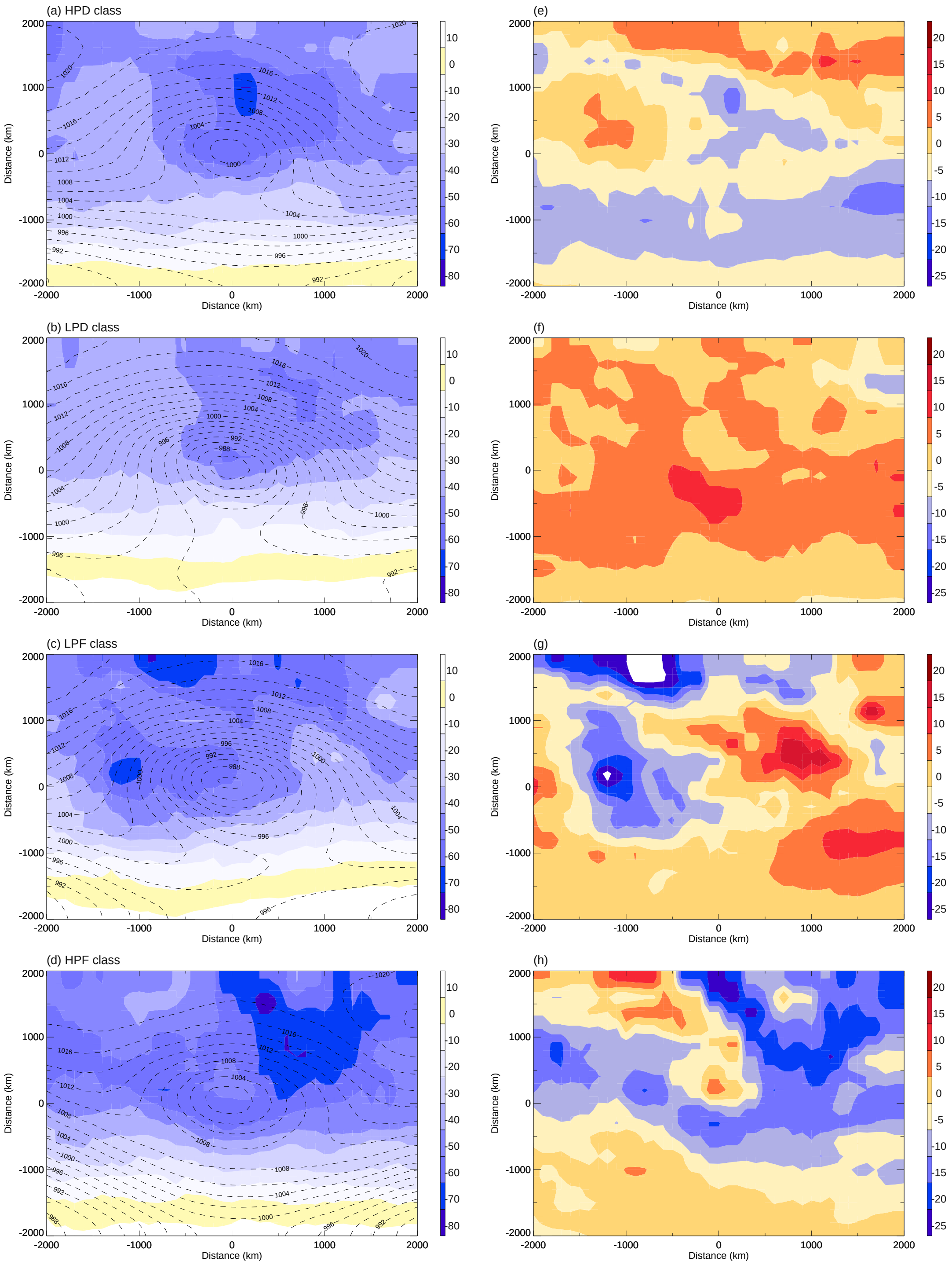

Figure 4.14: The left panels show the net CRE (W/m^2) and MSLP (hPa) and the right panels show the anomaly of net CRE for cyclones in all pressure tendency classes. MSLP is contoured and net CRE is shaded.

4.2.4 Radiation in the pressure tendency classes

Figure 4.12 shows the shortwave CRE for all pressure tendency stages. For the HPD class, there is a strong negative CRE in the shortwave of more than 70 W/m^2 to the north-east of the cyclone center. At the cyclone center shortwave CRE is more than that in the mean cyclone. At the LPD class, the shortwave CRE is more widely spread in the north-east corner. It weakens in the LPF class over all the domain and maxima of it moves more eastward consistent with shift of clouds in the region as seen in Figures 4.5, 4.6 and 4.7. However, in the HPF class, the shortwave CRE become slightly stronger at the north-eastern side of the cyclone center. The north-east corner of the cyclone shows more shortwave CRE than the mean cyclone. In the HPF class, there are the fewest high level clouds are existent (Figure 4.7). Consequently, it must be low- and mid- level clouds that produce the stronger shortwave CRE in the region. The following system to the main cyclone system is also evident in the HPF class as it was seen in the rain and cloud fields in Figures 4.4 and 4.6.

Figure 4.13 shows the longwave CRE for all stages. The longwave warming CRE is stronger in the deepening than the filling stages. In the HPD class, it is more concentrated at and to the south-east of the cyclone center. This longwave warming CRE is stronger than that of the mean cyclone. It spreads further eastward and become weaker in the LPF class. The longwave warming CRE is anomalously positive in the deepening stages in the warm frontal region consistent with thick clouds at higher levels found in that region (cf. Fig. 4.6 and Fig. 4.7). This is consistent with Tselioudis and Rossow (2006) who showed that the net longwave CRE increases with an increase in cyclone strength. The longwave warming CRE is weakest in the HPF class. It is anomalously negative near the center of the cyclone and anomalously positive in its north-eastern part showing a shift of clouds in that part of the cyclone in its later stages of life. An anomalously positive longwave warming CRE at the western side of the cyclone indicates the presence of the following systems as seen in the rain and dynamical fields.

The shortwave and longwave longwave CRE cancel each other in the warm frontal region as seen in Figure 4.14. The maximum of the net CRE is found at the north-western side of the cyclone center in the HPD class. In the LPF classes, the net CRE becomes stronger at the far northern side of the cyclone center. The net cooling is anomalously strong at the cyclone center and the southern part of the cyclone while it is anomalously weak at the western part of the cyclone in this class. In the LPD class, the net CRE is less than that in the mean cyclone. In the HPF class the net CRE is stronger in the north-eastern side of the cyclone. The maximum cooling

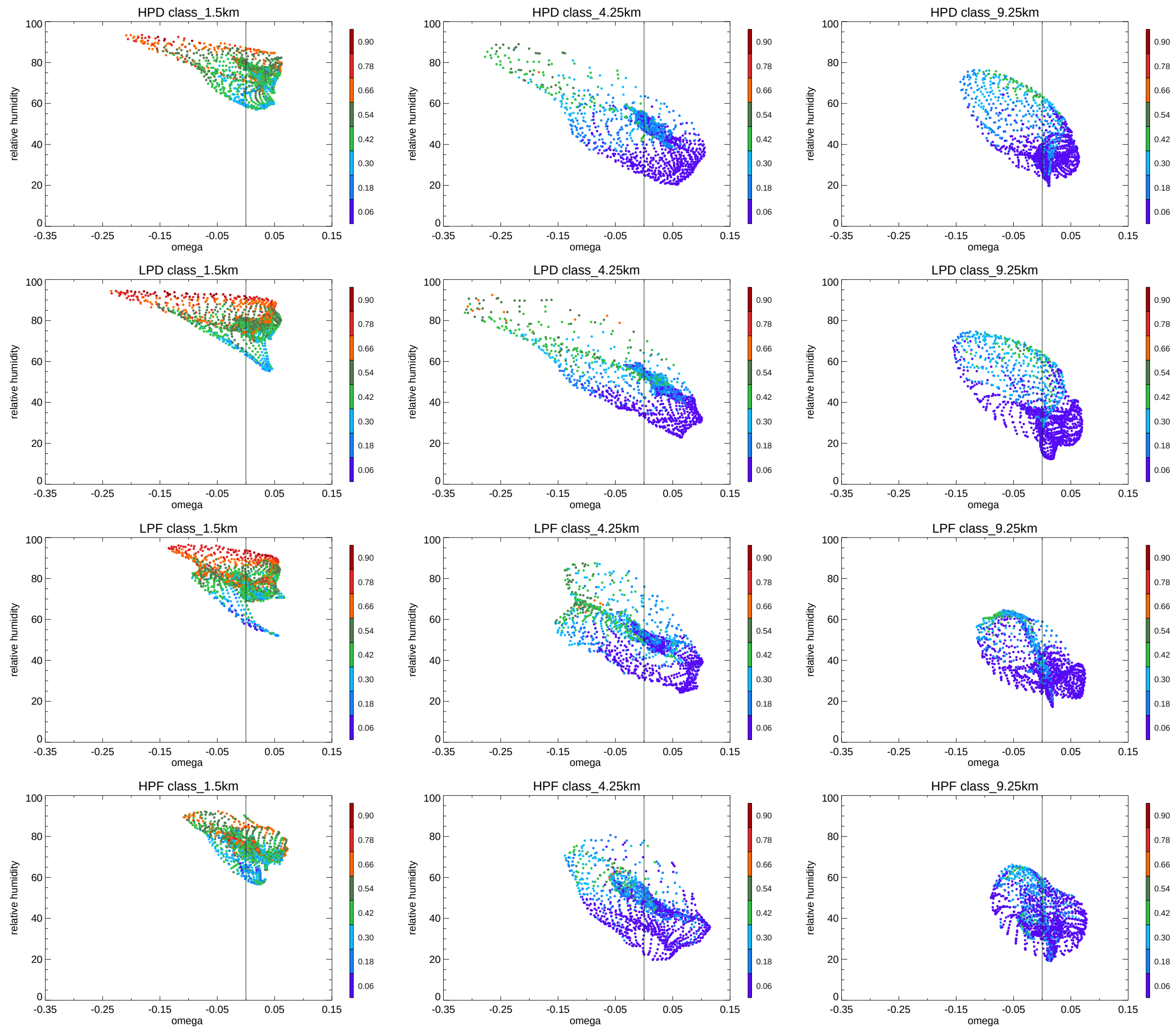

Figure 4.15: Cloud fraction in terms of relative humidity (%) and vertical motion (Pa/s) for a composite cyclone in all pressure tendency classes. The colour of the dots denote the value of cloud fraction and the black vertical line denotes the zero value of vertical motion.

net CRE is found in the HPF class. This is contradictory to Tselioudis and Rossow (2006) who showed that net CRE increases with the strength of cyclone. These type of signal do not appear in the cloud or rain field (cf. Figure 4.4 and 4.6), making it likely that it is the optical properties of the clouds that explain this result. The investigation of this issue is beyond the scope of this study.

4.3 The relationship between dynamical fields and clouds in the pressure tendency classes

One of the advantages of having vertically resolved concurrent cloud and dynamics information is that the cloud state can be more directly linked to its dynamical drivers as shown for the mean cyclone in Figures 3.14, 3.15 and 3.16. Here we apply the same technique to fields from the pressure tendency classes.

Figure 4.15 shows the relationship between vertical motion, relative humidity and cloud fraction at three different heights for all lifecycle stages. The vertical motion is on the x-axis and the relative humidity is on the y-axis. The colours indicate the value of cloud fraction. The black vertical line denotes zero values of vertical motion. This figure shows that the relationships between clouds, vertical motion and relative humidity do change with height (as shown before for the mean cyclone) but also with the class of the cyclones.

At 1.5 km, the highest cloud fraction appears in the LPD class. The values for cloud fraction are smallest in the HPF class and are consistent with minimum values of ascent. The values of cloud fraction are largest at this lowest height consistent with the prevalent low level cloudiness in the Southern Ocean. At 4.25 km, the ascent reaches its maximum value (-0.28 Pa/s) in the LPD class. The relative humidity ranges between 20% and 95%. The region of descent shows very small values of cloud fraction accompanied with the lowest values of relative humidity. In the region of ascent, the points with the highest values of ascent and the highest relative humidity are accompanied with the highest cloud fractions. The relationship between the three variables is strong in the deepening classes but it starts weakening in the filling classes. In the HPF and LPF classes, high values of cloud fraction do not necessarily relate to the high values of relative humidity implying that relative humidity and cloud fraction are not always directly proportional to each other.

Similar to the mean cyclone results in Chapter 3, at 9.25 km height, the range of all three variables is smaller than that at the lower heights for all four classes. Moreover, the relationship between the three variables is weak at this height. The region of descent is very dry and is accompanied with small values of cloud fraction. The values of relative humidity range between 20% and 70% (note again that relative humidity is defined with respect to water). Smaller values of ascent show higher values of cloud fraction than higher values of ascent indicating that vertical motion and cloud fraction are not always proportional to each other.

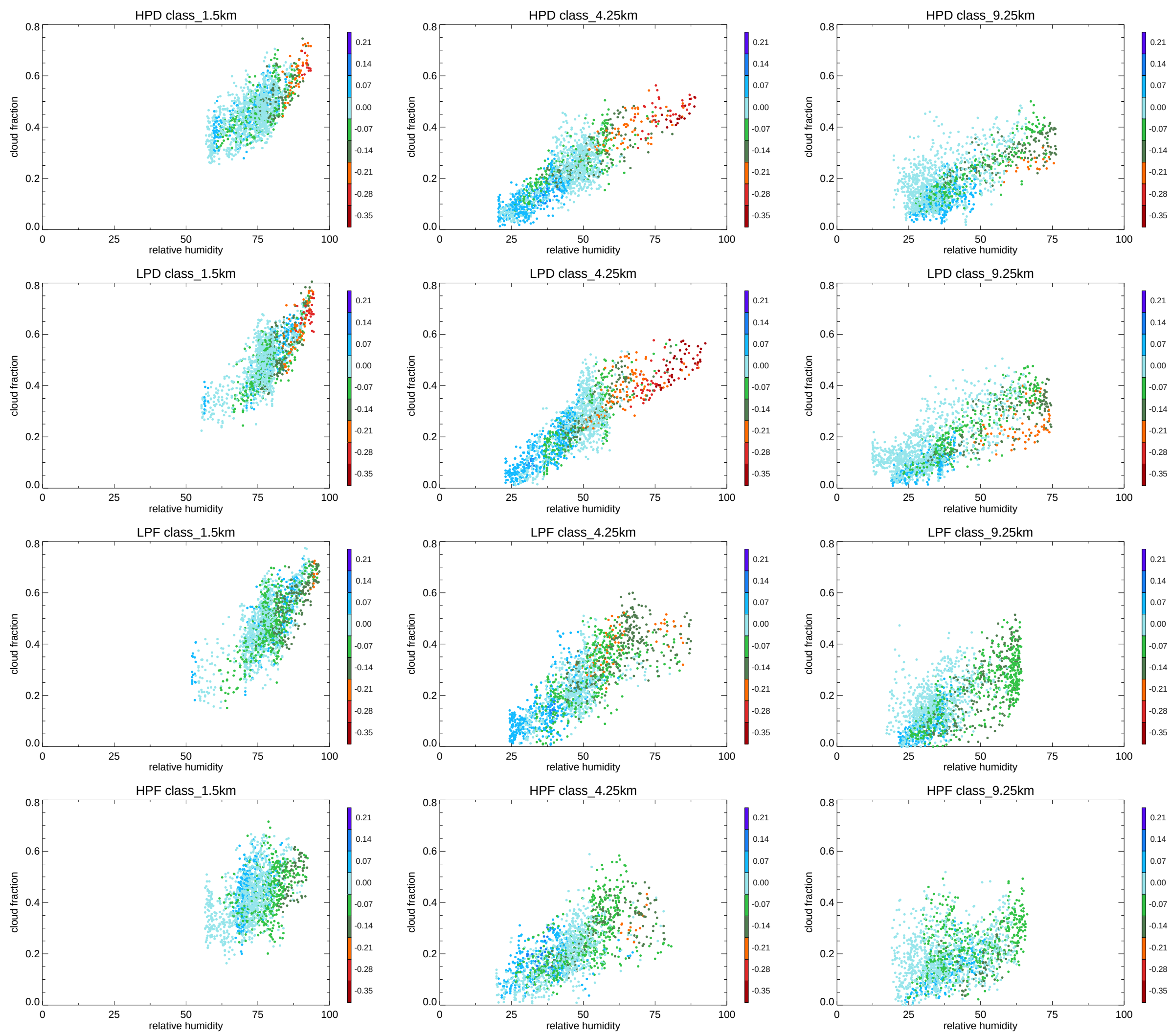

Figure 4.16: The vertical motion (Pa/s) in terms of relative humidity (%) and cloud fraction for a composite cyclone in all pressure tendency classes. The colour of the dots denote the value of vertical motion.

For all classes, vertical motion is drawn in terms of relative humidity and cloud fraction in Figure 4.16 at three different heights. The relative humidity is drawn on the x-axis and cloud fraction is on the y-Axis. The colour in this figure denotes value of vertical motion. This figure agrees well with Figure 4.15 and shows that the relationship between relative humidity and cloud fraction is nearly linear at low and mid-levels for the cyclone composite. Note that the composite provides a highly averaged picture and the results do not represent instantaneous relationships.

Cloud fraction and humidity at 1.5 km are very high. In the HPD and LPD class, the regions with higher humidity and higher cloud fraction are accompanied with higher values of ascent. Smaller values of humidity and cloud fraction are associated with small values of vertical motion. The relationship between the three variable is strong in these deepening classes. In the filling classes, the values of ascent are smaller even if the values of humidity and cloud fraction are higher.

At 4.25 km, the range of all variables is large in all classes compared to the other two heights. As shown in Figure 4.16 the values of cloud fraction and ascent are largest in the LPD class. The relationship between the three variables is strong as higher values of humidity and cloud fraction are accompanied by higher values of ascent in the deepening classes. In the filling stages, this relationship weakens. In the HPF class, the points with higher values of humidity and cloud fraction are related with smaller values of vertical motion and the regions with relatively small values of humidity and cloud fraction are related to higher values of ascent. The U-shape scatter plot for the HPF class at height 9.25 km confirms the weak relationship between the three variables in this class.

Figure 4.17 shows relative humidity in terms of vertical motion and cloud fraction, for all classes. At 1.5 km, most of the grid points show high values of relative humidity. The deepenig stages have higher values of ascent and cloud fraction compared to the filling stages. At 4.25 km, the grid points with smaller values of vertical motion and cloud fraction are relatively dry. In the LPD class, the range of all variables is bigger than in other classes. The relationship between the three variables is strong in the deepening classes but it weakens in the filling classes as shown in Figure 4.15 and Figure 4.16.

4.4 Summary

Cyclones go through a life cycle. A simple classification to represent that life cycle by considering whether the cyclone is deepening or filling is described in this Chapter. The central pressure of the individual cyclones was considered for further classification. This way, cyclones were classified into four classes. The composite method described in Chapter 3 was applied to cloud and dynamical fields related to the cyclones in these classes and comparisons were made.

The rain field evolves with the evolving lifecycle of the cyclone. Mainly, the eastern part of the cyclone is dominated by rain in all lifecycle stages. There is approximately 50% less precipitation in the filling stages than in the deepening stages.

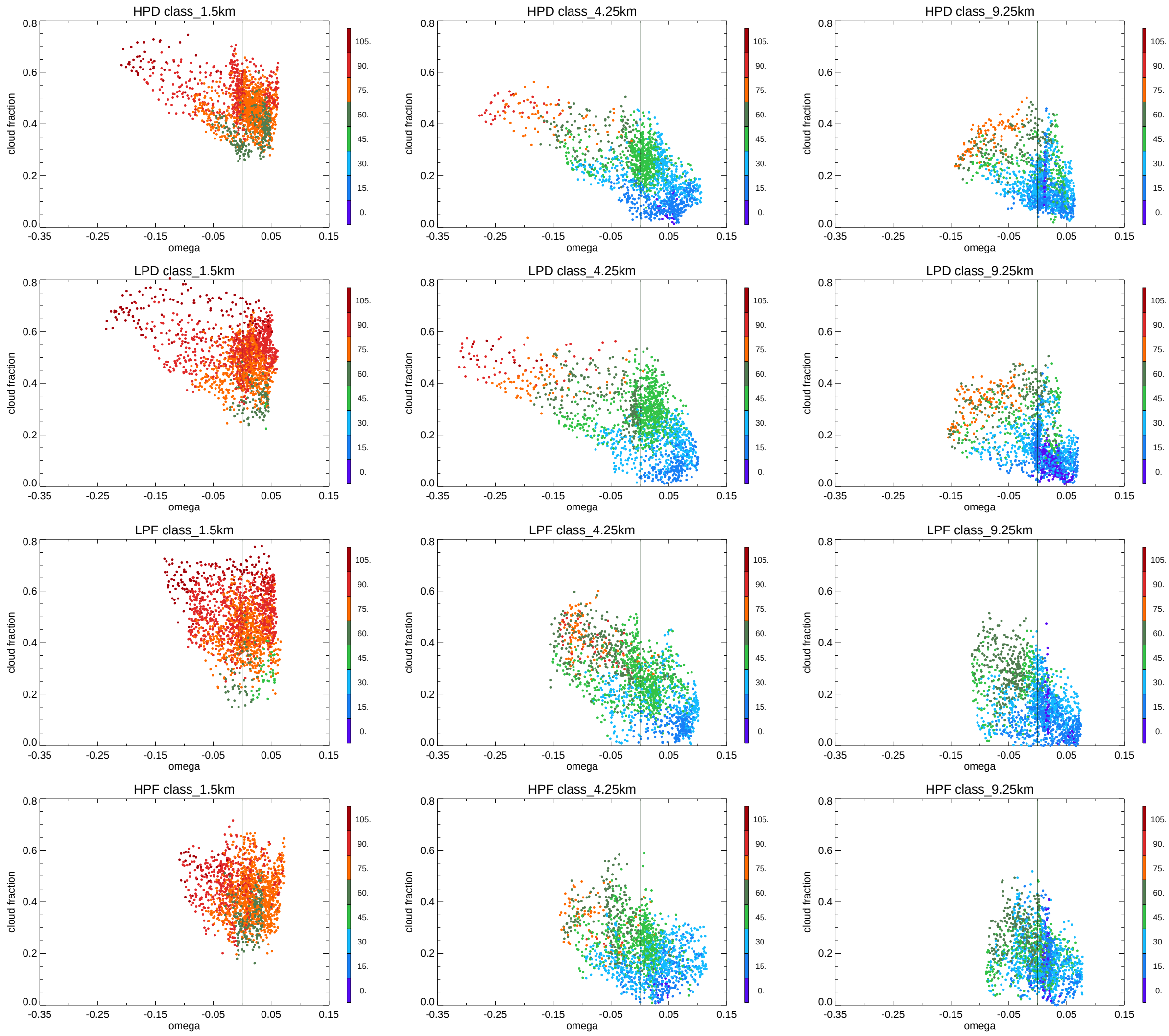

Figure 4.17: Relative humidity (%) in terms of vertical motion (Pa/s) and cloud fraction for a composite cyclone. The colour of the dots denote the value of relative humidity.

This is in agreement with analysis of Rudeva and Gulev (2011) who showed that cyclones produce less rain in the later stages of their life. The vertical motion field follows the comma shaped structure and maxima of cloud fraction are found in the region of ascent for each of the four classes. The ascent is strongest in the LPD class and the descent is strongest in the HPF class. The deepening (filling) stages have stronger (weaker) rising motion than the mean composite cyclone, consistent with larger (smaller) cloud fraction found in that region. This agrees with the results of Norris and Iacobellis (2005). The maxima of cloud fraction and rising motion shift eastward as the cyclone progresses through its life cycle. Relative humidity is matched well with the cloud field for all classes. In the deepening (filling) classes, relative humidity values are larger (smaller) than the mean composite in the eastern part of the cyclone.

The changes in the relationship between cloud, vertical motion and relative humidity with the class of cyclone is examined by drawing each variable in terms of remaining two variables for all classes. This relationship is strong in the lower part of the troposphere but weakens at higher levels for all classes consistent with the results in Chapter 3. We find that these relationships are stronger in the deepening stages and weaker in the filling classes.

Having analyzed the relationship of clouds and dynamics in a cyclone composite the next chapter will evaluate simulations of a state-of-the-art climate model using the techniques developed in this and the previous Chapters.

Chapter 5

The representation of Southern Hemisphere cyclones in a state-of-the-art climate model

5.1 Introduction

A faithful representation of midlatitude cyclones in atmospheric models is important for Numerical Weather Prediction and climate science. To have confidence in predictions of changes to extratropical cyclones in a future climate, climate models should provide a realistic representation of these systems, from the spatial distribution of the storm tracks down to the structure of the storm. Extratropical cyclones can also be associated with severe weather in terms of heavy rain and damaging winds. For these reasons it is important to determine if extratropical cyclones, including their description of clouds and their relationship to dynamical processes are adequately represented in weather and climate models. The analysis presented in the previous Chapters provides an innovative framework for the evaluation of cyclone structures in models.

Many recent studies have examined the representation of aspect of cloudiness as well as the radiation budget in climate models (Bodas-Salcedo et al., 2012; Field et al., 2011). These studies show that current models have large biases in the radiation budget. Webb et al. (2001) and Williams and Webb (2009) show that a deficit of bright mid-level cloud in the mid-lattude oceans contribute to a weak shortwave cloud radiative effect (CRE). Trenberth and Fasullo (2010) analyzed 24 coupled models from the Third Coupled Model Intercomparison Project (CMIP3, Meehl et al. (2007)) and demonstrated that models show a consistent positive bias in the absorbed shortwave radiation at top of atmosphere (TOA) over the Southern Ocean region. They argued that a lack of clouds in the present-day climate simulations is at least partially responsible for these TOA shortwave biases in the region. As the Southern Ocean covers a large area, the errors in the cloud representation in the area will have a relatively large effect on the global TOA radiation budget. If the model poorly reproduces the cloud distributions, then it is unlikely that it will reproduce cloud-climate feedbacks correctly (Webb et al., 2001).

This chapter aims to evaluate the Australian Community Climate and Earth System Simulator (ACCESS) model against observations. The main characteristics of Southern Hemisphere extratropical cyclones are examined by compositing data related to cyclones in a reference framework where the origin is at the center of the cyclone, as described in the compositing method in Chapter 3. This compositing approach is a useful way of removing cyclone-to cyclone variability from both observations and model cyclones (Lau and Crane, 1997; Klein and Jakob, 1999; Field et al., 2008, 2011). An assessment of cloud and dynamical fields along with precipitation and the radiation budget related to Southern Hemisphere extratropical cyclones will be carried out by applying this compositing method to the ACCESS model. We first compare the model simulation with ISCCP observations and then assess three-dimensional cloud structure of extratropical cyclones captured by models with CloudSat/CALIPSO observations. The relationship between clouds and dynamical fields related to extratropical cyclones in the model is examined and compared with that in the observations. As was done for the observations in Chapter 4, the model cyclones are then classified into four classes and the changes in the relationship between clouds and dynamical fields produced by the model are assessed against the observations.

5.2 Description of the model simulation

The ACCESS model used in this study is the MetUM version 7.1 and is based on the second version of the Hadley center Global Environment Model (HADGEM2-A) described in Collins et al. (2008). The model has been run for 2 years (2000- 2001). We run the ACCESS in atmosphere only mode forced with climatological SSTs. The analysis presented in this chapter is carried out with the climate horizontal resolution N96 (1.875^0 longitude $\times$ 1.25^0 latitude) and with 38 vertical levels. The model output used are 6 hourly bulk cloud fraction, vertical velocity, relative humidity, sea level pressure, radiation fluxes, as well as the large scale and convective rain fields.

The cloud scheme used in the simulation was the PC2 (prognostic cloud, prognostic condensate). The scheme uses a prognostic representation of cloud fraction and condensate by estimating their increments from each physical and dynamical process that is represented in the MetUM (Martin et al., 2011; Franklin et al., 2012). Changes have also been applied to the parameterization of convection when using the PC2 cloud scheme (Wilson et al., 2008). The major changes include an increase in the proportion of condensate that is detrained from the convective plumes, rather than being precipitated and a reduction of the phase change temperature between liquid and ice condensate in the convective updrafts. These changes have been found to be necessary to produce realistic anvil clouds due to the direct interaction of the large-scale cloud variables in PC2 with the convection scheme. The PC2 scheme includes prognostic variables for the cloud liquid water content, the cloud ice water content, the bulk cloud fraction, the liquid cloud fraction and the ice cloud fraction. The bulk cloud fraction, which is the volume of a grid-box covered by cloudy air in the PC2 scheme, was used here to compare with cloud observations from CloudSat/CALIPSO. Model rainrates were derived by adding precipitation from the large scale rain and convective parameterization schemes. Model fields for vertical motion, relative humidity, MSLP were extracted.

5.3 Evaluating the cyclone cloud structure using ISCCP observations

Several studies have evaluated climate models using ISCCP observations (Zhang et al., 2005; Field et al., 2011; Bodas-Salcedo et al., 2012). The main goal of this section is to compare earlier work with our analysis and make sure that the compositing technique used here is working well.

The ACCESS model has been run for the year 2000 using model version 7.1 including the ISCCP simulator (Klein and Jakob, 1999; Webb et al., 2001). The ISCCP simulator minimizes the difference of sampling geometry between the models and observed data. As a GCM represents clouds on a much coarser grid than the satellite observations, the ISCCP simulator downscales the model output to better match with satellite observations. Also, it allows the comparison of model clouds with measurements that matched cloud top pressure and visible optical depth with observations.

The model data is available 6 -hourly on a $1.88^0 \times 1.25^0$ grid and 38 vertical levels. Model fields for MSLP and cloud fraction in the standard ISCCP cloud-top pressure and cloud optical depth bins, were extracted. The cyclones were tracked using a method similar to Bauer and DelGenio (2006) applied to the MSLP field of the model. Using the compositing method described in Chapter 3, model fields for MSLP and cloud fraction as a function of ISCCP cloud top pressure were composited and are shown in Figure 5.1.

The left panels of Figure 5.1 show composited cloud fraction and MSLP from the model for the seven different cloud top pressure classes. The right panels show the difference of cloud fraction between the model (using the ISCCP simulator) and the ISCCP observations. The center of the cyclone can be easily seen in the MSLP field with approximately 990hPa minimum pressure. The MSLP field shows a structure consistent with the observations (cf. Figure 3.3). The model shows a larger horizontal extent of the cloud field compared to the observations. Consistent with the observations, low level clouds are at the west side of the cyclone center while upper level clouds are at the east side of the cyclone center. Mid-level clouds are found mainly on the southern side of the cyclone center. The main difference between the observations and the model is a lack of clouds below 500 hPa in the model. This underprediction of mid-level and low level clouds in the model is consistent with the result of Field et al. (2011) who used the Met Office Unified Model (UM) to assess clouds in midlatitude cyclones.

The compositing in the model worked well and reproduced existing results, which gives us confidence for the use of the CloudSat/CALIPSO data below.

5.4 Evaluation of the composite cyclone radiation and precipitation structure

Figure 5.2 shows the model-simulated CRE and precipitation as well as their difference from observations. The observed radiative fluxes are based on the ISCCP-FD data (as shown in Figure 3.4) and the observed precipitation field is from the GPCP dat set (as shown in Figure 3.4 (d)). As described in Chapter 3, the CRE is the difference between clear sky and full sky radiative fluxes. Panel (a) shows the shortwave CRE from the model (left) and panel (e) shows the model error which is calculated by subtracting the observed shortwave CRE from the model values. There is a negative (cooling) CRE in the shortwave of more than 20 W/m^2 in the model in the

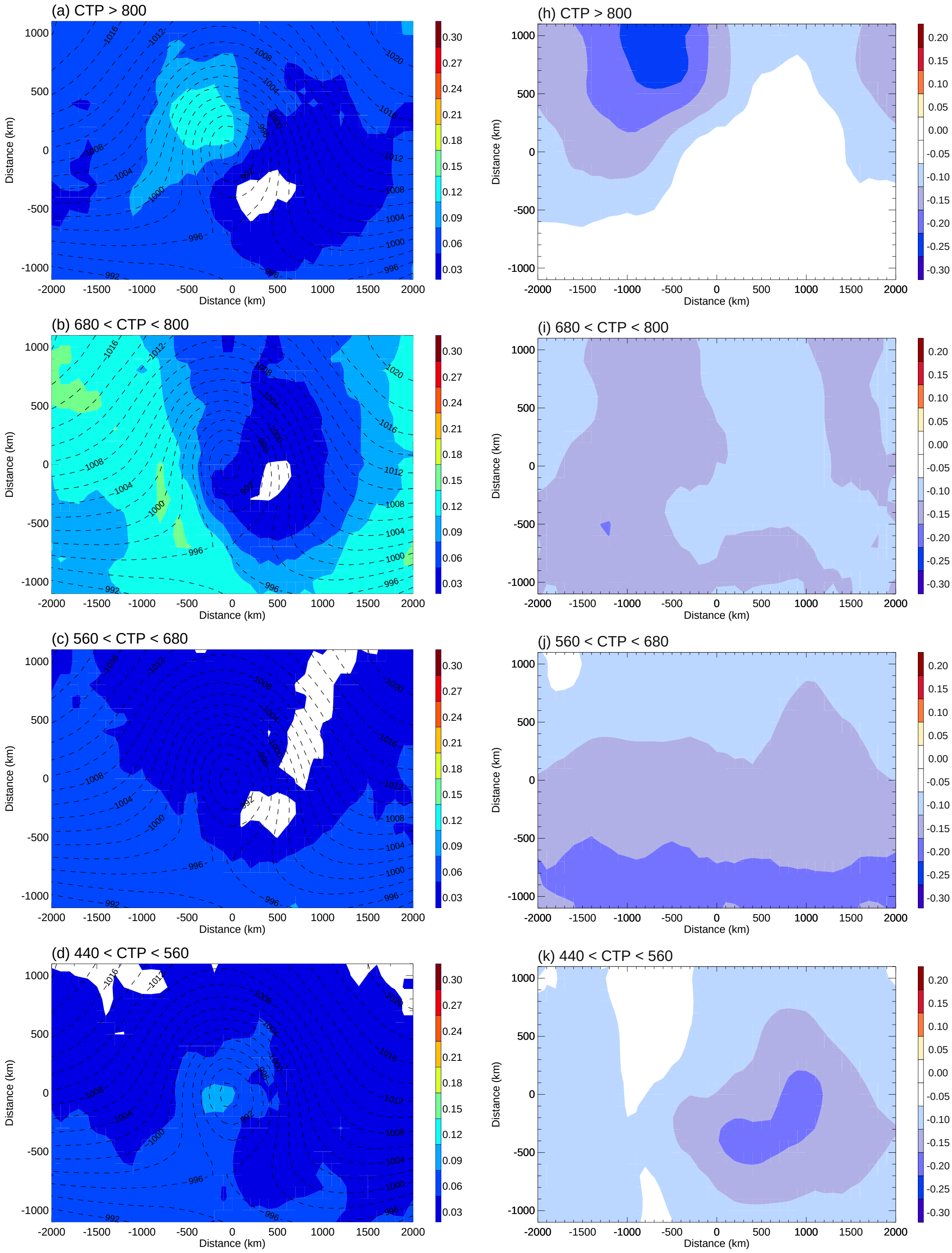

Figure continued on the next page.

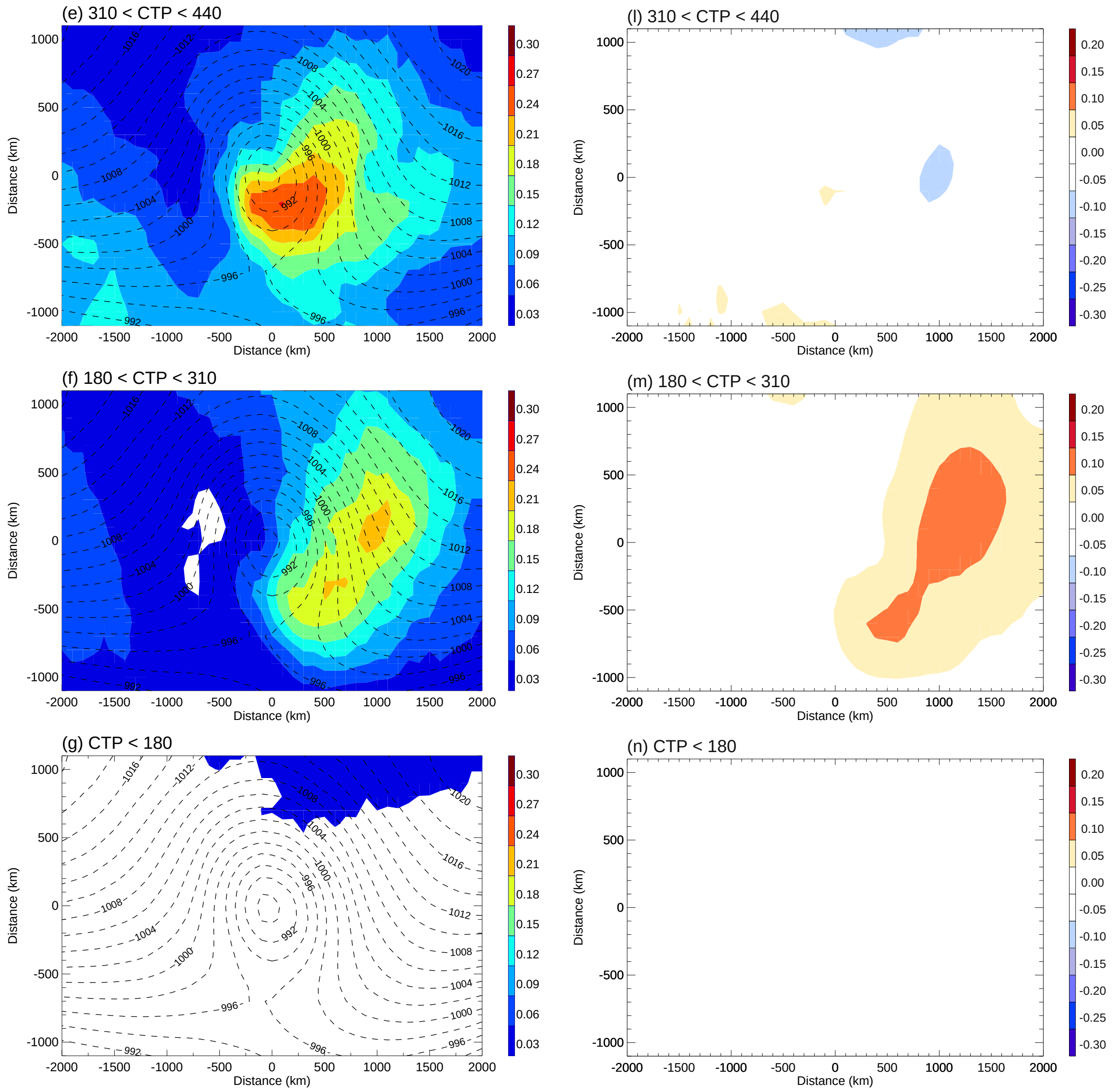

Figure 5.1: MSLP (hPa) and cloud fraction for the seven ISCCP CTP classes. The first column shows total cloud fraction and MSLP from the model simulation, the second column shows the model error. MSLP is contoured and the cloud fields are shaded.

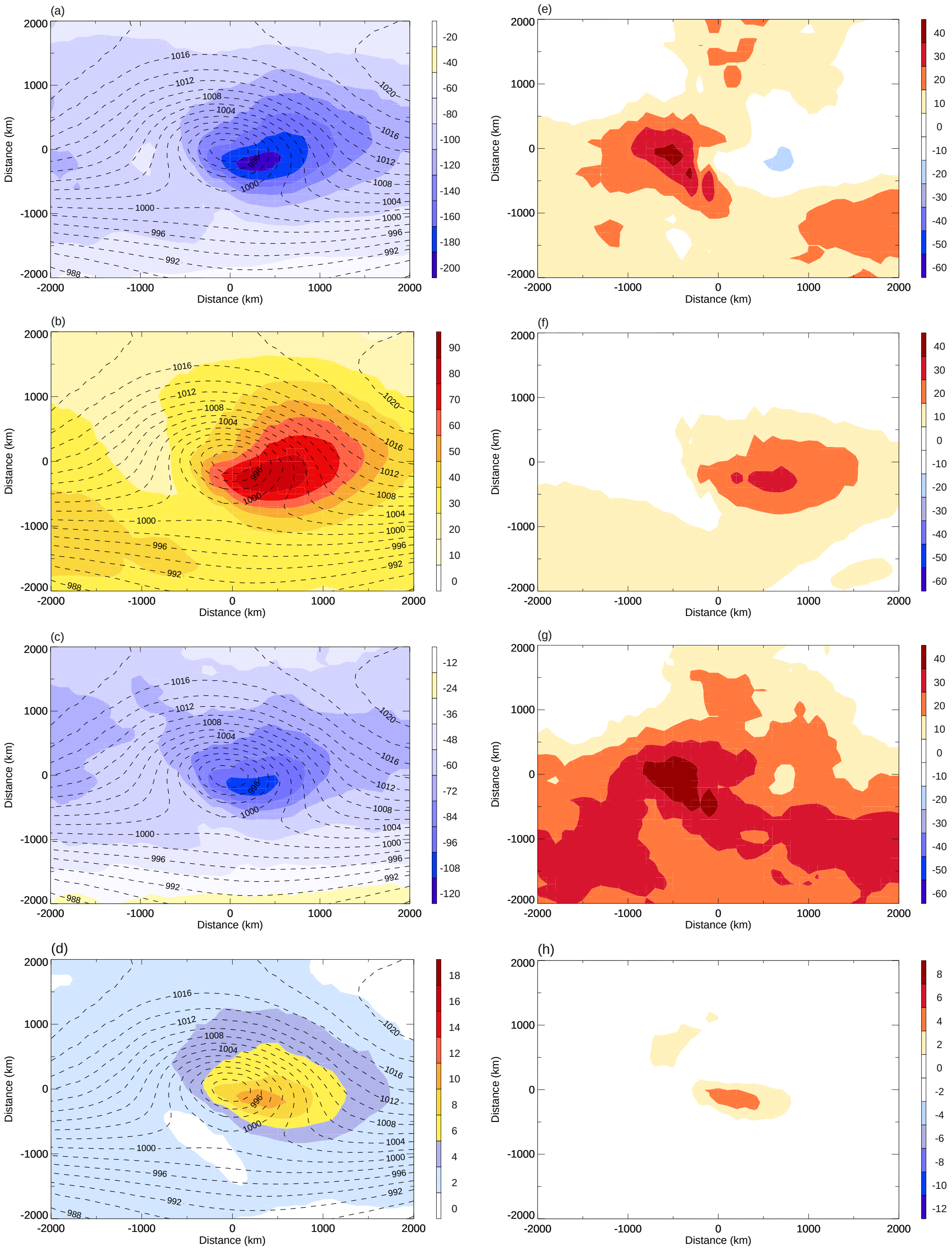

Figure 5.2: Cyclone composite CRE, MSLP (hPa) and precipitation from the model and the model error. MSLP is contoured, the radiation and precipitation fields are shaded. Panels (a) and (e): Shortwave CRE (W/m^2). Panels (b) and (f): Longwave CRE (W/m^2). Panels (c) and (g): Net CRE (W/m^2). Panels (d) and (h): Precipitation (mm/day).

entire domain. The maximum of the shortwave CRE lies near the center of cyclone in the warm frontal region. To the western side of the cyclone center the model fails to produce a strong enough shortwave CRE, compared to the observations. This is consistent with Field et al. (2011) who showed that for the short-wave, the model is brighter near the cyclone center and is dimmer away from the center, compared to the ISCCP - FD data set. There is bias of more than 40 W/m^2 behind the composite model cyclone center. The lack of clouds at mid - and lower levels seen in Figure 5.3 very likely contributes to this large bias. This result is consistent with Bodas-Salcedo et al. (2012) who composited the shortwave CRE around cyclones and showed that there is large shortwave CRE bias in the cold air region.

Panel (b) of Figure 5.2 shows the positive (warming) longwave CRE in the model around the composite model cyclone. The longwave CRE is peaking at up to 80 W/m^2 in the model. As described in the Chapter 3, the longwave CRE is generally driven by high level clouds. Consistent with overestimation of high clouds, the model has a stronger longwave CRE than observed (Figure 5.2(f)). The region of strong longwave CRE is slightly misplaced ahead of the observed warm frontal region.

The net CRE is the sum of the shortwave CRE and the longwave CRE and is shown in Panel (c) of Figure 5.2. The net CRE is negative all over the cyclone area box. Panel (g) shows its difference from the observations. The model has up to 40 W/m^2 of bias in the western part of the composite model cyclone. Consistent with conclusions of earlier studies (Trenberth and Fasullo, 2010; Field et al., 2011; Bodas-Salcedo et al., 2012) this bias in the net CRE is largly driven by a bias in the shortwave CRE and highlights once again the lack of low level clouds behind the cyclone center in the model.

Panel (d) shows the precipitation distribution around the model cyclone center. The maximum precipitation is found to the east and south-east of the cyclone center with values of 8-10 mm/day. Panel (h) shows the model error calculated by subtracting the GPCP derived precipitation composite from that of the model. The model produces more rain than the observations in the south-eastern part of the cyclone, consistent with over-prediction of high level clouds in the model in that region.

5.5 A precipitation adjusted CloudSat/CALIPSO data set for model evaluation

Our goal is to compare model simulations to the three-dimensional cloud and dynamical cyclone structure investigated in Chapters 3 and 4. To do so requires to match the model output with appropriate observations. There are two ways of doing this, i) the use of an observation simulator and ii) to retrieve the relevant model quantities from the observations. The Cloud Feedback model Comparison Project (CFMIP) Observation Simulator Package (COSP, Bodas-Salcedo et al. (2011)) is a software tool that allows simulation of Cloudsat data in the ACCESS that is consistent with the model microphysics (Field et al., 2011; Bodas-Salcedo et al., 2012). Unfortunately the COSP was not available to us at the start of this study. Hence we need to find ways to match CloudSat/CALIPSO data with model data as best as posiible. There are several issues to consider. first, the model height levels are not equally distributed and don't match the CloudSat/CALIPSO levels. They are denser at lower levels than at higher levels. To better match the observations, CloudSat-CALIPSO observations were averaged to match the model levels. At 1.6 km, the model output is compared with the average of two CloudSat vertical levels, at $\approx$ 1.7 km and $\approx$ 1.4 km. At 4.5 km, the model is compared with an average of three Cloudsat levels, at $\approx$ 4.5 km, $\approx$4.3 km and $\approx$4.1 km. At 9.7 km, the model output is compared with the average of four CloudSat levels, at $\approx$ 9.6 km, $\approx$9.3 km, $\approx$9.1 km and $\approx$8.9 km. Figure 5.3 shows this averaged cloud fraction at those three different heights in the left panels. Comparison to Figure 3.8 reveals that the main cloud structures are preserved in the averaging.

A second issue for the comparison is that the CloudSat/CALIPSO dataset includes precipitation in the cloud mask (Haynes et al., 2009), and consequently the estimated cloud fractions include a contribution from precipitation and are likely overestimated. We construct a new cloud mask (noprecip) by removing all cloud profiles for which precipitation was detected at the ground (Jiang et al., 2012). The precipitation flags (rain, snow, drizzle and graupel) in the CloudSat 2C-PRECIP-COLUMN product (Haynes et al., 2009) was used to detect precipitation at the ground. We consider the range between the original and noprecip cloud masks as a reasonable estimate of the upper and lower bound of cloud fraction from the CloudSat/CALIPSO data set. Both sets of observations are used from hereon for the model evaluation.

The upper bound of the cloud observations are shown in the left panels and the

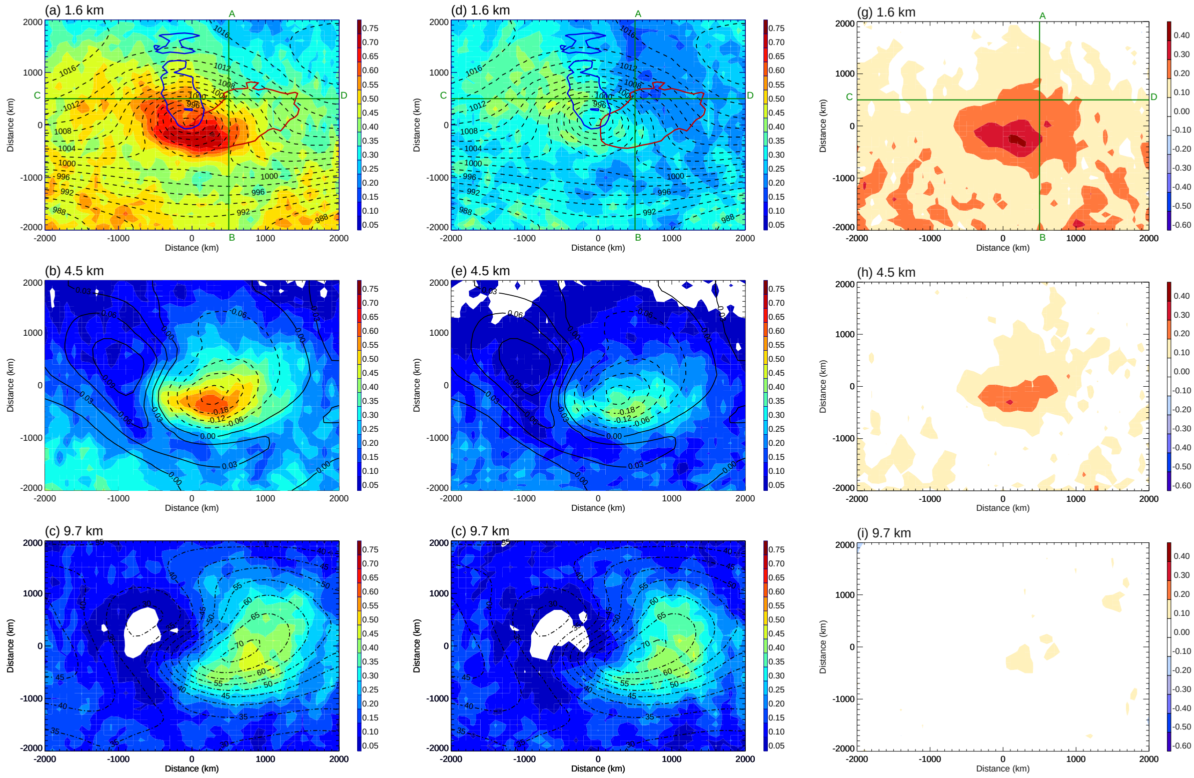

Figure 5.3: Cloud fraction at height 1.6 km (panels (a), (d) and (g)), 4.5 km (panels (b), (e) and (h)) and 9.7 km (panels (c), (f) and (i)). The first column shows the total cloud fraction from CloudSat/CALIPSO (upper bound), the second column shows cloud fraction only when there was no precipitation detected at the ground (lower bound) and the third column shows difference between the upper and lower bound of the observations.

lower bound of the observations are shown in the middle panels of Figure 5.3. The difference between two is shown in the right panels of Figure 5.3. The highest cloud fractions are found at the lowest altitude (1.6 km, panels (a), (d) and (g)). As one might expect the differences between the upper and lower bounds for cloud fraction are also largest at that level. The difference between the upper and lower bounds of the observation is large near the center of the composite cyclone, consistent with the co-existence of low clouds and rainfall in that region (see Figure 3.4 (d)). At 4.5 km (panels (b), (e) and (h)), the maximum of cloud fraction is found in the warm frontal region. The superposed field in these panels is vertical motion which shows the familiar dipole structure discussed in earlier chapters. The cloud free region is behind the system, in the region of descent. The difference between the upper and lower bound is largest in the warm frontal region again consistent with the rainfall distribution in Figure 3.4. At 9.7 km (panels (c), (f) and (i)), the maximum of cloud fraction moves to the eastern side of the cyclone center. The superposed field here is relative humidity (%). As found earlier, the maximum of relative humidity and the maximum of cloud fraction align well. The region behind the system is cloud free and dry. The difference between the upper and lower bounds of cloud fraction is small at this level, indicating that many of the high clouds do not produce significant precipitation at the surface.

As in previous chapters, cross-sections taken at lines AB and CD in Figure 5.3 are shown in Figure 5.4. A tilted cloud structure is clearly visible in the section taken at 500 km north of the cyclone center (panel (a)), as previously seen in the Chapter 3. Relative humidity matches well with cloud field with two peaks, one at the lower levels, at about 2 km and another at high levels around 10 km. As expected from Figure 5.3, the difference between the lower and upper bounds of observed cloud fraction is largest at low levels. Below 3 km, this difference is largest at the eastern side of the cyclone center. The cross-section taken at 500 km east of the cyclone center is shown in panels (b), (d) and (f). Most of the clouds are in the region of ascent with two peaks, one at about 2 km and another at about 6 km. The region of descent is cloud free. The difference between two bounds is maximum below 3 km, east of the cyclone center.

In summary, excluding CloudSat/CALIPSO observations that contain precipitation at the surface primarily reduces cloud fraction at low levels in and near the center of the composite cyclone and to the south of the cyclone. Given the large differences and the uncertainty in the observations combined with the absence of simulator information, we treat the two observational cloud fraction estimates as

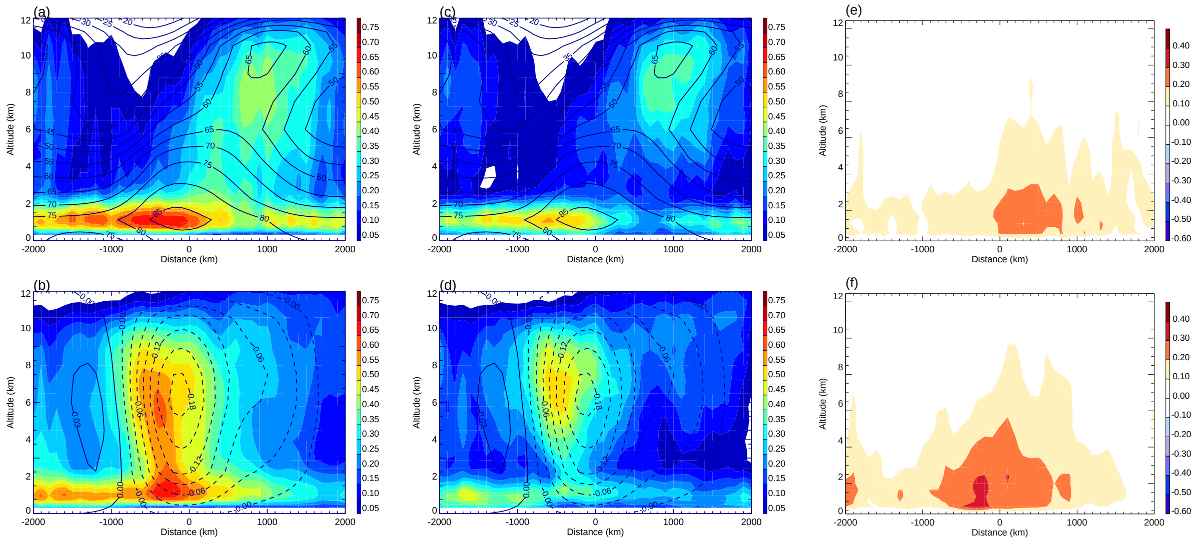

Figure 5.4: Cross section of cloud fraction along the lines CD and AB in Figure 5.3. Panel (a) : Upper bound of cloud observation and RH (%) at line CD, (b): Upper bound of cloud observation and ω (Pa/s) at line AB, (c): lower bound of cloud observations and RH at line AB , (d): lower bound of cloud observations and ω at line AB (e) and (f) show the difference between the upper and lower bound of cloud observations at lines CD and AB, respectively. Dynamical fields are contoured and cloud fields are shaded.

upper and lower bound in the model evaluation performed in the next sections.

5.6 Evaluation of the three-dimensional structure of the model composite cyclone

In this section, we evaluate the cloud structure simulated by the ACCESS model against observations. As for the observed cyclones we use 2 years of model simulations to compare with CloudSat/CALIPSO observations. We extract the bulk cloud fraction field from the model without using any simulator. We also use model-simulated MSLP, relative humidity and ω. First, the model cyclones are tracked using the method of Bauer and DelGenio (2006) applied to the MSLP field of the model. We find 3367 cyclones to composite in the 40^0 S-50^0 S latitudinal band. Using the compositing method described in Chapter 3, model fields for MSLP, vertical motion, relative humidity and cloud fraction related to tracked cyclones were composited and are shown in Figures 5.5 and 5.6. Note again that the observed cloud fractions are averaged over the depth of the model layers, which are 0.2 km for 1.6 km level, 0.5 km for the 4.5 km level and 0.7 km for the 9.7 km level.

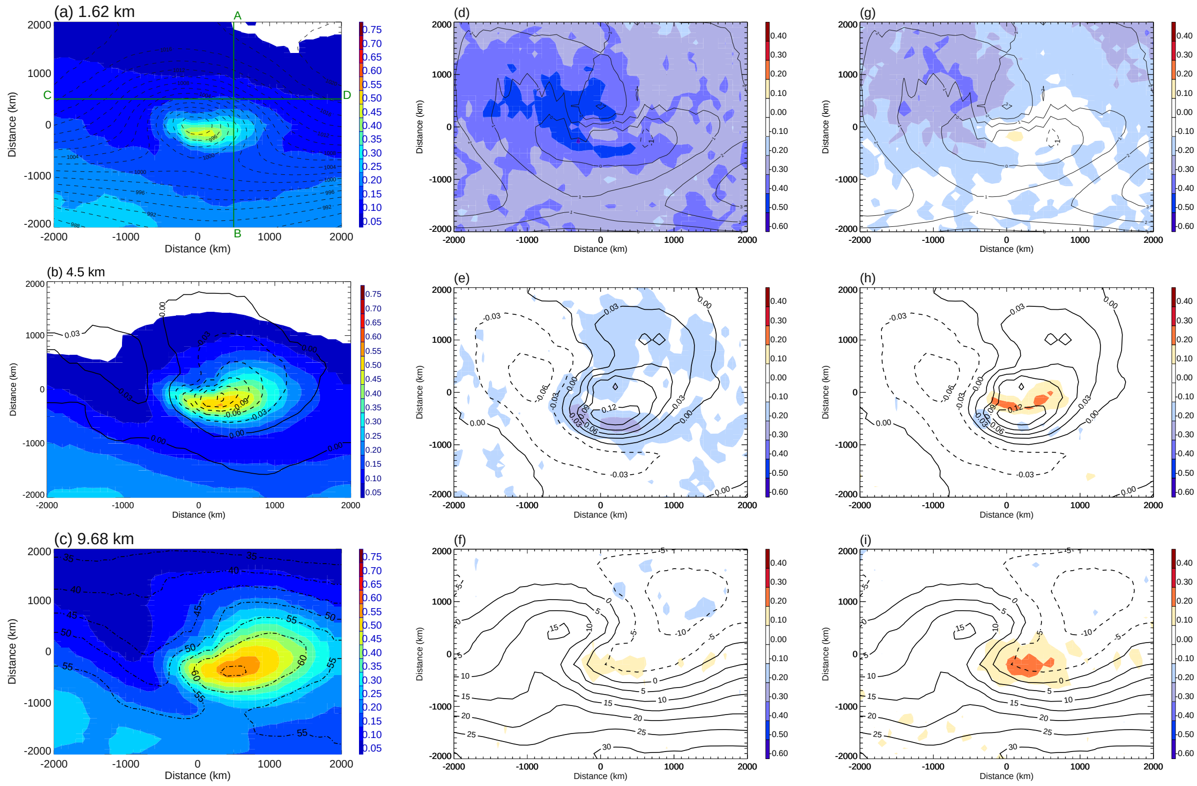

Figure 5.5: Model cloud fraction and differences with the observations at three different heights. At height 1.6 km, panel (a) : cloud fraction and MSLP (hPa) from model simulation , (d): difference between model cloud fractions and the upper bound observations along with the MSLP error, (g): difference between model cloud fractions and the lower bound observations along with the MSLP error. At height 4.5 km, panel (b) : model cloud fraction and ω (Pa/s), (e): difference between model cloud fractions and the upper bound observations alongwith ω - differences, (h): difference between model cloud fractions and the lower bound observations along with ω - differences. At height 9.7 km, panel (c) : model cloud fraction and relative humidity (%), (f): difference between model cloud fractions and the upper bound observations along with RH- differences, (i): difference between model cloud fractions and the lower bound observations along with RH - differences. Dynamical fields are contoured and cloud fields are shaded.

Figure 5.5 shows the model results in the left panels. The difference between model and the upper bound of the observations is shown in the middle panels and the difference with the lower bound is shown in the right panels. While the model and the observations exhibit broadly similar cloud structures, there are significant model deficiencies. At 1.6 km, the model has high cloud fraction near and to the eastern side of the composite model cyclone center. The observed cloud field covers a larger area than the model in particular in the north-west part of the cyclone. The model has minimum of 994 hPa MSLP near the center of the cyclone. The differences of MSLP with the reanalysis in panels (d) and (g) show that model cyclones are not deep enough compared to the observed composite cyclone. This is consistent with Bauer and DelGenio (2006) who showed that GCM cyclones are shallower than those in the reanalysis. Figure 5.2 showed a large bias in the model shortwave CRE at north-west part of composite cyclone. The lack of clouds at lower levels is consistent with that bias.

At mid-levels around 4.5 km, clouds can be seen in the eastern part of the composite model cyclone center in panel (b) of Figure 5.5. As before, the superposed field here is vertical motion. The vertical motion field shows a dipole structure as in the observations (cf fig 5.3 panel (b)) with rising motion at the eastern side of the cyclone center and sinking motion to the west of the cyclone center. However, the vertical motion in the model is weaker than observed. The rising motion is $\approx$ 50 % weaker and follows a comma shaped structure with an exaggerated north-east tilt compared to the observations (panels (e) and (h)). The descending motion is also weak compared to the observations. Most of the clouds are in the region of rising motion and the region of descent is cloud-free as it is in the observations. The model likely underestimates cloud fraction in the region of ascent (panels (e) and (h)), with values close to the low observational estimate.

Panel (c) of Figure 5.5 shows the cloud fraction and relative humidity from the model at 9.7 km. The maximum of the model cloud fraction is well matched with the maximum of relative humidity. Clouds occur mainly in the eastern part of the cyclone. There are no clouds behind the composite cyclone center, consistent with very dry air in the region. The model produces slightly larger cloud fractions than observed, in particular near the center of the composite cyclone. However, in the north-eastern part of the cyclone, the model underestimates cloud fraction consistent with lower values of relative humidity than observed (panels (f) and (i)). To the west of the cyclone center, the model has relative humidity values higher than

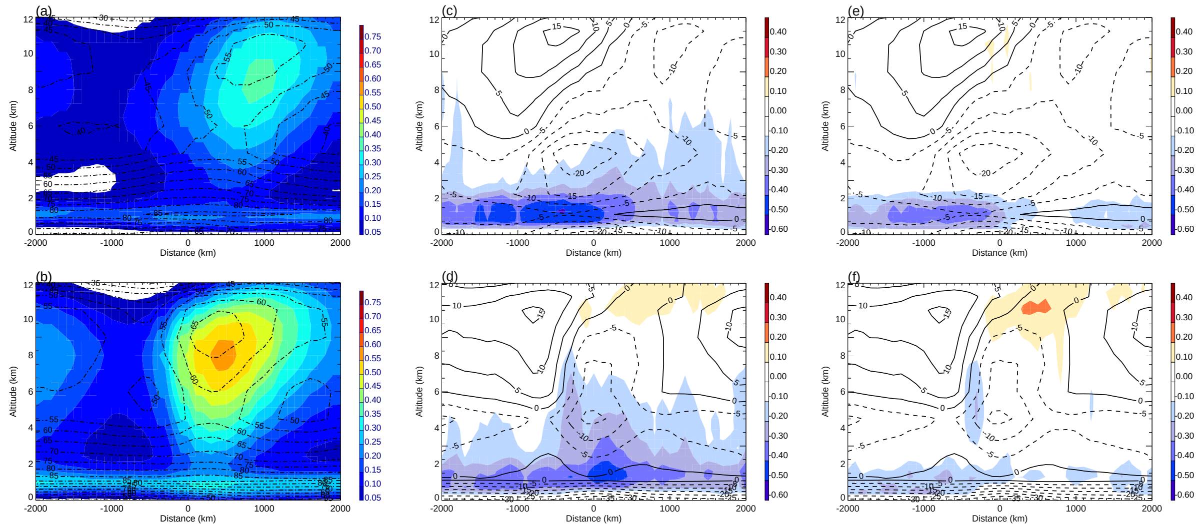

Figure 5.6: Cross section of RH and cloud fraction along the lines CD and C1D1 in Figure 5.5. Model cloud fraction and RH (%) are shown in (a) at line CD and in (b) at line C1D1. Panels (c) and (d) show the difference between the model cloud fraction and RH and the upper bound observations while panels (e) and (f) show the difference between the model cloud fractions and RH and the lower bound observations. RH is contoured and cloud fields are shaded.

the observation, consistent with the weaker circulation identified at lower levels.

Four cross-sections taken at 500 km north of the cyclone center and 500 km south of the cyclone center, 500 km east of the cyclone center, 100 km west of the cyclone center are shown in Figures 5.6 and 5.7. Figure 5.6 shows the cross-section taken at 500 km north of the cyclone center and 500 km south of the cyclone center along with the model error calculated from the two observational estimates. Panels (a) and (b) show a maximum cloud fraction near the center of the composite cyclone at low levels that gradually extends further eastwards at higher levels. In the cold frontal region (panel(a)) the maximum of relative humidity lies around 1.5 km. Cloud fraction reaches its maximum at about 8 km height to the east of the composite model cyclone center. The region behind the system is cloud free and dry. Cloud fraction at low levels is underestimated compared to both sets of observations (panels (c) and (e)). The relative humidity values at high levels in the model are underestimated in the eastern part of the cyclone and overestimated in the western part again hinting at a too weak ascent and descent in and behind the cyclone center.

The cross-section of clouds and relative humidity from the model taken at 500 km south of the cyclone center, where cloud fraction values were highest in the observations (cf. Figure 5.3) is shown in panel (b) of Figure 5.6. Similar to panel

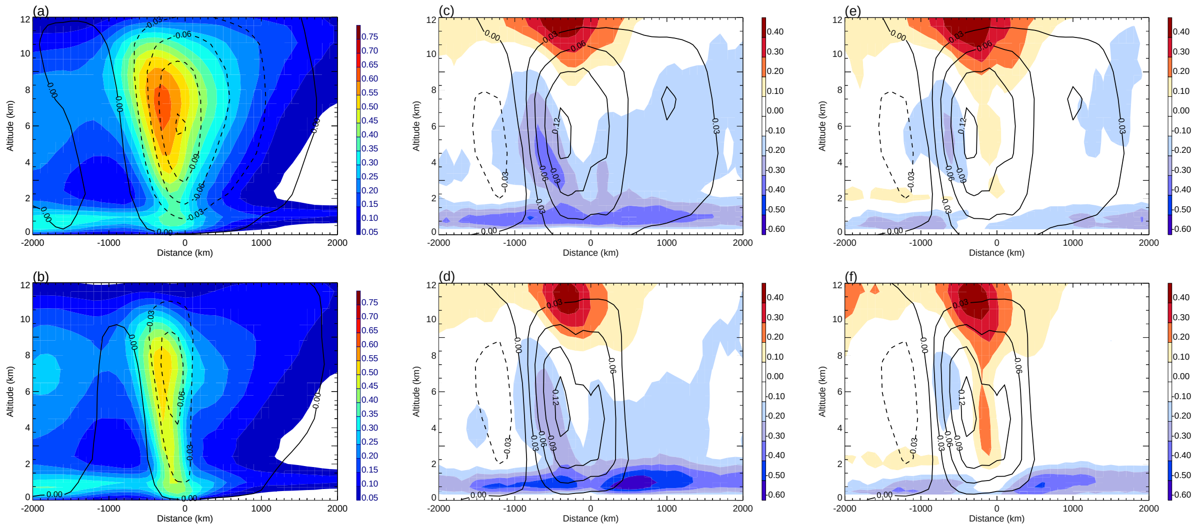

Figure 5.7: Cross section of ω (Pa/s) and cloud fraction along the lines AB and A1B1 in Figure 5.5. Model cloud fraction and ω are shown in (a) at line AB and in (b) at line A1B1. Panels (c) and (d) show the difference between model cloud fraction and ω and the upper bound observations while panels (e) and (f) shows the difference between model cloud fractions and ω and the lower bound observations. ω is contoured and cloud fields are shaded.

(a), the lower level clouds are underestimated. There is a severe negative bias in the relative humidity in the subcloud layer. The cloud fraction values are slightly higher in the model than observation above 10 km height, consistent with slightly higher values of relative humidity. The model is too dry in the eastern part of the cyclone and too moist behind the composite cyclone center compared to the observations.

Composited cloud fraction and vertical motion from the model at 500 km east of the cyclone center are shown in the Figure 5.7(a). This cross-section passes through the warm frontal region (cf Figure 5.3). There is a maximum in cloud fraction at the center of the composite model cyclone center which gradually extends further south at higher levels. These clouds are underestimated in the model below 8 km, mainly to the south of the cyclone center. However, clouds above 9 km are overestimated in the model (panels (c) and (e)). Most of the clouds are in the region of ascent. The region of descent is cloud-free except at very low levels, where model cloud fraction is once again too low. As was already evident in Figure 5.5, the rising motion and the descending motion are too weak in the model compared to the observation.

The cross-section of cloud fraction and vertical motion from the model taken behind the system, at 100 km west of the cyclone center, is shown in panel (d) of Figure 5.7. The underestimation of clouds in the model al lower levels is most severe behind the system, to the north of composite cyclone center. The upper level clouds are again overestimated in the model. The vertical motion field is weak in the model compared to observations.

5.7 Air parcel trajectories in the model cyclone

In order to see how airflows in the cyclone are represented in the model, we will perform trajectory analysis introduced in Chapter 3 on the model. As in Chapter 3, 48-hour back trajectories are drawn in Figure 5.8 at three different pressure levels, namely, 850 hPa, 500 hPa and 250 hPa. Using the composite of u,v and w component of the wind in the model, the path followed by the air parcel is tracked back for every hour. The black points denote end point of trajectory. The difference in pressure level is denoted by the colour of trajectory. the equivalent trajectories for the observations are shown in Figure 3.11.

At 850 hPa, the descending motion is evident at the western side of cyclone and ascending motion is evident in the eastern part of cyclone. Near the center, the air rises and turns cyclonically. Compared to the observations (cf. Figure 3.11(a)), the circulation near the center is not as closed. Air in the north-eastern part of the cyclone does not sufficiently turn cyclonically as it did in the observations. In the model, this air rises and turns anticyclonically and moves away from the cyclone center. The descending motion is weak compared to the observations (cf. Figure 5.5).

At 500 hPa, strong westerly motion is evident in the model. The western part of cyclone shows descending motion and the eastern part of cyclone mostly shows ascending motion. Near the center and to eastern part of cyclone, air rises up to 3-7 hPa per hour, however, it does not turn cyclonically in the warm frontal region which is contradictory to the observations (cf. Figure 3.11(b)). The representation of the warm conveyor belt is poor in the model.

Consistent with the observations, at 250 hPa, strong westerlies are dominant in the model. In the eastern part of the cyclone, air rises and turns anticyclonically to the far eastern side of the cyclone center. Consistent with the observations, the south-western part of the model cyclone shows the ascending motion.

Figure 5.9 shows the values of cloud fraction along the trajectories. This Fig-

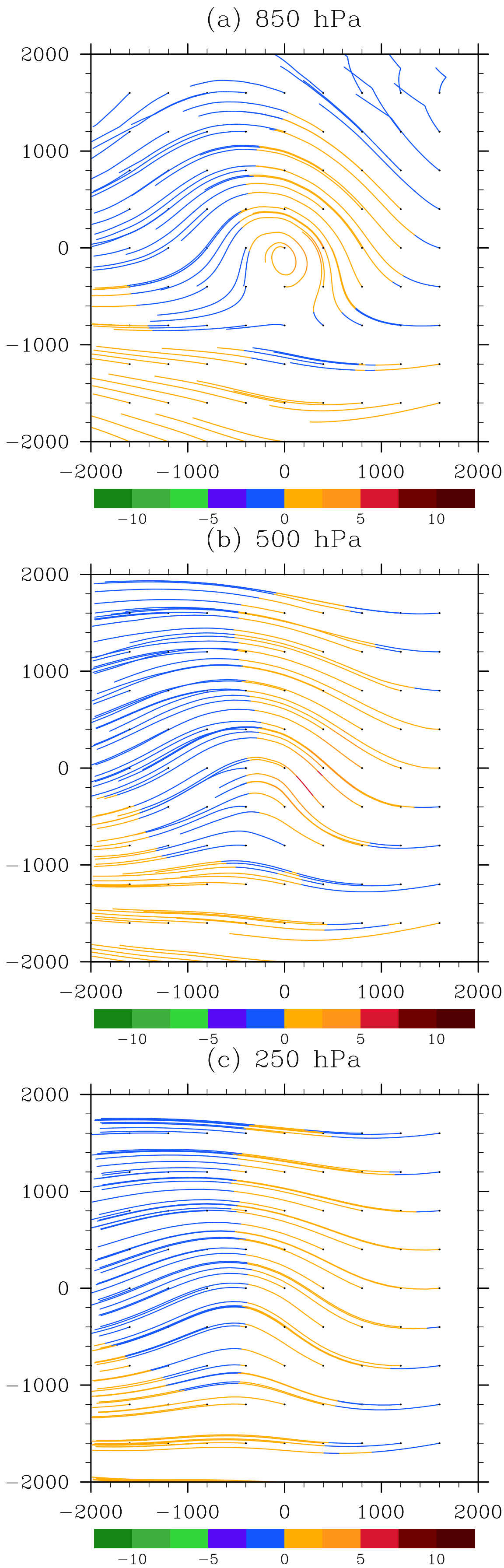

Figure 5.8: 48 hours back trajectories at (a) 850 hPa, (b)500 hPa and (c) 250 hPa for the composite model cyclone. The colour of the trajectory denotes the difference in pressure level every hour. The end point of the trajectory is shown by a black dot.

ure should be compared to Figure 3.12 for the observations. At 850 hPa, near the cyclone center, the cloud fraction reaches values of only 0.5, consistent with the deficient cloud cover at low levels in the model (cf. Figure 5.5). Most of the cyclone area shows cloud fraction values less than 0.25, whereas in the observations, the minimum value of cloud fraction is 0.25 (cf.Figure 3.12 (a)). At 500 hPa, the higher values of cloud fraction are evident in the eastern part of cyclone. However, the model has values less than 0.25 for cloud fraction in the remaining part of the cyclone, except in the south-west corner. At 250 hPa, the relatively high cloud fractions are evident at far eastern side of the cyclone center.

The values of relative humidity along trajectories are shown in Figure 5.10. Similar to the observations (cf Figure 3.13), higher values of relative humidity can be seen at 850 hPa, compared to the other levels. In the region of ascent relative humidity reaches up to 80 %. However, cloud fraction values along these trajectories are not that high (cf Figure 5.9) indicating a poor relationship between relative humidity and cloud fraction in the model. Trajectories ending in the region of descent show lower values of relative humidity. At 500 hPa, the region of ascent shows moderate values of relative humidity and the region of descent shows lower values of relative humidity. The difference between values of relative humidity in the region of ascent and in the region of descent is smaller than the observations. At 250 hPa, moderate values of relative humidity are evident at far eastern side of the cyclone center consistent with higher cloud fraction found in the region (cf Figure 5.9). Contradictory to the observations, there is no much difference between the values of relative humidity at the eastern and western part of cyclone.

From the above discussion it is evident that while the overall cloud structure is well captured by the model there are some significant model errors. High-level cloud occurrence is somewhat overestimated while low-level cloud occurrence is severely underestimated. There are too few clouds behind the system and too many high clouds in the warm frontal region, compared to observations. The model cyclones are shallower than observations. The circulation around the cyclone is too weak in the model. Moreover, airflows in the cyclone are poorly represented by the model. To shed more light on the model errors, the relationship between clouds and the cyclone dynamics in the model will be explored and compared with observations in the next section.

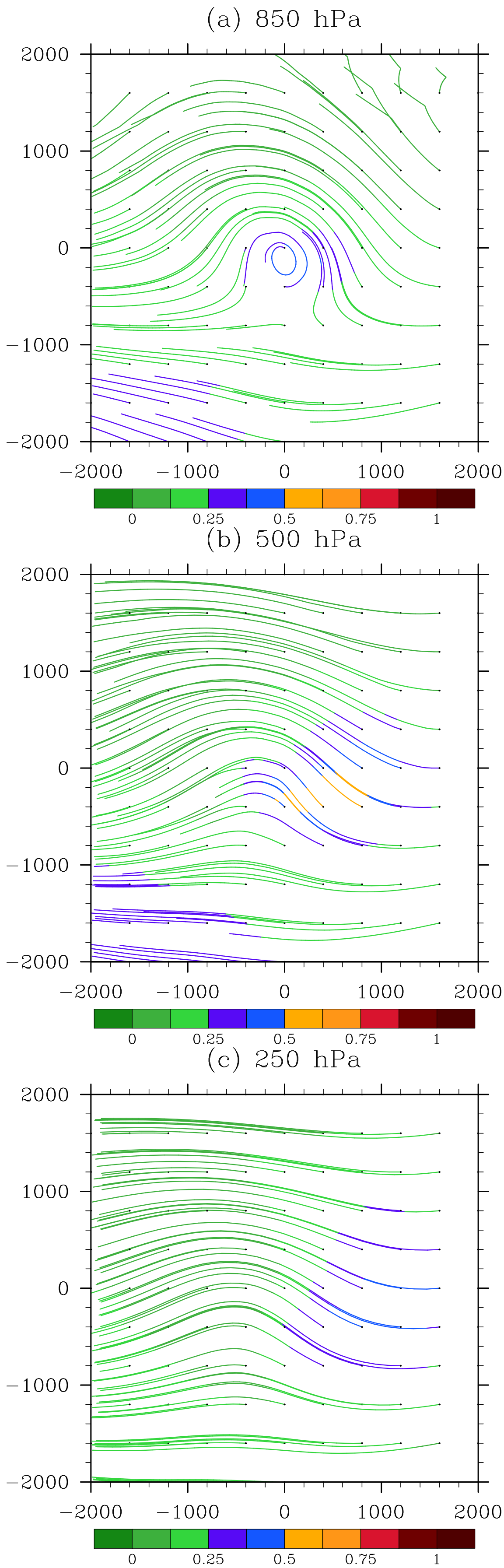

Figure 5.9: 48 hours back trajectories at (a) 850 hPa, (b)500 hPa and (c) 250 hPa for the composite cyclone. The colour of the trajectory denotes the value of cloud fraction every hour. The end point of the trajectory is shown by a black dot.

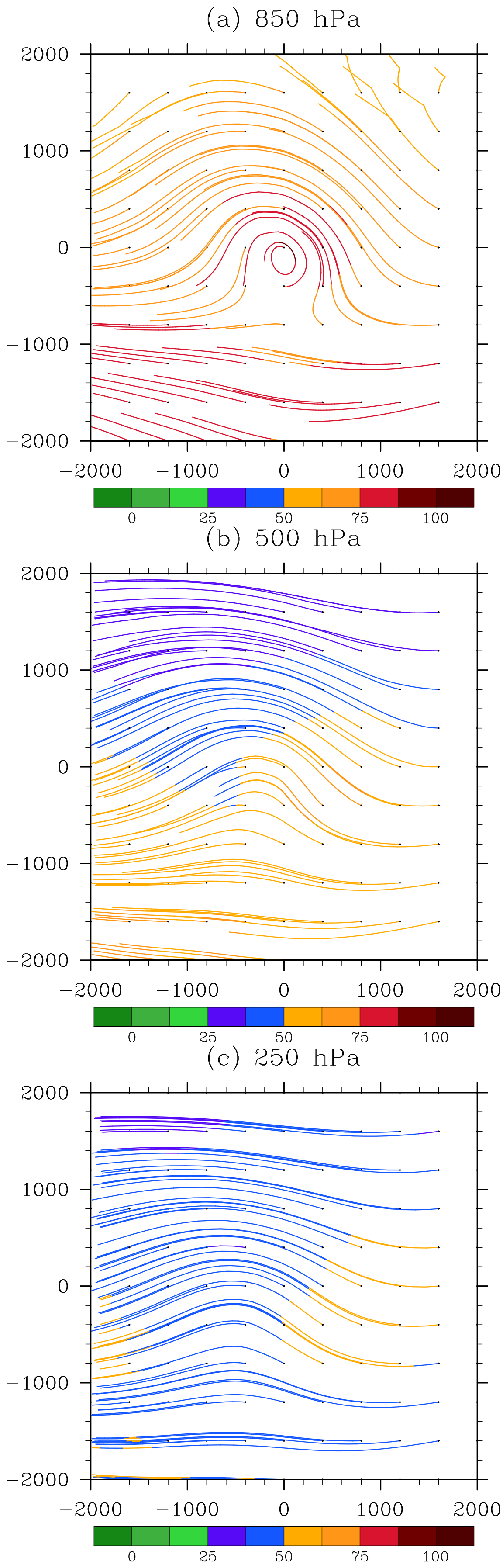

Figure 5.10: 48 hours back trajectories at (a) 850 hPa, (b)500 hPa and (c) 250 hPa for the composite model cyclone. The colour of the trajectory denotes the value of relative humidity every hour. The end point of the trajectory is shown by a black dot.

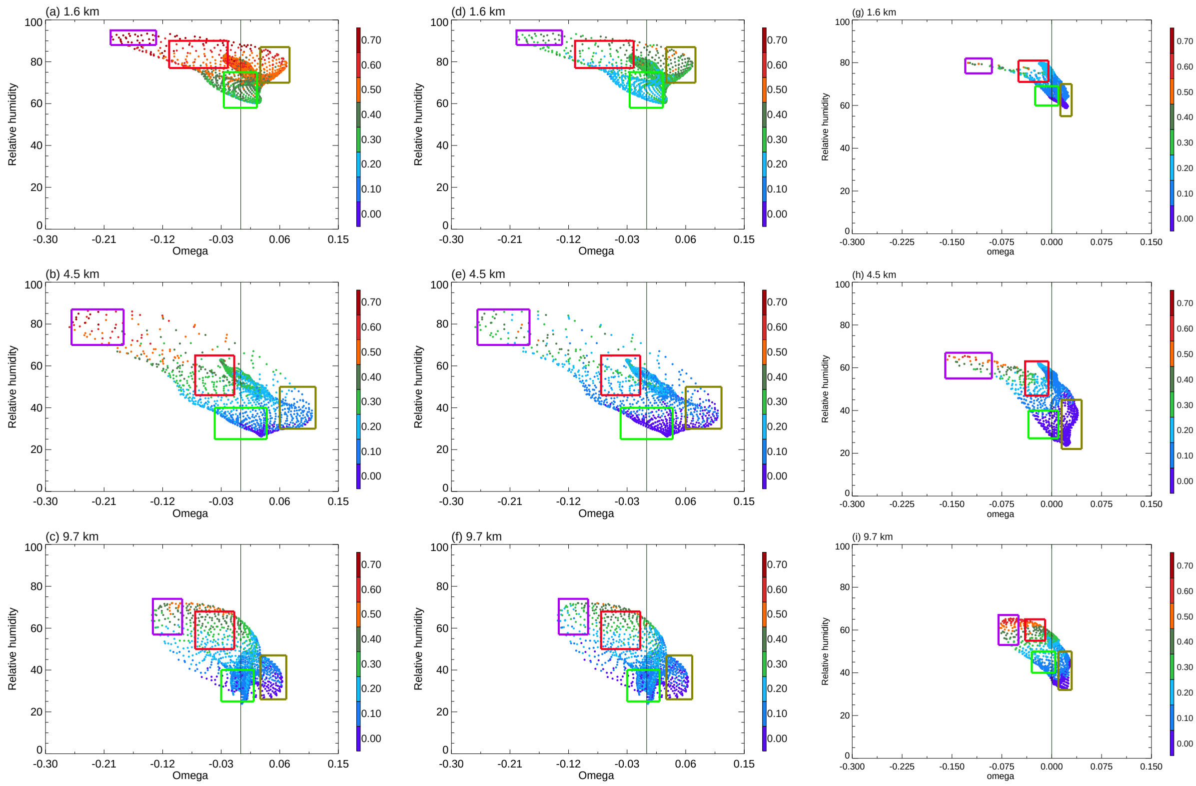

Figure 5.11: Cloud fraction in terms of the ω (Pa/s) and relative humidity (%) from observations and from the model at height 1.6 km (panels(a), (d) and (g)), 4.5 km (panels(b),(e) and (h)) and 9.7 km (panels (c), (f) and (i)). The first column shows results from the upper bound cloud observations, the second column shows results from the lower bound of cloud observations, while the third column shows results from model. The colour of the point denotes the value of cloud fraction.

5.8 Evaluation of the model's cloud-to-dynamics relationships

After investigating the overall distribution of clouds and key dynamical fields in the model in the previous section, we now study more closely how the clouds relate to the dynamics. Figure 5.11 shows relationship between vertical motion, relative humidity and cloud fraction at three different heights. The two observational estimates are shown in the first two columns and the model values in the last column. The X-axis denotes vertical motion and the Y-axis relative humidity. The colour of the point denotes value of cloud fraction. The first column shows the upper bound of the observations and the middle column shows the lower bound. Note that the shape of the scatter plot remains the same for the first two columns as the observed vertical motion and relative humidity are from the NCEP reanalysis in both. However, the colour of the points changes according to value of cloud fraction in two observational estimates.

Panel (g) of Figure 5.11 shows cloud fraction - vertical motion - relative humidity relationship at 1.6 km, in the model. It is evident that the shape of the scatter plot from the model is very different from the observations (Panels (a) and (d)). The values of cloud fraction are very small in the model, consistent with the underestimation of clouds in the model shown in Figure 5.5. The range of vertical motion and relative humidity is much smaller than observed. The maximum value for the ascent is -0.12 Pa/s and the maximum value for relative humidity in the model is 80 % compared to -0.24 Pa/s and 95 % in the observations. Hence the model clouds exist in much drier air than those in the observations. The descent in the model is also weaker than in the observations. The region of descent with high values of relative humidity is essentially absent in the model. As for the region of ascent, the clouds found in the region of descent again exist in lower than observed relative humidities.

At 4.5 km, the model relative humidity reaches upto 65 % and its ascent value peaks around -0.18 Pa/s (Panel (h) of Figure 5.11). The range of all variables is again too small compared to the observation. However, in relative terms the range of vertical motion and relative humidity at this mid-level is larger than at the other two levels shown, which is consistent with the observations. The region of descent is more limited than observed and clouds in the region of descent are largely absent. This figure is consistent with the weak vertical motion field in the model, shown in Figure 5.5.

Consistent with Figure 5.5, the values of model cloud fraction at the 9.7 km level (panel (i) of Figure 5.11) are higher than those in the observation. This is despite the fact that the ascent in the model is more than 50% weaker than observed. The descent values are again too small compared to observations also.

While the model clearly underestimates the variability of the dynamical fields across the cyclone it is still of interest to investigate where different areas of Figure 5.11 are located in space. Equivalent to Figure 3.14, the coloured boxes drawn in the Figure 5.11 denote areas of particular interest in the observations and in the model. Figure 5.12 shows the position of points in each coloured box related to the (composite) cyclone center in the observations (first row) and in the model (second row). The colour showing the position of the point in Figure 5.12 and the colour of the box in the Figure 5.11 in which that point is located, are matched.

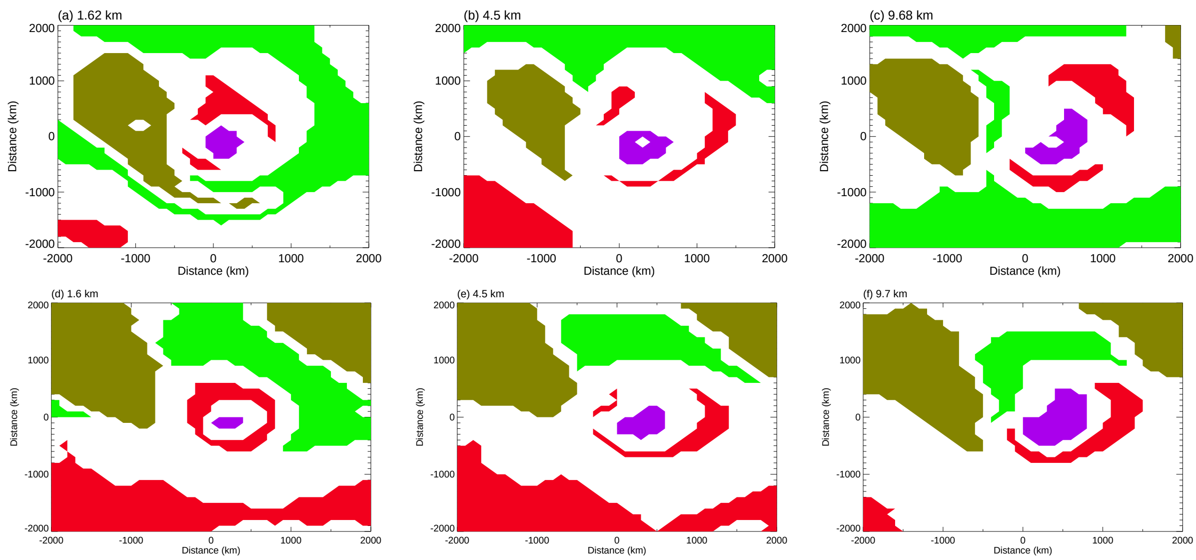

Figure 5.12: Region of particular interest at (a) and (d) 1.6 km, (b) and (e) 4.5 km and (c) and (f) 9.7 km height. The first row shows results from observations while the second row shows results from the model.

The purple box includes the points where the highest relative humidity and highest ascent value are achieved in both the observations and in the model. These points are located near and to the east of the cyclone center in both observations and model at all heights (cf. Figure 5.12). The red box includes points of medium ascent and mid-to-high values of relative humidity. These points surround the region with the highest ascent values and highest humidity values near the cyclone center in both model and observations. Points with these characteristics can also be seen in the south-western part of the domain. The points in the region of descent are relatively dry and can be found behind the system in both model and observations. Unlike the observations the model also produces points with high descent values and low values of relative humidity in the north-eastern part of the cyclone. The remaining points have small vertical motion and relative dryness in both, the observations and the model. The Figure illustrates that in a relative sense the model represents the cyclone structure well even though the absolute values of key variables tend to have too small a variability across the composite.

To further illustrate this point, we show the relationship in Figure 5.12 in two more ways. Figure 5.13 shows the relative humidity in terms of vertical motion and cloud fraction in the model at three different heights. At 1.6 km, the points in the region of ascent have higher values of relative humidity. The region of descent is dry and shows lower values of cloud fraction. Compared to Figure 3.15, the range of all three variables is too small at all three heights. The shape of the scatter plots for all

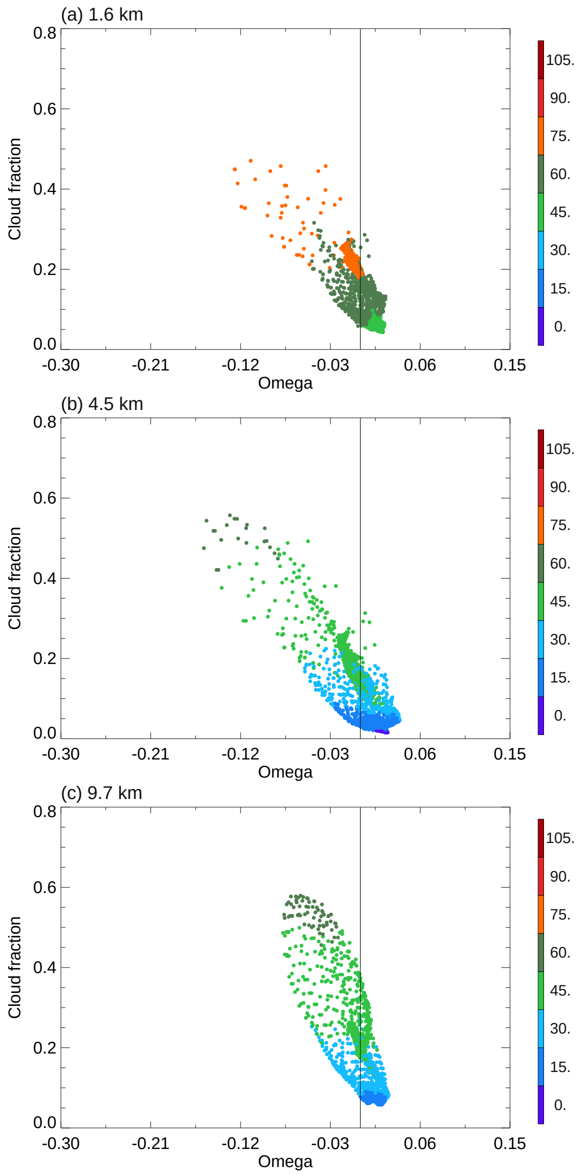

Figure 5.13: Relative humidity (%) in terms of the ω and cloud fraction from the model at (a) 1.6 km, (b) 4.5 km and (c) 9.7 km height. The colour of the points denotes the value of relative humidity.

three heights is again very different in the model from that in the observations (cf. Figure 3.15). Furthermore, the steepness in the scatter plot increases with height in the model. However, in the observations, the steepness remains overall the same for all heights. In the model many points are located in a small region which is contradictory to observations where all the points are distributed over larger area (cf. Figure 3.15). Also, the relationship between the three variables remain quite strong at 9.7 km contradictory to observations, where it weakens (cf panel (c) of Figure 3.15). The number of points with high values of relative humidity is larger at 9.7 km than that at 4.5 km which is consistent with highest values of cloud fraction found at the higher level (Figure 5.11).

Figure 5.14 shows vertical motion in terms of the relative humidity (%) and cloud fraction in the model. It is evident that the model does not show the quasi-linear relationship between relative humidity and cloud fraction seen in the observations (Figure 3.16). The vertical motion in the model is weaker than in the observations consistent with Figure 5.5. The range of all variables is again too small compared to the observations as previously seen in Figures 5.11 and 5.13.

In summary, we find that while the model produces an overall good spatial cloud structure related to extra-tropical cyclones, the relationship between cloud fraction and the larger scale dynamical variable is not correct compared to the observations. The range of most dynamical variables in the composite cyclone is smaller than observed, indicating that the dynamical properties of the model cyclones are not well simulated. We will now investigate if these errors in the cloud -to-dynamics relationship are a function of the stage of the cyclone life cycle by examining the relationship across the four life cycle classes defined in Chapter 4.

5.9 Classification of cyclones in the model

We apply the cyclone classification method introduced in Chapter 4 to stratify the model cyclones into four classes in order to understand whether the model represents the different structures of cyclones seen in the observations. As in Chapter 4, these four classes are the High Pressure Deepening (HPD) class, the Low Pressure Deepening (LPD) class, the Low Pressure Filling (LPF) class, the High Pressure Filling (HPF) class. The model has 439 cyclones in the HPD class, 443 cyclones in the LPD class, 162 cyclones in the LPF class and 159 cyclones in the HPF class. The model has more deepening cyclones compared to the observations and fewer filling

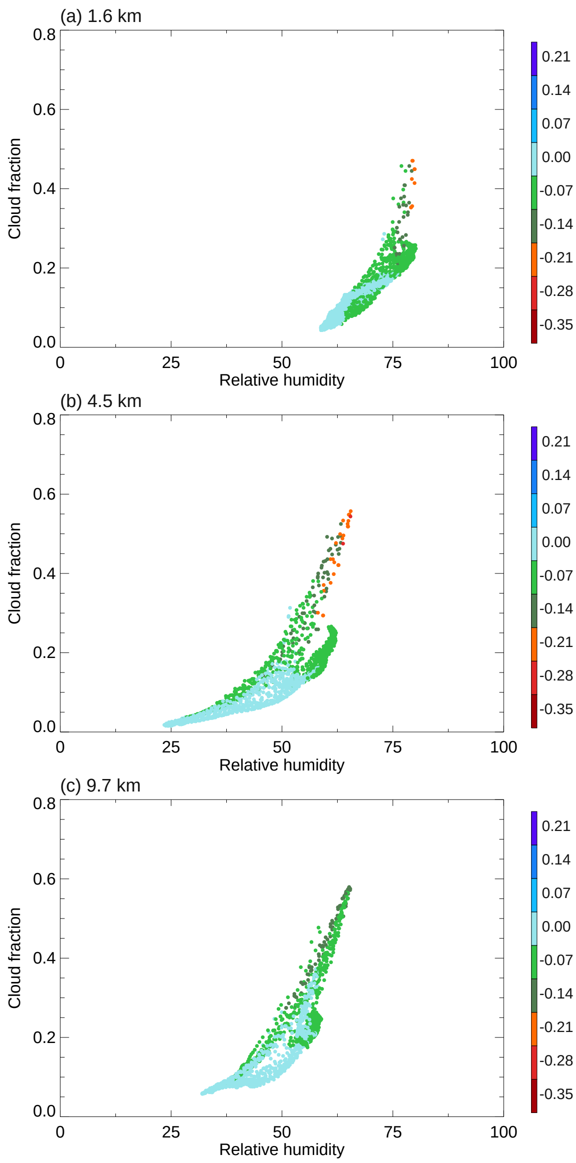

Figure 5.14: Vertical motion (Pa/s) in terms of the relative humidity (%) and cloud fraction from the model at (a) 1.6 km, (b) 4.5 km and (c) 9.7 km height. The colour of the points denotes the value of vertical motion.

cyclones (see Table 4.1 in chapter 4). This implies that the model cyclones must be deepening slowly and filling fast, so we detect more of the deepening cyclones and less of the filling cyclones.

Figure 5.15 shows the cloud fraction for all four classes in the model. For all three heights, the cyclone follows an evolution similar to the observations. In the HPD class, the cloud structure starts developing, in the LPD class it becomes mature, in the LPF class it starts dissipating and in the HPF class it shows its lowest values. The first column of the Figure 5.15 shows the cloud fraction and MSLP for all classes at 1.6 km. As would be expected from the definition of the classes, the LPD class has the lowest MSLP at the center. The minimum MSLP is 998 hPa for the HPD class, 978 hPa for the LPD class, 982 hPa for LPF class and 1004 hPa for HPF class. Compared to observations (cf. Figure 4.5), the minimum MSLP is 2 hPa less in the HPD class, 8 hPa less in the LPD class, 4 hPa less in the LPF class and 2 hPa more in the HPF class. Here we clearly see evaluation of cyclone through four classes. The cyclone reaches its minimum MSLP in the LPD class and in the filling classes the central MSLP gradually rises to achieve its maximum in the HPF class. Cloud fraction is high near the center of the cyclone for all classes. Consistent with the observations (cf. Figure 4.5), the model LPD class has the highest values of cloud fraction.

The second column of Figure 5.15 shows cloud fraction and vertical motion from the model for all four classes. As it was in the observations (Figure 4.6), the rising motion is at the right side of the cyclone center while the descending motion is at the left side of the cyclone center, behind the system. The maximum ascent is found in the LPD class consistent with the highest cloud fraction in the class. Behind the system, in the region of descent, cloud fraction values are very small agreeing with observation. Consistent with the observations, the rising motion follows a comma shaped structure as that in the cloud field. The vertical motion field also reveals the evolution of the model cyclone by exhibiting the strongest ascent in the LPD class which weakens in the filling classes. In the filling classes, the rising motion field becomes less well defined. Like the observations (Figure 4.6), the descending motion slightly strengthens in the filling classes in the model. There is no shift of the region of ascent and its associated cloud structure towards the eastern side of the cyclone center in the filling classes which is evident in the observations (Figure 4.6). The values of the cloud and vertical motion field are lower in the model than they were in the observations (Figure 4.6).

Cloud fraction and relative humidity from the model at 9.7 km are shown in the third column of Figure 5.15. The eastern side of the cyclone center has higher RH than the western side, consistent with the observations. For the deepening classes, relative humidity values are higher than those in the filling classes, similar to the observations, again confirming the similarity of the evolution of the cyclone in the model and in the observations. Behind the system, humidity values are relatively low and are accompanied by very low values of cloud fraction. In the filling classes, the southwestern part of the cyclone becomes wetter and achieves higher values of cloud fraction similar to the observations. The cloud fraction and relative humidity values are lower in the model than their observations at this height (Figure 4.7). Contradictory to observations, there is no shift of the wet region with high values of cloud fraction to the eastern side of the cyclone center.

Overall, the model represents the cyclone evolution similar to the observations through the four classes. Like the observations, all dynamical and cloud fields are stronger in the deepening classes for the model and they start to weaken once the cyclone entered into filling stage. The higher cloud fractions are found in the region of ascent which also have higher values of relative humidity. However, the cloud fraction and dynamical fields for all classes have lower values in the model when compared to the observations. In the filling classes, the rising motion, the relative humidity and the cloud field are less well defined in the eastern side of the cyclone. We will now examine how the relationships between the dynamical and cloud fields change with cyclone class in the model.

Figure 5.16 shows the cloud fraction in terms of vertical motion and relative humidity at three different heights for all four classes in the model. At 1.6 km, the cloud fraction values are highest in the LPD class, consistent with the observations (cf. Figure 4.15). As seen in Figure 5.15 all fields are stronger in the deepening classes than that are in the filling classes. As seen for the mean cyclone in Section 5.8, the range of all variables is considerably smaller compared to the observations for all classes (see Figure 4.15). Similar to the observations, higher cloud fractions are found in the region of ascent. The region of descent is relatively dry and has very small values of cloud fraction. In the HPF class, the relationship between the three variables becomes weak in the model, consistent with the observations.

At 4.5 km, the ascent values reach their peak in the LPD class, similar to the observations. The filling classes have very low values of cloud fraction and show a very weak relationship between variables. Unlike the observations, the region of ascent

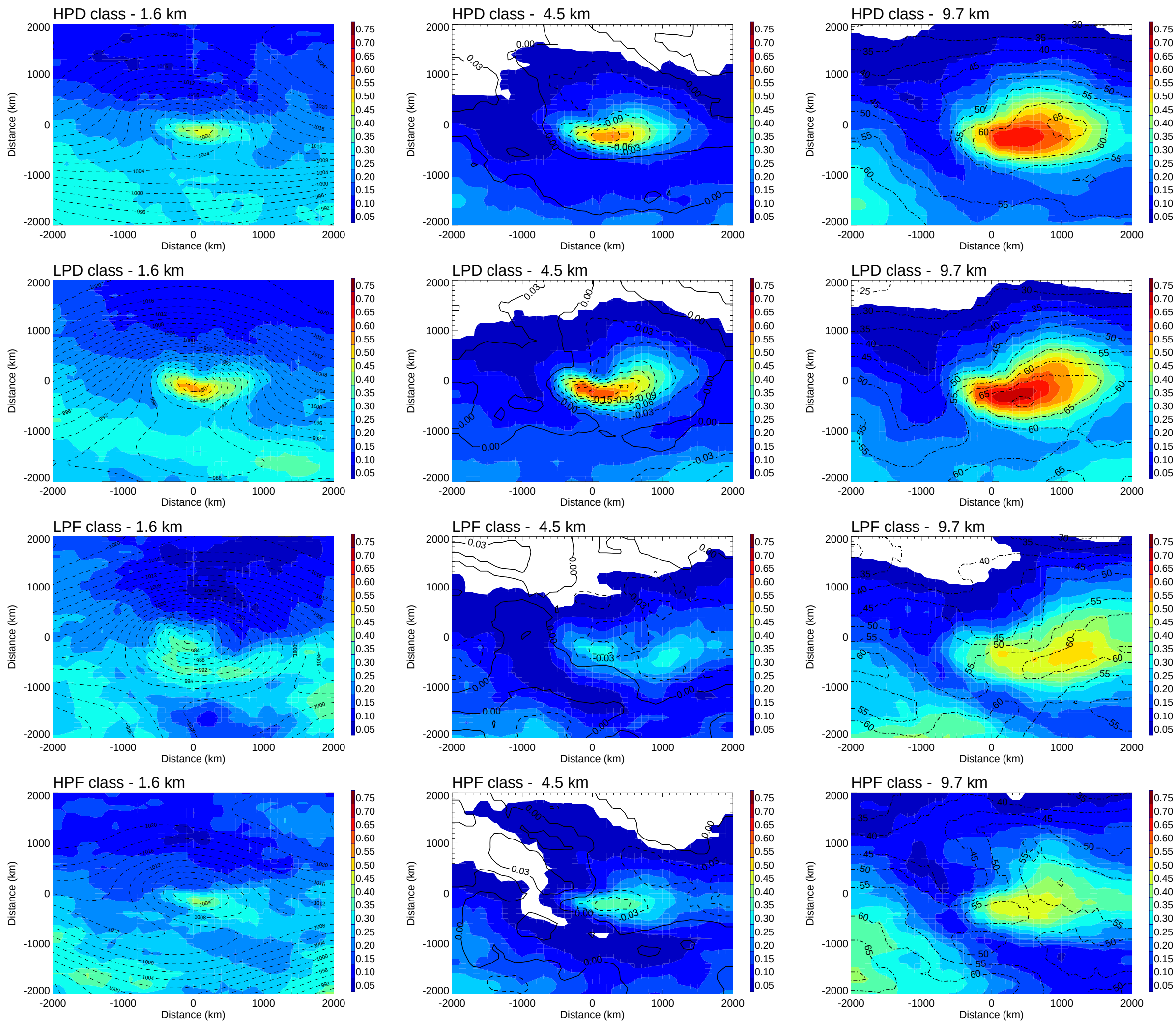

Figure 5.15: Cloud fraction for the four cyclone classes in the model. The cloud field is shaded and the dynamical fields are contoured.

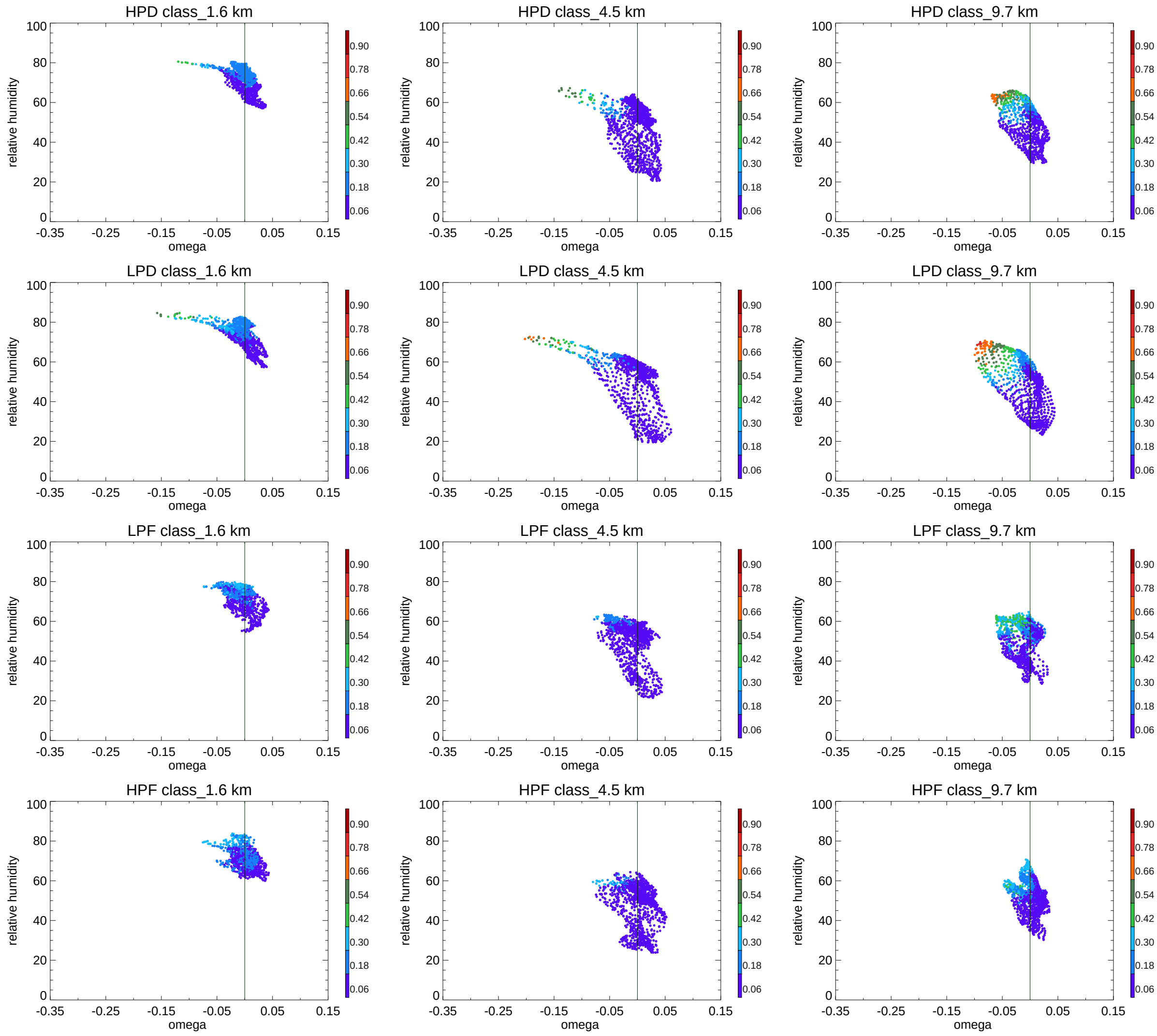

Figure 5.16: Cloud fraction in terms of relative humidity and omega for all four cyclone classes in the model. The colour of the points denotes the value of cloud fraction.

and descent have similar values for cloud fraction and humidity in the HPF class. The relationships between the three variables become weak in the filling classes in the model, consistent with the observations.

The highest cloud fractions at 9.7 km are found in the LPD class which is consistent with the overestimation of clouds in the model at higher levels seen in Figure 5.5. Like at the other two heights, the region of descent has very low values of cloud fraction for all classes. Clouds in the region of descent are essentially absent in the model, contradicting the observations (cf. Figure 4.15). The relationship between the three variables is stronger in the deepening classes and weak in the filling classes, similar to the observations.

5.10 Summary

The purpose of this chapter was to evaluate the ability of a modern climate model, the ACCESS model, to simulate the observed dynamical and cloud features of Southern Hemisphere extratropical cyclones. First, ISCCP cloud observations were compared with the model clouds using the ISCCP simulator. This comparison as well as a comparison of the composite radiation field with observations confirmed the result of earlier studies. Consistent with Bodas-Salcedo et al. (2012) and Field et al. (2011) the model produces a weaker shortwave CRE than the observations. This error is associated with a lack of lower-level clouds behind the system.

After confirming some known model deficiencies, the three dimensional model cloud structure was compared to CloudSat/ CALIPSO observations. For this, the model was run for 2 years without using any simulator. The model fields for bulk cloud fraction, MSLP, vertical motion, relative humidity were extracted. Following the same technique used for the observations the model fields were composited around the cyclone center. To better match the model's vertical resolution, the CloudSat/CALIPSO observations were averaged according to the thickness of the model levels. As we do not have access to the CloudSat simulator and since the CloudSat/CALIPSO mask may contain precipitating particles, we generate two sets of observations. The upper bound of the observations includes the total cloud mask while the lower bound of the observations includes only cloud fraction from pixels for which there was no precipitation at ground. The model is then expected to produce cloud fractions between these two bounds to be deemed successful. Some dynamical fields were also composited around the cyclone center and were compared against observations.

The overall spatial cloud structure around the cyclone center is well captured by the model but the relationship between cloud fraction and larger scale dynamical variables is not well reproduced. When measured by minimum pressure the model has shallower cyclones than observed. The circulation around the cyclone is weaker in the model and there is an underestimation of clouds behind the system, while in the warm frontal region, the model produces too many clouds at very high levels compared with observations. Unlike the observations, the model does not show a quasi-linear relationship between cloud fraction and relative humidity. Ascent and descent values in model are very weak compared to observations indicating that the dynamical properties of the model cyclones are not well simulated. This makes it hard for the model to produce the correct cloud fields.

The model has more deepening and fewer filling cyclones than observed. Consistent with the observations, the dynamical and cloud fields in the model are stronger for cyclones in the deepening classes and they start to weaken once the cyclone enters the filling classes. Overall, the model reproduces the cyclone evolution similar to the observations. However, in the filling classes, the dynamical and cloud fields are less well defined in the model.

This work provides a new comprehensive way to evaluate model's ability in reproducing the cloud and dynamical structure of cyclones. It is shown that the dynamical properties of the cyclones are not well simulated. The clouds related to the cyclone are linked with the airflows in it. If the model does not have the correct dynamics, such as enough rising motion or enough moisture then it will not be able to produce the correct clouds. These errors must be addressed in future model development.

Chapter 6

Summary and conclusions

6.1 Overview

Extratropical cyclones and their associated rain and cloud fields are a prominent feature of the atmosphere. It is important to determine if extratropical cyclones including their cloud structure and the relationship of clouds to dynamical processes are adequately represented in weather and climate models. The Southern Ocean storm tracks and their associated extra-tropical cyclones and fronts are pronounced features of the Southern Hemisphere atmospheric circulation. The cloud field related to these extratropical cyclones plays an important role in the radiation budget of the region. However, clouds in the Southern Hemisphere extratropical region have received relatively less attention than their Northern Hemisphere counterparts. Recent studies show that current models have large biases in the radiation budget over the Southern Ocean (Trenberth and Fasullo, 2010). This study focussed on the Southern Hemisphere and aimed to, for the first time, provide a comprehensive three-dimensional picture of Southern Hemisphere extratropical cyclone cloud structures together with the dynamical background they are embedded in. It further examined the representation of the cloud structure and related dynamical processes in a state-of-the-art climate model.

The recently available CloudSat/CALIPSO data provides an opportunity to add a third dimension to the study of clouds in extratropical cyclones (Posselt et al., 2008; Naud et al., 2010). These modern satellite data were used to construct a picture of the three dimensional structure of clouds around Southern Hemisphere extratropical cyclones. Related dynamical fields from reanalyses were composited to identify key links of the cyclone dynamical structure with the cloud fields. The goal of this study was to answer the following questions:

- What is the three-dimensional cloud structure around Southern Hemisphere extratropical cyclones?
- What is the relationship between the cloud structure and the dynamical processes of the cyclone?
- How does the cloud structure change with the intensity and life cycle of the cyclone?
- How well are the cloud structure and related dynamical processes represented in a state-of-the-art climate model?

6.2 Methodology

A cyclone compositing method that combines many individual cyclones into a composite cyclone was used to answer the above questions. This compositing approach provides a useful way to remove cyclone-to-cyclone variability from both observational and model cyclones (Lau and Crane, 1995; Field and Wood, 2007; Naud et al., 2010). The compositing method used in previous studies was modified in this study to composite the relatively sparse CloudSat/CALIPSO data. For each of the cyclones in the composite, the CloudSat/CALIPSO orbits that intersect the 4000 km × 4000 km cyclone area box was found. The cyclone area box was subdivided into 100 km × 100 km boxes and the 2B-GEOPROF-LIDAR pixels were assigned to the appropriate box for each cyclone. Finally, the cloudy and total pixels falling into each box were counted to obtain the cloud fraction in each 240 m height bin around the composite cyclone. Following this modified compositing method, the relatively sparse sampling of CloudSat was turned into a revealing composite cloud structure around cyclone center. The three-dimensional cloud structure related to many other atmospherical phenomenon such as anticyclones or the Madden-Julian Oscillation (MJO) can potentially be constructed using this method.

In addition to the cloud observations and objectively tracked cyclones, supplementary reanalysis fields, frontal locations and radiation and precipitation data were used to construct, for the first time, a fairly complete three-dimensional picture of a composite Southern Hemisphere extratropical cyclone. This composite information was used to quantify the relationship between dynamical variables and clouds. Trajectory analysis was applied to better define the airflows through the composite cyclone more precisely. The compositing method developed in this study provides a more comprehensive approach to evaluate a climate model's ability in simulating clouds and dynamical processes in extratropical cyclones. It was applied to assess a state-of-the-art climate model. The model's cloud and dynamical fields along with precipitation and radiation fields related to modeled cyclones were assessed.

6.3 Conclusions

The application of the compositing technique to both observations and the model allows for answering the key science questions posed at the beginning of this study.

What is the three-dimensional cloud structure around Southern Hemisphere extratropical cyclones?

A cyclone compositing techniques were used to composite Southern Hemisphere extratropical cyclones. The cloud structure associated with them was constructed using CloudSat/CALIPSO measurements. The velocity and thermodynamic fields were derived from reanalyses and composited to better understand the relationship between the clouds and dynamical properties of extratropical cyclones. The constructed three dimensional structure of clouds closely resembles the classical conceptual pictures of clouds (Bjerknes and Solberg, 1922; Posselt et al., 2008; Naud et al., 2010) related to extratropical cyclones. The main characteristics of the constructed three dimensional picture of a composite Southern Hemisphere extratropical cyclone are as follows.

- Thicker high top clouds are found in the warm frontal region. This region is also characterized by a maximum rainfall, maximum mid - and upper level ascent and high relative humidity.
- Thin cirrus clouds are located at the leading edge of the warm frontal region.
- A smaller but still significant region of thick clouds and precipitation is located along the cold frontal regions to the north of the cyclone.
- Mid-level clouds extend to the south-east side of the cyclone centre ahead of the cyclone.
- Low level clouds of various depth can be found all around the system and form the dominant cloud type in the north-west sector of the composite cyclone. Thick and high clouds are essentially absent in that region owing to strong subsidence behind the frontal systems. The strongest net radiative effects are also found in this region, which is dominated by a net cooling of 90-130 W/m^2.

Forty - eight hour back trajectories constructed from the composite cyclone motion field clearly show the three main airstreams found in extratropical cyclones, the warm conveyor belt, the cold conveyor belt and the dry intrusion. Consistent with conceptual cyclone models, it was found that trajectories in the region of ascent show higher values of cloud fraction and relative humidity while trajectories in the region of descent show smaller values of cloud fraction and relative humidity. The cyclone composite constructed here provides an innovative way to evaluate the ability of climate models to capture the cyclone structure (see below).

This study, for the first time, constructs a comprehensive qualitative picture of an archetypal extratropical cyclone in the Southern Hemisphere entirely from observations. It thereby significantly enhances previous studies that proposed conceptual models for these systems. By drawing a quantitative rather than just qualitative picture of the cyclone structure it leads to deeper insights into the working of cyclones as well as providing a more useful tool for model evaluation.

What is the relationship between the cloud structure and the dynamical processes of the cyclone?

In extratropical cyclones, cloud structures are invariably linked to the internal circulations in it. This study aimed to quantify the relationship between the cloud field and dynamical fields. Two dynamical fields, vertical motion and relative humidity, which are important for the formation and dissipation of clouds, were studied. The relationship between the cloud fraction, vertical motion and relative humidity was then quantified. The main conclusions related to this question are as follows:

- The relationship between cloud fraction, vertical motion and relative humidity changes considerably with height.
- The range of all variables is larger at lower levels than that at higher levels.
- Ascent is confined to a smaller area and stronger than descent in the composite cyclone. The higher values of cloud fractions are evident in the region of ascent and the region of descent shows low values of cloud fraction.
- There is a strong quasi-linear relationship evident between the three variables at lower levels. This relationship becomes weak at higher levels.
- Particular regions in the composite cyclone have special characteristics depending on their position relative to the cyclone center. The region at the center and eastern side of the cyclone is characterized by strong ascent, high

relative humidity and high values of cloud fraction. Medium ascent values and relative dryness are the main characteristics of the immediate surrounding region. Related to the dry slot, the western side of the cyclone center is very dry and has very low values of cloud fraction, except at very low levels.

How does the cloud structure change with the intensity and life cycle of the cyclone?

This question has been addressed in Chapter 4 by defining a simple cyclone classification method. The change in relationship between clouds and dynamical fields with cyclone strength and life cycle were investigated. First, cyclones were classified into four classes considering their deepening or filling stage and their central pressure. Those four classes are the High Pressure Deepening (HPD) class, the Low Pressure Deepening (LPD) class, the Low Pressure Filling (HPF) class and the High Pressure Filling (HPF) class.

- The precipitation in the filling classes is 50% less than in the deepening classes.
- The vertical motion field follows the comma shaped structure for all four classes. The maxima of ascent and maxima of cloud fraction are matched well in all four classes.
- The ascent is strong in the deepening classes while the descent becomes strong in the filling classes.
- The LPD class is characterized by the strongest ascent, highest relative humidity and highest values of cloud fraction, compared to the other cyclone classes.
- An eastward shift in the maxima of cloud fraction, relative humidity and ascent is evident as the cyclone progresses through its life cycle.
- The relationship between vertical motion, relative humidity and cloud fraction changes with the class of cyclone. These relationships are stronger in the deepening classes and are weaker in the filling classes. When compared in terms of height, these relationships are strong at the lower levels and weak at the higher levels, for all classes.

The structure of extratropical cyclones at different stages of their life cycle is investigated by defining a simple classification method here. This provided some insights into the processes that relate clouds and precipitation to the state of dynamical development of the cyclone. Due to the nature of the CloudSat/CALIPSO data and the small number of cyclones (from only two JJA seasons) this analysis resulted in a sparsely populated cloud structure around composite cyclone for all classes. To investigate systematic structural changes in the cloud field related to all classes, the analysis of cyclones over many years would be required.

How well are the cloud structure and related dynamical processes represented in a state-of-the-art climate model?

The strong relationships between the clouds and dynamical variables suggests that the representation of the dynamical processes and airflows of extratropical cyclones is of great importance in models to correctly predict the cloud fields. If the dynamical processes of cyclones are poorly represented in the model, then there is no reason to believe that it can produce the clouds with the right properties in the correct locations. The Australian Community Climate and Earth System Simulator (ACCESS) model was evaluated for its ability, to simulate the observed cloud and dynamical features identified previously. Using the MSLP field of the model, the cyclones were tracked using the method of Bauer and DelGenio (2006). As in the observational analysis, the main characteristics of cyclones were examined by compositing model data in a cyclone-relative reference framework. First, the ISCCP simulator was used to analyze the model clouds. It was shown that there is a lack of clouds below 500 hPa in the model which is consistent with earlier studies (e.g. Field et al. (2011)). Similar to the observations, the maximum of the shortwave cloud radiative effect in the model is found near the cyclone center. However, compared to the observations, the model failed to produce a strong enough shortwave CRE. Consistent with conclusions of earlier studies, a particularly large shortwave CRE bias is found in the cold air region (Bodas-Salcedo et al., 2012; Field et al., 2011).

The three-dimensional model cloud structure was assessed against CloudSat / CALIPSO observations. The model is able to qualitatively reproduce the overall cloud structure around the cyclone center. However, it showed several shortcomings:

- High level cloud occurrence is somewhat overestimated and low level cloud occurrence is severely underestimated.

- The circulation around the cyclone center is too weak in the model, compared to the observations.

- The representation of airflows in the cyclone is poor in the model.

- The relationship between cloud fraction and larger scale dynamical variables in the model is not well reproduced. The model fails to show the observed quasi-linear relationship between cloud fraction and relative humidity which is evident in the observations.

- The range of the dynamical variables in the composite model cyclone is smaller than observed, indicating that the dynamical properties of the model cyclones are not well simulated. This must be influencing cloud field in the model.

- Overall, the model reproduces the observed cyclone evolution. The dynamical and cloud fields in the model are stronger in the deepening classes and are weaker in the filling classes. However, in the filling classes, the dynamical and cloud fields are less well defined in the model.

The lack of clouds particularly at low levels in the model could explain Trenberth and Fasullo's (2010) finding that the absorbed shortwave radiation in the Southern Ocean is higher in the climate models than observed. The Southern Hemisphere is ocean dominated and a lack of clouds in the model will cause an excess solar radiation at the ocean surface. To produce clouds with the right properties in their appropriate locations, climate models must first address their weak circulation in extratropical cyclones. Southern Hemisphere cyclone cloud occurence has greater sensitivity to changes in humidity and hence may be more sensitive to changes in water vapor content and, consequently, to changes in surface temperature (Naud et al., 2012). Therefore, for future developments, GCMs must address the low relative humidity and the poorly simulated relationship between clouds and relative humidity.

6.4 Future work

This study has shown that compositing is a potent tool for investigating the structure of extratropical cyclones and to assess the simulation of extratropical cyclones in climate models. CloudSat data were used to extend the two-dimensional view of extratropical cyclones in previous studies to a truly three-dimensional perspective. The combination of these modern satellite cloud observations, objectively tracked cyclones and fronts and supplementary reanalysis fields provides a consistent three dimensional picture of a composite Southern Hemisphere extratropical cyclone. It would be a great addition to this if microphysical properties of clouds could be composited around the cyclone center and added to this analysis. Furthermore, this study focussed on only the Southern Hemisphere extratropical cyclones. It would be of great interest to compare them to their Northern Hemisphere counterparts.

Perhaps the most valuable aspect of our analysis is its use for the evaluation of climate models. Given the large biases in the radiation budget in the models at the top of atmosphere, it is necessary to test the climate model's ability not only to accurately represent the cloud field in the right amount and at the correct location but also to represent the relationships between clouds and dynamical fields evident in the observations. The methodology developed in this study provides a comprehensive alternative to evaluate a model's ability to simulate the concurrent cloud, dynamical, radiative and precipitation structures related to cyclones. By quantifying the relationships between clouds and dynamical fields, the possibility of a more thorough evaluation of climate models was possible.

This study showed that the ACCESS model has several shortcomings in the simulation of clouds around composite cyclone center. The model clearly underestimates the variability of the dynamical fields across the cyclone, indicating that the dynamical properties of the model cyclones are not well simulated. It would be interesting to see if any of these model outputs alter with use of the COSP simulator for model simulation. Using the methodology developed here, comparison between different models or comparison between many versions of any model is easily possible. Furthermore, it would be interesting to perform model sensitivity studies, such as changes to the model resolution or model parameter settings to identify possible ares of model improvement.

In the extratropical regions, cloud processes are mainly governed by atmospheric dynamics. The methodology developed here links dynamics with cloud field in the cyclone. Clearly there remain large errors related to clouds in climate models which must be addressed in order to have confidence in future projection of the Earth's climate. A natural extension of the work presented here is the application of the methodologies to the large climate model ensemble collected by the CMIP5 project, to gain a comprehensive understanding of modern climate models ability to simulate Southern Ocean cyclones.

References

Adler, R. F., G. J. Huffman, A. Chang, R. Ferraro, P. Xie, J. Janowiak, B. Rudolf, U. Schneider, S. Curtis, D. Bolvin, A. Gruber, J. Susskind, P. Arkin, and E. Nelkin, 2003: The version 2 Global Precipitation Climatology Project (GPCP) monthly precipitation analysis (1979 present). *J. Hydrometeor.*, **4**, 1147–1167.

Bates, T. S., V. N. Kapustin, P. K. . Quinn, D. S. Covert, D. J. Coffman, C. Mari, P. A. Durkee, W. J. DeBruyn, and E. S. Saltzman, 1998: Processes controlling the distribution of aerosol particles in the lower marine boundary layer during the First Aerosol Characterization Experiment (ACE 1). *J. Geophy. Res.*, **103**, 16369–16383.

Bauer, M. and A. D. DelGenio, 2006: Composite analysis of winter cyclones in a GCM: influence on climatological humidity. *J. Clim.*, **19**, 1652–1672.

Bengtsson, L., K. I. Hodges, M. Esch, N. Keenlyside, L. Kornblueh, J. J. Luo, and T. Yamagata, 2007: How many tropical cyclones change in a warmer climate? *Tellus*, **59A**, 539–561.

Bengtsson, L., K. I. Hodges, and N. Keenlyside, 2009: Will extratropical storms intensify in a warmer climate? *J. Clim.*, **22**, 2276–2301.

Berry, G., M. J. Reeder, and C. Jakob, 2011: A global climatology of atmospheric fronts. *Geophys. Res. Lett.*, **38**, L04809, doi:10.1029/2010GL046451.

Bjerknes, J. and H. Solberg, 1922: Life cycle of cyclones and the polar front theory of atmospheric circulation. *Geoph. Publ.*, **3**, 3–18.

Blender, R., K. Fraedrich, and F. Lunkeit, 1997: Identification of cyclone track regimes in the North Atlantic. *Quart. J. Roy. Meteor. Soc.*, **123**, 727–741.

Blender, R. and M. Schubert, 2000: Cyclone tracking in different spatial and temporal resolutions. *Mon. Wea. Rev.*, **128**, 377–384.

Bodas-Salcedo, A., M. J. Webb, S. Bony, H. Chepfer, J. L. Dufresne, S. Klein, Y. Zhang, R. Marchand, J. M. Haynes, R. Pincus, and V. O. John, 2011: COSP: satellite simlatin software for model assessment. *Bull. Am. Meteorol. Soc.*, **92(8)**, 1023–1043.

Bodas-Salcedo, A., K. Williams, P. Field, and A. Lock, 2012: The surface downwelling solar radiation surplus over the Southern Ocean in the Met Office model: the role of midlatitude cyclone clouds. *J. Clim.*, **25**, 7467–7486.

Boers, R., J. B. Jensen, P. B. Krummel, and H. Gerber, 1996: Microphysical and short-wave radiative structure of wintertime stratocumulus clouds over the Southern Ocean. *Q. J. R. Meteorol. Soc.*, **122**, 1307–1339.

Boers, R. and P. B. Krummel, 1998: Microphysical properties of boundary layer clouds over the Southern Ocean during ACE 1. *J. Geophy. Res.*, **103,D13**, 16651–16663.

Bony, S., R. Colman, V. M. Kattsov, R. P. Allan, C. S. Bretherton, J. Dufresne, and A. Hall, 2006: How well do we understand and evaluate climate change feedback processes of Climate. *J. Clim.*, **19**, 3445–3482.

Browning, K. A., 1997: The dry intrusion perspective of extra-tropical cyclone development. volume 4, 317–324.

Browning, K. A. and N. M. Roberts, 1994: Structure of a frontal cyclone. *Quart. J. Ray. Meteor. Soc.*, **120**, 1535–1557.

Carleton, A. M., 1979: A synoptic climatology of satellite-observed extratropical cyclone activity for the Southern Hemisphere winter. *Arch Meteorol. Geophys. Bioklimatol, Ser B*, **27**, 265–279.

— 1981: Monthly variability of satellite-derived cyclonic activity for the Southern hemisphere winter. *J. Clim.*, **1**, 21–38.

Carlson, T. N., 1980: Airflow through midlatitude cyclones and the comma cloud pattern. *Mon. Wea. Rev.*, **108**, 1498–1509.

— 1994: Mid-latitude weather systems. *Harper Collins Academic*.

Catto, J. L., L. C. Shaffery, and K. I. Hodges, 2010: Can climate models capture the structure of extratropical cyclones? *J. Clim.*, **23**, 1621–1635.

Cess, R. D., G. L. Potter, J. Blanchet, G. J. Boer, A. D. Genio, M. Deque, V. Dymnikov, V. Galin, W. L. Gates, S. J. Ghan, J. T. Kiehl, A. A. Lacis, H. L. Treut, Z.-X. Li, X.-Z. Liang, J. Mcaveny, V. P. Melesko, J. F. B. Mitchell, J. Morcrette, D. A. Randall, L. Rikus, E. Roeckner, J. F. Royer, U. Schlese, D. A. Sheinin, A. Slingo, A. P. Sokolov, K. E. Taylor, W. M. Washington, R. T. Wetherald, I. Yagai, and M. Zhang, 1990: Intercomparison and Interpretation of Climate Feedback Processes in 19 Atmospheric General Circulation Models. *J. Geophy. Res.*, **95**, 16601–16615.

Champion, A. J., K. i. hodges, L. O. Bengtsson, N. S. Keenlyside, and M. Esch, 2011: Impact of increasing resolution and a warmer climate on extreme weather from Northern Hemisphere extratropical cyclones. *Tellus*, **63A**, 893–906.

Collins, W., N. Bellouin, M. Doutriaux-Boucher, N. Gedney, T. Hinton, C. Jones, S. Liddicoat, G. Martin, F. OConnor, J. Rae, C. Senior, I. Totterdell, S. Woodward, T. Reichler, and J. Kim, 2008: Evaluation of the HadGEM2-ES model. Hadley Centre Technical Note. *http://www.metoffice.gov.uk/research/hadleycentre/pubs/HCTN/index.html*, **74**, 48pp.

Eckhardt, S., A. Stohl, H. Wernli, P. James, C. Forster, and N. Spichtinger, 2004: A 15-year climatology of warm conveyor belts. *J. Climate*, **17**, 218–237.

Eliassen, A. and E. Kleinschmidt, 1957: Dynamic meteorology. *Handbunch der Physik ,S. Flugge, Ed. Springer-Verlag, Berlin*, **48**, 1–154.

Evans, M. S., D. Keyser, L. F. Bosart, and G. M. Lackmann, 1994: A satellite derived classification scheme for rapid maritime cyclogenesis. *Mon. Wea. Rev.*, **122**, 1381—1416.

Field, P., A. Gettelman, R. Neale, R. Wood, P. Rasch, and H. Morrison, 2008: Midlatitude cyclone compositing to constrain climate model behaviour using satellite observations. *J. Clim.*, **21**, 5887–5903.

Field, P. and R. Wood, 2007: Precipitation and cloud structure in midlatitude cyclones. *J. Clim.*, **20**, 233–254.

Field, P. R., A. Bodas-Salcedo, and M. E. Brooks, 2011: Using model analysis and satellite data to assess cloud and precipitation in midlatitude cyclones. *Q. J. R. Meteorol. Soc.*, **137**, 1501–1515.

Fitzpatrick, M. F. and S. G. Warren, 2007: The relative importance of clouds and sea ice for the solar energy budget of the Southern Ocean. *J. Clim.*, **20**, 941–954.

Franklin, C. N., C. Jakob, M. Dix, A. Protat, and G. Roff, 2012: Assessing the performance of a prognostic and a diagnostic cloud scheme using single column model simulations of TWPICE. *Q. J. R. Meteorol. Soc.*, **138**, 734–754.

Gordon, N. D. and J. R. Norris, 2010: Cluster analysis of midlatitude oceanic cloud regimes: mean properties and temperature sensitivity. *Atmos. Chem. Phys.*, **10**, 6435–6459.

Govekar, P. D., C. Jakob, M. J. Reeder, and J. Haynes, 2011: The three-dimensional distribution of clouds around Southern hemisphere extratropical cyclones. *Geophy. Res. Lett.*, **38**, L21805, doi:10.1029/2011GL049091.

Gregory, D. and D. Morris, 1996: The sensitivity of climate simulations to the specification of mixed phase clouds. *Clim. Dyn.*, **12**, 641–651.

Hahn, C. J. and S. G. Warren, 1995: The effect of moonlight on observation of cloud cover at night, and application to cloud climatology. *J. Clim.*, **8**, 1429–1446.

Harrold, T. W., 1973: Mechanisms influencing the distribution of precipitation within baroclinic disturbances. *Quart. J. roy. Meteorol. Soc.*, **99**, 232–251.

Haynes, J. M., C. Jakob, W. B. Rossow, G. Tselioudis, and J. Brown, 2011: Major characteristics of Southern Ocean cloud regimes and their effects on the energy budget. *J. Clim*, **24**, 5061–5080.

Haynes, J. M., T. S. L'Ecuyer, G. L. Stephens, S. D. Miller, C. Mitrescu, N. B. Wood, and S. Tanelli, 2009: Rainfall retrieval over the ocean with spaceborne W-band radar. *J. Geophys. Res.*, **114**, doi:10.1029/2008JD009973.

Haynes, J. M., R. T. Marchand, Z. Luo, A. Bodas-Salcedo, and G. Stephens, 2007: A multipurpose radar simulation package: Quickbeam. *Bull. Amer. Meteor. Soc.*, **78**, 1917–1940.

Henderson-Sellers, A., 1986: Cloud changes in a warmer Europe. *Climatic Change*, **8**, 25–52.

— 1992: Continental cloudiness changes this century. *GeoJournal*, **27.3**, 255–262.

Hoskins, B. J. and K. I. Hodges, 2002: New Perspectives on the Northern Hemisphere Winter Storm Tracks. *J. Atmos. Sci.*, **59**, 1041–1061.

Huffman, G. J., R. Adler, M. Morrissey, D. Bolvin, S. Curtis, R. Joyce, B. McGavock, and J. Susskind, 2001: Global precipitation at one-degree daily resolution from multi-satellite observations. *J. Hydrometeor.*, **2**, 36–50.

Jakob, C. and G. Tselioudis, 2003: Objective identification of cloud regimes in the tropical western Pacific. *Geophys. Res. Lett.*, **30(21),2082**, doi: 10.1029/2003GL018367.

Jiang, J. H., H. Su, C. Zhai, V. Perun, A. D. Genio, L. Nazarenko, L. Donner, L. Horowitz, C.Seman, J. Cole, A. Gettleman, M. A. Ringer, L. Rotstayn, S. Jeffrey, T. Wu, F. Brient, J. Dufresne, H.Kawai, T. Koshiro, M. Watanabe, T. Lecuyer, E. Volodin, T. Iversen, H. Drange, M. Mesquita, W. G. Read, J. W. Waters, B. Tian, J. Trixeira, and G. Stephens, 2012: Evaluation of cloud and water vapor simulations in CMIP5 climate models using NASA "A-Train" satellite observations. *J. Geophys. Res.*, **117**, D14105, doi:10.1029/2011JD017237.

Jones, D. A. and I. Simmonds, 1993: A climatology of southern Hemisphere extratropical cyclones. *Clim. Dyn.*, **9**, 131–145.

Jones, J. M. and M. Widmann, 2004: Atmospheric science: Early peak in Antarctic oscillation index. *Nature*, **432(7015)**, 290–291.

Jones, P. A. and A. Henderson-Sellers, 1992: Historical records of cloudiness and sunshine in Australia. *J. Clim.*, **5**, 260–267.

Justice, C. O., E. Vermote, J. R. G. Townshend, R. Defries, D. P. Roy, D. K. Hall, V. V. Salomonson, J. L. Privette, G. Riggs, A. Strahler, W. Lucht, R. B. Myneni, Y. Knyazikhin, S. W. Running, R. R. Nemani, Z. Wan, A. R. Huete, W. Leeuwen, R. E. Wolfe, L. Giglio, J. Muller, P. Lewis, and M. J. Barnsley, 1998: The Moderate Resolution Imaging Spectroradiometer (MODIS) land remote sensing for global change research. *IEEE Trans. Geosci. Remote Sens.*, **36**, 1228–1249.

Kanamitsu, M., W. Ebisuzaki, J. Woollen, S. Yang, J. J. Hnilo, M. Fiorino, and G. L. Potter, 2002: NCEP-DOE AMIP-II reanalysis (R-2). *Bull. Amer. Meteor. Soc.*, **83**, 1631–1643.

Kep, S. L., 1984: A climatology of cyclogenesis, cyclone tracks and cyclolysis in the Southern Hemisphere for the period 1972-81.. *University of Melbourne, Department of Meteorology,Pub. No.*, **25**.

Klein, S. and C. Jakob, 1999: Validation and sensitivities of frontal clouds simulated by the ECMWF model. *Mon. Weath. Rev*, **127**, 2514–2531.

Lambert, S. J. and J. C. Fyfe, 2006: Changes in winter cyclone frequencies and strengths simulated in enhanced greenhouse warming experiments: Results from the model participating in the IPCC diagnostic exercise. *Clim. Dyn.*, **26**, 713–728.

Lau, N. C. and M. W. Crane, 1995: A Satellite view of the synoptic-scale organization of cloud properties in midlatitude and tropical circulation systems. *Mon. Weath. Rev*, **123**, 1984–2006.

— 1997: Comparing satellite and surface observations of cloud patterns in synoptic-scale circulation systems. *Mon. Weath. Rev*, **125**, 3172–3189.

Lauer, A., K. Hamilton, Y. Wang, V. Phillips, and R. Bennartz, 2010: The impact of global warming on marine boundary layer clouds over the Eastern Pacific - a regional model study. *J. Clim.*, **23**, 5844–5863.

Lim, E. P. and I. Simmonds, 2002: Explosive cyclone development in the Southern Hemisphere and a comparison with Northern hemisphere events. *Mon. Wea. Rev..*, **130**, 2188–2209.

— 2007: Southern Hemisphere winter extratropical cyclone characteristics and vertical organisation observed with the ERA-40 reanalysis data in 1979-2001. *J. Clim.*, **20**, 2675–2690.

Mace, G. G., 2010: Cloud properties and radiative forcing over the maritime storm tracks of the Southern Ocean and North Atlantic derived from A Train. *J.Geoph. Res.*, **115**, D00A26, doi:10.1029/2009JD012517.

Mace, G. G., Q. Z. R. Marchand, and G. Stephens, 2007: Global hydrometeor occurance as observed by Cloudsat: Initial obsertvations from summer 2006. *Geoph. Res. Lett.*, **34**, L09808, doi:10.1029/2006GL029017.

Mace, G. G., Q. Zhang, M. Vaughan, R. Marchand, G. Stephens, C. Trepte, and D. Winker, 2009: A desription of hydrometeor layer occurrence statistics derived from the first year of merged Cloudsat and CALIPSO data. *J.Geoph. Res.*, **114**, D00A26, doi:10.1029/2007JD009755.

Marchand, R., G. G. Mace, T. Ackerman, and G. Stephens, 2008: Hydrometeor detection using CloudSat - an Earth-orbiting 94-GHz cloud radar. *J. Atmos. Oceanic Technol.*, **25**, 519–533.

Martin, G. M., N. Bellouin, W. J. Collins, I. D. Culverwell, P. R. Halloran, S. C. Hardiman, T. J. Hinton, C. D. Jones, R. E. McDonald, A. J. McLaren, F. M. OConnor, M. J. Roberts, J. M. Rodriguez, S. Woodward, M. J. Best, M. E. Brooks, A. R. Brown, N. Butchart, C. Dearden, M. D.-B. J. M. E. P. D. F. N. G. L. J. G. S. H. Derbyshire1, I. Dharssi3, H. T. Hewitt, M. Hobson, M. R. Huddleston, J. Hughes, S. Ineson, W. J. Ingram, P. M. James, T. C. Johns, C. E.

Johnson, A. Jones, C. P. Jones, M. M. Joshi, A. B. Keen, S. Liddicoat, A. P. Lock, A. V. Maidens, J. C. Manners, S. F. Milton, J. G. L. Rae, J. K. Ridley, A. Sellar, C. A. Senior, I. J. Totterdell, A. Verhoef, P. L. Vidale, and A. Wiltshire, 2011: The HadGEM2 family of Met Office United Model climate configurations. *Geosci. Model Dev.*, **4**, 723–757.

McAvaney, B. G. and H. LeTreut, 2003: The cloud feedback intercomparison project:CFMIP. *CLIVAR Exchanges-supplementary contributions*.

Meehl, G. A., C. Covey, T. Delworth, M. Latif, B. McAvney, J. Mitchell, R. Stouffer, and K. E. Taylor, 2007: The WCRP CMIP3 multimodel dataset - A new era in climate change research. *Bull. Am. Meteorol. Clim.*, **88**, 1383—1394.

Morrison, A. E., S. Siems, and M. Manton, 2011: A three-year climatology of cloud-top phase over the Southern Ocean and north Pacific. *J. Clim.*, **24**, 2405–2418.

Morrison, A. E., S. Siems, M. Manton, and A. Nazarov, 2009: On the analysis of a cloud seeding dataset over Tasmania. *J. Appl. Meteor. and Clim.*, **48**, 1267–1280.

— 2010: A modeling case study of mixed-phase clouds over the Southern Ocean and tasmania. *Mon. weat. rev.*, **138**, 839–862.

Mossop, S. C., 1985: Microphysical properties of supercooled cumulus clouds in which ice particle multiplication processes operate. *Q. J. R. meteorol. Soc.*, **111**, 183–198.

Mossop, S. C., A. Ono, and E. R. Weishart, 1970: Ice particles in maritime clouds near Tasmania. *Q. J. Royal Meteorol. Soc.*, **96**, 487–508.

Mossop, S. C., R. E. Ruskin, and K. J. Heferman, 1968: Glaciation of a cumulus cloud at approximatel -4^{0}C. *J. Atmos. Sci*, **25**, 889–898.

Naud, C. M., A. D. DelGenio, M. Bauer, and W. Kovari, 2010: Cloud vertical distribution across warm and cold fronts in Cloudsat-CALIPSO data and a General circukation model. *J. Clim.*, **23**, 3397–3415.

Naud, C. M., D. Posselt, and S. van den Heever, 2012: Observational analysis of cloud and precipitation in midlatitude cyclones: Northern versus Southern Hemisphere warm fronts. *J. Clim.*, **25**, 5135–5151.

Neiman, P. J., M. A. Shapiro, and L. S. Fedor, 1993: The life cycle of an extratropical marine cyclone, Part II : Mesoscale structure and dignostics. *Mon. Weat. Rev.*, **121**, 2177–2199.

Neu, U., M. Akperov, N. Bellenbaum, R. Benestad, R. Blender, R. Caballero, A. Cocozza, H. Darce, Y. fang, K. Fraedrich, J. Grieger, S. Gulev, J. Hanley, T. Hewson, M. Inatsu, K. Keay, S. F. Kew, I. Kindem, G. C. Leckbusch, M. L. R. Liberato, P. Lionello, I. I. Mokhov, J. G. Pinto, C. C. Raible, M. Reale, I. Rudeva, M. Schuster, I. Simmonds, M. Sinclair, M. Sprenger, N. D. Tilinina, I. F. Trigo, S. Ulbrich, U. Ulbrich, X. L. Wang, and H. Wernli, 2013: IMILAST: A community effort to intercompare extratropical cyclone detection and tracking algorithms. **94**, 529–547.

Norris, J. R. and S. F. Iacobellis, 2005: North Pacific cloud feedbacks inferred from synoptic-scale dynamic and thermodynamic relationship. *J. Clim.*, **18**, 4862–4878.

Norris, J. R. and C. P. Weaver, 2001: Improved techniques for evaluating GCM cloudiness applied to the NCAR CCM3. *J. Clim.*, **14**, 2540–2550.

Palmer, C. W., 1942: Synoptic analysis over the Southern Hemisphere. *Prof. Note, New Zealand, Meteorol. Office, Wellington*, **1**.

Petterssen, S., D. Bradbury, and K. Pedersen, 1962: The Norwegian cyclone models in relation to heat and old sources. *Geophys. Publ.*, **24**, 243–280.

Posselt, D., G. Stephens, and M. Miller, 2008: Cloudsat-Adding a new dimension to a classical view of extratropical cyclones. *Bull. Amer. Meteor. Soc.*, **89**, 599–609.

Ramanathan, V., B. Barkstrom, and E. F. Harrison, 1989: Climate and the earth's radiation budget. *Phy. Today*, **42(5)**, 22–33.

Rossow, W. B., A. P. G. Tselioudis, and C. Jakob, 2005: Tropical climate described as a distribution of weather states indicated by distinct mesoscale cloud property mixtures. *Geophys. Res. Lett.*, **32**, L21812, doi: 10.1029/ 2005GL024584.

Rossow, W. B. and R. A. Schiffer, 1991: ISCCP cloud data products. *Bull. Amer. Meteorol. Soc.*, **72**, 2–20.

— 1999: Advances in understanding clouds from ISCCP. *Bull. Amer. Meteorol. Soc.*, **80**, 2261–2287.

Rudeva, I. and S. K. Gulev, 2011: Composite analysis of north Atlantic extratropical cyclones in the NCEP Reanalysis data. *Mon. Wea. Rev.*, **139**, 1419–1446.

Ryan, B. F. and W. D. King, 1997: A critical review of the Australian experience in cloud seeding. *Bull. Amer. Meteorol. Soc.*, **78**, 239–254.

Sanderson, B. M., C. Piani, W. J. Ingram, D. A. Stone, and M. R. Allen, 2008: Towards constraining climate sensitivity by linear analysis of feedback patterns in thousands of perturbed-physics GCM simulations. *Clim. Dyn.*, **30**, 175–190.

Schiffer, R. A. and W. B. Rossow, 1983: The International Satellite Cloud Climatology Project (ISCCP): The first project of the World Climate Research Program. *Bull. Amer. Meteorol. Soc.*, **64**, 779–784.

Schultz, D. M., 2001: Reexamining the cold conveyor belt. *Mon. Weath. Rev.*, **129**, 2205–2225.

SenGupta, A., A. Santoso, A. Taschetto, C. C. Ummenhofer, J. Trevena, and M. H. England, 2009: Projected Changes to the Southern Hemisphere Ocean and Sea Ice in the IPCC AR4 Climate Models. *J. Clim.*, **22**, 3047–3078.

Shapiro, M. A. and D. Keyser, 1990: Fronts, jet streams, and the tropopause. *Extratropical Cyclones, The Erik Palmen Memorial Volume*, . W. Newton and E. O. Halopainen, eds., Amer. Meteor. Soc.

Simmonds, I. and K. Keay, 2000: Mean Southern hemisphere extratropical cyclone behaviour in the 40-year NCEP-NCAR Reanalysis. *J. Clim.*, **13**, 873–885.

Sinclair, M. R., 1994: An objective cyclone climatology for the Southern Hemisphere. *Mon. Wea. Rev.*, **122**, 2239–2256.

— 1997: Objective identification of cyclones and their circulation, intensity and climatology. *Wea. Forecasting*, **12**, 591–608.

Smith, E. J., L. G. Veitch, D. E. Shaw, and A. J. Miller, 1979: A cloud-seeding experiment in Tasmania. *J. Appl. Meteorol.*, **18**, 804–815.

Solomon, S., D. Qin, M. Manning, R. Alley, T. Berntsen, N. Bindoff, Z. Chen, A. Chidthaisong, J. Gregory, G. Hegerl, M. Heimann, B. Hewitson, B. Hoskins, F. Joos, J. Jouzel, V. Kattsov, U. Lohmann, T. Matsuno, M. Molina, N. Nicholls, J. Overpeck, G. Raga, V. Ramaswamy, J. Ren, M. Rusticucci, R. Somerville, T. Stocker, P. Whetton, R. Wood, and D. Wratt, 2007: The physical Science basis. *Contribution of working group I to the fourth assessment report of the Intergovernmental Panel on Climate Change*, S. Solomon, D. Qin, M. Manning, Z. Chen, M. Marquis, K. B. Avery, M. Tignor, and H. L. Miller, eds., Cambridge University Press, Cambridge.

Squires, P., 1956: The microstructure of cumuli in maritime and continental air. *Tellus*, **8**, 443–444.

Stephens, G. L., G. W. Paltridge, and C. M. R. Plat, 1978: Radiation profiles in extended water clouds. III: Observations. *J. Atmos. Sci.*, **35**, 2133–2141.

Stephens, G. L., D. G. Vane, R. J. Boain, G. G. Mace, K. Sassen, Z. Wang, A. J. Illingworth, E. J. OConnor, W. B. Rossow, S. L. Durden, S. D. Miller, R. T. Austin, A. Benedetti, C. Mitrescu, and the CloudSat Science Team, 2002: The Cloudsat mission and the A-TRAIN: A new dimension to space-based observations of clouds and precipitation. *Bull. Amer. Meteorol. Soc.*, **83**, 1771–1790.

Stephens, G. L., D. G. Vane, S. Tanelli, E. Im, S. Durden, M. Rokey, D. Reinke, P. Partain, G. G. Mace, R. Austin, T. LEcuyer, J. Haynes, M. Lebsock, K. Suzuki, D. Waliser, D. Wu, J. Kay, A. Gettelman, Z. Wang, and R. Marchand, 2008: Cloudsat mission: performance and early science after the first year of operation. *J. Geophys. Res.*, **113**, D00A18, doi:10.1029/2008JD009982.

Streten, N. A. and A. J. Troup, 1973: A synoptic climatology of satellite observed cloud cortices over the Southern Hemisphere. *Q. J. R. Meteorol. Soc.*, **99**, 56–72.

Susskind, J., P. Piraino, L.Rokke, L. Iradell, and A. mehta, 1997: Characteristics of the TOVS Pathfinder Path A dataset. *Bull. Amer. Meteor. Soc.*, **78**, 1449–1472.

Taljaard, J. J., 1967: Development, distribution, and movement of cyclones and anticyclones in the Southern Hemisphere during the IGY. *J. appl. Meteorol.*, **6**, 973–987.

Tanelli, S., S. Durden, E. Im, K. S. Pak, D. G. Reinke, P. Partain, and J. M. H. amd R. T. Marchand, 2008: Cloudsat's cloud profiling radar after two years in orbit: Perfoemance, calibration, and processing. *IEEE Trans. Geosci. Remote Sens.*, **46**, 3560–3573.

Trenberth, K. E., 1991: Storm tracks in the Southern Hemisphere. *J. Atmos. Sci.*, **48**, 2159–2178.

Trenberth, K. E. and J. Fasullo, 2010: Simulation of present day and 21st century energy budgets of the southern oceans. *J. Clim.*, **23**, 440–454.

Troup, A. J. and N. A. Streten, 1972: Satellite-observed Southern Hemisphere cloud vortices in relation to convensional observations. *J. Clim.*, **23**, 440–454.

Tselioudis, G. and C. Jakob, 2002: Evaluation of midlatitude cloud properties in a weather and a climate model: Dependence on dynamic regime and spatial resolution. *J. Geophys. Res.*, **107(D24),4781**, doi: 10.1029/2002JD002259.

Tselioudis, G. and W. B. Rossow, 2006: Climate feedback implied by observed radiation and precipitation changes with midlatitude storm strength and frequency. *J. Geophys. Res.*, **33, L02704**, doi: 10.1029/2005GL024513.

Tsushima, Y., S. Emori, T. Ogura, M. Kimoto, M. J. Webb, K. D. Williams, M. A. Ringer, B. J. Soden, B. Li, and N. Andronova, 2006: Importance of the mixed-phase cloud distribution in the control climate for assessing the response of clouds to carbon dioxide increase: A multi-model study. *Clim. Dyn.*, **27**, 113–126.

Twomey, S., 1959: The nuclie of natural cloud formation II: The supersaturation in natural clouds and the variation of cloud droplet concentration. *Geofis. Pura Appl.*, **43**, 243–249.

Twomey, S. and T. Cocks, 1982: Spectral reflectance of clouds in the near-infrared: Comparison of measurements and calculations. *J. Meteorol. Soc. Jap.*, **60**, 583–592.

Twomey, S. and J. Warner, 1967: Comparison of measurement of cloud droplets and cloud nuclie. *J. Atmos. Sci.*, **24**, 702–703.

Ulbrich, U., G. C. Leckebusch, J. Grieger, M. Schuster, M. Akperov, M. Y. Bardin, Y. Feng, S. Gulev, M. Inatsu, K. Keay, S. Kew, M. L. R. Liberato, P. Lionello, I. I. Mokhov, U. Neu, J. G. Pinto, C. C. Raible, M. reale, I. rudeva, I. Simmonds, N. D. Tilinina, I. F. trigo, S. Ulbrich, X. L. wang, H. Wernli, and the IMILast team, 2013: Are Greenhouse Gas Signals of Northern Hemisphere winter extra-tropical cyclone activity dependent on the identification and tracking algorithm? *Meteorologische Zeitschrift*, **22**, 61–68.

VanLoon, H., 1965: A climatological study of the atmospheric circulation in the Southern Hemisphere during the IGY, Part I: 1 July 1957-31 March 1958. *J. Appl. Meteorol.*, **4**, 479–491.

Verlinden, K. L., D. W. J. Thompson, and G. L. Stephens, 2011: The three-dimensional distribution of clouds over the Southern hemisphere high-latitudes. *J. Clim.*, **24**, 5799–5811.

Wallace, J. and P. Hobbs, 2006: Atmospheric science: an introductory survey. *Academic press*, **92**.

Wang, H. and R. Fu, 2000: Influences of ENSO SST anomalies and winter storm tracks on the interannual variability of upper-troposphere water vapor over the Northern Hemisphere extratropics. *J. Climi.*, **13**, 59–73.

Warner, J., 1970: The microstructure of cumulus clouds. Part III. The nature of the updraft. *J. Atmos. Sci.*, **27**, 682–688.

— 1979: On the spatial variability of droplets in clouds. *J. Atmos. Sci.*, **36**, 541–545.

Warren, S., R. Eastman, and C. Hahn, 2007: A survey of changes in cloud cover and cloud types over land from surface observations. *J. Clim.*, **20**, 717–738.

Webb, M., C. Senior, S. Bony, and J. J. Morcrette, 2001: Combining ERBE and ISCCP data to assess clouds in the Hadley centre, ECMWF and LMD atmospheric climate models. *Clim. Dyn.*, **17**, 905–922.

Wielicki, B. A., B. R. Barkstrom, E. F. Harrison, R. B. Lee, G. L. Smith, and J. E. Cooper, 1996: Clouds and the Earth's Radiant energy System (CERES): an earth observing system experiment. *Bull. Am. Meteorol. Soc.*, **77(5)**, 853–868.

Williams, K. D. and M. J. Webb, 2009: A quantitative performance assessment of cloud regimes in climate models. *Clim. Dyn.*, **33 (1)**, 141–157.

Wilson, D. R., A. C. Bushell, A. M. Kerr-Munslow, D. Price, C. Morcrette, and A. Bodas-Salcedo, 2008: A prognostic cloud fraction and condensation scheme. Part II: Results of climate model simulations. *Q. J. R. Meteorol. Soc.*, **134**, 2109–2125.

Winker, D., W. H. Hunt, and M. J. McGill, 2007: Initial performance assesssment of CALIOP. *Geophys. Res. Lett.*, **34,L19803**, doi:10.1029/2007GL030135.

Zhang, M., W. Lin, S. Klein, J. Bacmeister, S. Bony, R. Cederwall, A. del Genio, J. Hack, N. Loeb, U. Lohmann, P. Minnis, I. Muscat, R. Pincus, P. Stier, M. Suarez, M. Webb, J. Wu, S. Xie, M. Yao, , and J. Zhang, 2005: Comparing clouds and their seasonal variations in 10 atmospheric general circulation models with satellite measurements. *J. Geophys. Res.*, **110**, D15S02, doi: 10.1029/2004JD005021.

Zhang, Y. C., W. B. Rossow, A. Lacis, V. Oinas, and M. I. Mishchenko, 2004: Calculation of radiative fluxes from the surface to top of atmosphere based on ISCCP and other global data sets: Refinements of the radiative transfer model and the input data. *J. Geophys. Res.*, **109**, D19105, doi: 10.1029/2003JD004457.

Zhou, C., M. Zelinka, A. Dessler, and P. Yang, 2013: An analysis of the short-term cloud feedback using MODIS data. *J. Clim.*, **26**, 4803–4815.

Zillman, J. W. and P. G. Price, 1972: On the thermal structure of mature Southern Ocean cyclones. *Aust. Meteor. Mag.*, **20**, 34–48.